# Computational and experimental studies reveal a role for airframe configuration in insect flight control

Jorge Bustamante, Jr.

A dissertation
submitted in partial fulfillment of the
requirements for the degree of

Doctor of Philosophy

University of Washington

2021

Reading Committee:

Thomas L. Daniel, Chair

Jeffrey A. Riffell

Adam P. Summers

Program Authorized to Offer Degree:
Biology

University of Washington

## Abstract

Computational and experimental studies reveal a role for airframe configuration in insect flight control

Jorge Bustamante, Jr.

Chair of the Supervisory Committee:
Professor Thomas L. Daniel
Department of Biology

Research on insect flight control has focused primarily on the role of wings. Yet airframe deformations via abdominal deflections during flight may potentially influence the dynamics of flight and play a significant role in control and management of energy resources. To address these general issues, I use a combination of a Model Predictive Control (MPC)-inspired computational inertial dynamics model, free flight experiments in the hawkmoth, *Manduca sexta*, and–in collaboration with another research group–bio-inspired machine learning methods. The 2D inertial dynamics model simulated underactuated and fully actuated models tracking a vertically oscillating flower. Flight performance was evaluated with two metrics: tracking error and cost of transport. The models suggest that fully actuated simulations minimized the tracking error and cost of transport. Moreover nearly eliminating the role of the abdomen by reducing its mass significantly worsened both flight performance metrics. Additionally, I tested the effect of restricted abdomen movement on free flight in live hawkmoths by fixing a carbon fiber rod over the thoracic-abdomen joint. Hawkmoths with a restricted abdomen flew less frequently compared to the sham treatment moths. Furthermore those moths which flew, performed worse than sham treatment moths in various flight performance metrics. I also explored inertial-elastic, and morphological modifications of the dynamics model to examine the trade-offs between flower tracking accuracy and flight performance for a range of size, shapes, abdominal masses, and thoracic-abdomen stiffness

values. I found that increasing abdominal mass reduced tracking error across size ranges while also increasing the mechanical work and cost of transport. Moreover, increasing petiole length reduced tracking error across size ranges while also increasing the mechanical work and cost of transport. Lastly, in a collaborative study, we used deep neural networks (DNNs) trained by MPC data sets to develop an efficient method for solving inverse flight control problems. Furthermore, these DNNs were pruned to determine how sparse a network can be and still yield successful flight. We find that the network can be pruned to $\sim$7% of the original networks weights and still fly successfully. Motions of non-aerodynamic structures, found in all flying animals, and the use of pruning DNNs can inform the development of multi-actuated micro air vehicles as well as determine the role the abdomen plays in insect flight control and energetics.

## TABLE OF CONTENTS

## LIST OF FIGURES

Figure Number Page

2.2 **Methods for simulating trajectories.** The model has a prescribed set of biomechanical properties: both inertial parameters (masses: $M_1$, $M_2$, moments of inertia: $I_1$, $I_2$, vector lengths: $L_1$, $L_2$, $L_3$, torsional spring constant: $\kappa$, and torsional damping coefficient: $\eta$) and aerodynamic parameters (coefficient of drag: $C_d$, dynamic viscosity of air: $\mu_a$, and density of air: $\rho_a$). Each simulation begins with a prescribed set of initial conditions (the set of positions: $q$ and their respective velocities: $\dot{q}$). Monte-Carlo methods randomized the applied forces (magnitude of force: $F$, direction of force: $\alpha$) and torques (abdominal torque: $\tau_{abdo}$, and wing torque: $\tau_{wing}$). There are a set of 2500 randomized forces and torques for each time 20 ms time period, yielding the final conditions. The initial conditions, randomized torques and forces, and biomechanical parameters are all passed into the ordinary differential equations (ODEs) of the system (to see the ODEs and their full derivations, see Appendix Equations 2.30 - 2.33). A loss function ($\lambda$) selects the trajectory with the lowest loss function value. The loss function contains various weights ($w_{1-6}$, see Appendix Table 2.3) which penalize deviations from $y$ and $x$ more than $\theta$. The composition of the vertically oscillating signal $y_{goal}$ is noted in the grey dashed box on the upper right. The time series of the $y_{goal}$ is displayed for a 10 second time period, the frequency components of this signal are noted in the figure below. The values of amplitude and frequency are noted in Appendix Table 2.1. The trajectory selected by the loss function uses the values 25% through the trajectory as the new initial conditions for the next 20 ms time period. A visualization of the trajectories and the selection of one trajectory through time is included in the light blue dashed box on the lower right. . . . . 30

# LIST OF TABLES

## ACKNOWLEDGMENTS

I would like to express my deepest appreciation to my committee chair, and advisor, Dr. Tom Daniel. Without his guidance, constant reassurance, and commitment to my personal development, completion of this dissertation would not be possible. Graduate school has many invisible milestones that most graduate students are unaware of, and Tom is keen to point out when a student crosses such milestones.

What drew me to his lab was the work that his current and former students completed– a unique mix of biology and engineering known as biomechanics. During one of the first conversations we had, I said, "I'm a fan of Andrew Mountcastle's work." Mountcastle was a former graduate student in his lab. To which Tom responded, "I am too." It is fair to say that Tom sees all of his lab members as equals immediately, and treats everyone with the utmost respect. It is an honor to be his last biology graduate student.

I would also like to thank my committee members: Dr. Jeff Riffell, and Dr. Adam Summers. Their continued guidance and feedback aided in elevating the overall quality, clarity, and structure of the thesis. Both their familiarity with, and their contributions to the quality of work presented annually at the Society for Integrative and Comparative Biology have aided in framing this work to a broader audience which would appreciate the work.

In addition, I would like to thank all collaborators on all chapters of the thesis: Mahad Ahmed (former Daniel lab post-bac, and current M.D. student), Dr. Tanvi Deora, Dr. Brian Fabien, Olivia Zahn (Ph.D. student), Dr. Callin Switzer, and Dr. J. Nathan Kutz. Their essential collaboration made this thesis possible.

## DEDICATION

To
my parents, friends, and former students
in recognition of their support, their kinship,
and the joy that they have brought to my life.

*In loving memory of:*
My grandparents Ofilia Bustamante, and Felix Gallardo
who brought so much laughter and life to many loved ones.

Michael J. Brooks
a humanistic mentor to countless people–
–myself included.

And to my friend Jin-Ah Kim
who sparked endless joy while fighting tirelessly
for those she did not even know.

# Chapter 1

# INTRODUCTION

Animal locomotion relies on managing changes in body configuration to generate appropriate forces. Complex negotiations of changes in body configuration are required in terrestrial, aquatic, and aerial locomotion. An example of changes in body configuration during terrestrial locomotion is the upward shifting of tail position in lizards assists in pitch control and allows for lizards to jump onto substrates easier [80]. Such aquatic examples include: lift forces produced by tail and pectoral fins in various aquatic vertebrates [4, 44, 49, 57, 67, 76, 77, 106, 134]. And lastly, in animal flight, wings undergo a dramatic change in configuration (*i.e.* flapping, bending, twisting) to generate the necessary forces for lift.

And yet, insect flight is incredibly complex. Flapping flight is different from fixed wing aerodynamics in synthetic systems (*i.e.* airplanes). Flapping flight in particular is subject to non-linear fluid dynamics which lead to many unsteady mechanisms [40]. Such unsteady mechanisms were summarized thoroughly by Sane in 2003 [108]. These unsteady mechanisms in insect flight, reviewed by Sane included but were not limited to: the Wagner effect [130], clap-and-fling [11, 47, 81, 132], delayed stall and the leading-edge vortex [37, 41, 98, 130], the Kramer effect (rotational forces) [10, 37, 110], added mass inertia [109, 128], and wing-wake interactions [39, 41]. Additionally, for insects, the various body parts are multi-articulated for various physiological and morphological functions [25].

As a result of a desire to understand these phenomena, both in synthetic systems and biological systems, biologists and engineers developed a plethora of visualization and measurement techniques within the last 50 years. Methods for modeling and imaging such complex fluid phenomena and how organisms interact with fluids include: high speed videography, computational fluid dynamics (CFD), and particle image velocimetry (PIV). In 2017, Bomphrey et. al masterfully combined these techniques [16]. Using an eight camera setup to

record freely flying mosquitoes, they were able to model a number of metrics such as the CFD of shed vorticies (often associated with lift), and PIV for both the trailing-edge, and leading-edge vortex during flight. All of these techniques have been utilized at different times for various insects [108].

Indeed, the vast majority of insect flight literature has focused on the wings because they generate the lift forces necessary for flight [38, 42]. However, other body segments may contribute to flight control and maneuverability by changing body configuration during flight. Such examples include the tail motions as a mechanism for flight control in birds and bats [53, 122, 126]. Insects do not have tails, but are rather divided into three body segments (head, thorax, and abdomen), with six legs protruding from the thorax. The legs have been observed to contribute to flight control in insect flight [31]. Likewise, flight control by visually driven abdominal extension and flexion has been observed in various insects [23, 45, 140, 139], along with abdominal undulations for monarch butterflies [125]. These changes in body configuration during flight may well contribute to path control.

This thesis set out to explore how flight control may involve reshaping of the airframe itself by changes in its configuration. This relatively understudied aspect of animal flight may apply to wide range of insect taxa as well as a host of vertebrate flyers. To address this general topic, I combine computational approaches (inspired by model predictive control), experimental analyses of flying hawkmoths, biomechanical measurements of the body, and – in collaboration with another research group – bio-inspired machine learning methods. The thesis is structured around three core chapters, each briefly summarized below:

Chapter 2 will explore if the abdomen contributes to flight control for a simulated moth tracking a vertically oscillating flower. The model established in chapter 2 will recur throughout the thesis. The model in chapter 2 will focus on flight performance between underactuated and fully actuated simulations. Lastly, using the results of the model, we abdominally restricted live hawkmoths to observe changes in flight performance. The findings of this chapter are currently *in review* in *Integrative Organismal Biology* [21].

Chapter 3 explores the trade-offs between flower tracking accuracy and flight performance (*i.e.* energetics) for inertial-elastic, and morphological modifications to the model developed in chapter 2. The findings of this chapter are *in prep* for submission to *Integrative*

*Organismal Biology* [22].

Lastly, chapter 4 uses the model developed in chapter 2, and uses a Deep Neural Network (DNN) to solve the inverse problem of flight control. Additionally, the DNN is pruned to identify how sparsely the network can be pruned and still yield successful flight. The findings of this chapter are *in prep* for submission to *PLoS Computational Biology* [138].

Chapter 2

# ABDOMINAL MOVEMENTS IN INSECT FLIGHT RESHAPE THE ROLE OF NON-AERODYNAMIC STRUCTURES FOR FLIGHT MANEUVERABILITY I: MODEL PREDICTIVE CONTROL FOR FLOWER TRACKING

Jorge Bustamante, Jr. [1,∗], Mahad Ahmed [1], Tanvi Deora [1], Brian Fabien [2], and Thomas L. Daniel [1]

**[1]** Department of Biology, University of Washington, Box 351800, 98195, WA, USA

**[2]** Shiley School of Engineering, University of Portland, 5000 N. Willamette Blvd., 97203, OR, USA

**[*]** Primary author

## *2.1 Abstract*

Research on insect flight control has focused primarily on the role of wings. Yet abdominal deflections during flight can potentially influence the dynamics of flight. This paper assesses the role of airframe deformations in flight, and asks to what extent the abdomen contributes to flight maneuverability. To address this, we use a combination of both a Model Predictive Control (MPC)-inspired computational inertial dynamics model, and free flight experiments in the hawkmoth, *Manduca sexta*. We explored both underactuated (i.e. number of outputs are greater than the number of inputs) and fully actuated (equal number of outputs and inputs) systems. Using metrics such as the non-dimensional tracking error and cost of transport to evaluate flight performance of the inertial dynamics model, we show that fully actuated simulations minimized the tracking error and cost of transport. Additionally, we tested the effect of restricted abdomen movement on free flight in live hawkmoths by fixing a carbon fiber rod over the thoracic-abdomen joint. Moths with a restricted abdomen performed worse than sham treatment moths. This study finds that abdominal motions contribute to flight control and maneuverability. Such motions of non-aerodynamic structures,

found in all flying taxa, can inform the development of multi-actuated micro air vehicles.

## *2.2 Introduction*

With the exception of feed-forward control, most animal movements are governed by multiple streams of sensory inputs that are processed centrally to coordinate force and torque generation by multiple actuators. Such multi-input, multi-output (MIMO) systems underlie complex motor tasks such as grasping and manipulation as well as myriad modes of terrestrial, aquatic and aerial locomotion [32]. Animal flight is an especially challenging MIMO system that relies on both visual and mechanosensory information processing to coordinate complex wing dynamics for movements ranging from forward flight, to hovering, to tracking moving targets [32, 107, 124, 131]. The vast majority of literature pertaining to the control and dynamics of animal flight, however, has largely focused on the wing motions for the clear reason that wings generate the lift forces necessary for flight [38, 42]. Yet other body segments may also contribute to movement control and maneuverability by changing the configuration of their position during flight. For example, tail motions are a key component of the flight control system in birds and bats [53, 122, 126]. In insects, rather than a distinct tail, both the abdomen and legs have been implicated in flight control. For example, leg extension in response to wind gusts in various Hymenoptera have been suggested to serve a role in flight stability [31]. Similarly, visually driven abdominal flexion and extension is thought to contribute to flight control in a variety of insects including moths [45], locusts [23], and fruit flies [140, 139]. A previous study has shown that while insect flight is inherently pitch unstable, movement of the abdomen yields short-term control in the thoracic pitch of a 2-D simulated butterfly [66]. Finally, abdominal undulations (*i.e.*, periodic abdominal swings coupled to wing inertia) have been demonstrated both experimentally and theoretically to be a mechanism which reduces the overall mean power and mean energy requirements for hovering and forward climbing flight in monarch butterflies [125]. These changes in body posture during flight (airframe deformations) may arise either actively (*i.e*, movements driven by the insect) or passively (*i.e*, respond to external perturbations) and may well contribute to path control.

Given that the abdomen contributes a large proportion of mass for insects (up to 46-67%

of body mass for hawkmoths, see Appendix 2.7), a deeper examination of its role in flight control is warranted. Additionally, understanding the relative roles of wings and abdominal movements in accomplishing specific flight tasks presents an interesting inverse problem: can one predict abdominal motions that are required to accomplish a specified path? Previous literature has addressed the inverse problem of hovering and level forward flight using a combination of genetic algorithm wedded with a simplex optimizer [59]. Moreover, a study that solved the inverse problem by linearizing the dynamical system associated with flight control [45] found that flapping flight with active abdominal control operates on the edge of stability.

This paper focuses on flight control in the hawkmoth (*Manduca sexta*) by combining both experimental and computational approaches to address the role of airframe deformations in flight. Computationally, we use an inertial dynamics model of an insect tracking a vertically oscillating signal in which abdominal flexion contributes to the control. Experimentally, we explore this airframe control hypothesis through measurements of free flight behaviors for animals whose abdominal motion is restricted.

We develop an inertial dynamics model inspired by Dyhr *et. al*, [45] to examine the extent of abdominal contribution in the movement control of a 2D inertial model (an insect) tracking a vertically moving target (a moving flower). We use an approach inspired by Model Predictive Control (MPC) to solve the inverse problem of determining the wing forces and torques, along with abdominal motions, that achieve a specified path. In doing so, we explore a fully actuated control model (4 controls for 4 degrees of freedom) and an underactuated model (3 controls for 4 degrees of freedom). In all cases we analyze both the tracking error of these control strategies as well as a non-dimensional measure of the energy cost associated with each strategy. Interestingly, all MPC solutions were able to solve the flower tracking. However, there are subtle differences in the errors of each approach and substantial differences in the cost of tracking. Additionally, experimentally suppressing abdominal motions in live hawkmoths greatly inhibits flight performance.

### *2.3 Model formulation and methods*

We developed an inertial dynamics model coupled with Monte Carlo simulations to address the question of abdominal contribution to flight maneuverability and flight control. Our model simulates the dynamics of a flying moth as a reduced-order two-mass rigid body system. We used an Euler-Lagrange formulation to generate a system of ordinary differential equations that relate wing forces and body torques to the position and angles of the body in time. Our model includes aerodynamic drag forces and is in the form of a nonlinear, second order system of ordinary differential equations. As we indicate below, we use a method inspired by Model Predictive Control (MPC).

*Insect Geometric Model*

The hawkmoth was modeled as two mechanically coupled ellipsoid masses: mass ($m_1$ and $m_2$) with associated moments of inertia ($I_1$ and $I_2$) (Figure 2.1b). A pin joint connects the base of the head-thorax mass $m_1$ to the abdomen mass $m_2$. The pin joint connection between the two masses was modeled as a damped torsional spring with a spring constant ($\kappa$) and a torsional damping term ($\eta$) as shown in Beatus and Cohen [7]. The externally applied efforts of the system include the aerodynamic force of magnitude ($F$), with a direction ($\alpha$) with respect to the long axis of $m_1$. Additionally, an abdominal torque at the pin joint ($\tau_{abdo}$), and the wing torque ($\tau_{wing}$) serve as two additional control features.

The model follows the traditional right-hand coordinate system (*i.e.*, $x$ and $y$ are positive going right and upward respectively, Figure 2.1b). The angular motion associated with the head-thorax mass relative to an inertial coordinate frame is $\theta$, while the motion associated with the abdomen mass is $\phi$, which is also relative to an inertial frame (Figure 2.1b). To keep consistency with right-handed coordinates, all counter-clockwise rotations are defined as positive.

The model was modified to examine four cases with the modification shorthand in parentheses next to their respective definitions: (1) fully actuated ("fa", the basic model, Figure 2.1b), (2) fully actuated with the location of the applied force shifted from the center of mass ("fs", Figure 2.1c), (3) underactuated ("ua", Figure 2.1d) where the wings do not

generate torque, (4) underactuated with the location of the applied force shifted from the center of mass ("us", Figure 2.1e). The modifications that include shifting the location of the applied force from the center of the head-thorax mass are included to determine whether the role of implicit torques on the system provide additional stability. Additionally, these four modified cases were also run with a model where the abdomen mass was decreased by 90% to determine the role the applied torques contribute to maneuverability.

All model morphometric values and mechanical properties were measured from hawkmoths ($N = 10$, 5 males & 5 females). These specific morphometric values and mechanical properties can be found in the Appendix (Table 2.2). We used the torsional damping coefficient from Dyhr *et. al* [45], and empirically measured the torsional spring constant in this study (see 2.3 below).

*Dynamical Equations*

The Euler-Lagrange formulation (Equation 2.1) yields the equations of motion (see Appendix equations 2.9-2.33) necessary to simulate the dynamics of the multi-body model (full derivation in Appendix).

$$\frac{\mathrm{d}}{\mathrm{d}t}\frac{\partial T^*}{\partial \dot{q}} - \frac{\partial T^*}{\partial q} + \frac{\partial V}{\partial q} + \frac{\partial D}{\partial \dot{q}} = e_q^s \tag{2.1}$$

where $T^*$ accounts for the kinetic energies of the system, $V$ accounts for the potential energies of the system, $D$ accounts for the dissipative energies of the system, and $e_q^s$ accounts for the work due to external applied efforts. All energies and efforts are with respect to the generalized coordinates. The equations of motion form a coupled system of second-order non-linear ordinary differential equations, which can be separated and solved using an explicit numerical solver we have written in Python (using odeint). All code is available on https://github.com/JorgeBJr/multibodyDynamicsModel.git .

*Specifying motion and loss function value*

We specified a challenging motion for the model to track. We chose prime frequencies as used in Roth *et. al* [107], and Sponberg *et. al* [117] to determine whether the output

response of the model was non-linear. The prescribed goal signal (equation 2.2) includes eleven prime number frequencies (see Appendix 2.7, Table 2.1), and eleven amplitudes of decreasing magnitude to ensure the velocity of the signal was not increasing as frequency increases.

$$\begin{aligned} y_{goal} =& A_1 sin(2\pi f_1 t) + A_2 sin(2\pi f_2 t) + ... \\ &+ A_{11} sin(2\pi f_{11} t) \end{aligned} \tag{2.2}$$

where the amplitudes $A_i$ and frequencies $f_i$ are specified in the Appendix (Table 2.1) for the $y_{goal}$. The specified goal motion of the $x$-direction ($x_{goal}$) is always set to zero. The specified goal angle of the head-thorax mass ($\theta_{goal}$) is always set to $\pi/2$.

To explore the theoretical control authority, the applied efforts ($F$, $\alpha$, $\tau_{abdo}$, $\tau_{wing}$) were randomized using Monte-Carlo methods. Each individual randomized set of applied efforts yields an individual realization. Each realization was allowed to run for a time period of 20 ms. 2500 realizations were generated from the randomized set of applied efforts for a given 20 ms time period with the same initial conditions for each particular time period. To simulate a closed-loop system, a loss function (Equation 2.3) selects one realization out of the 2500 realizations with the lowest loss function value for the particular time period (Figure 2.2, bottom right).

$$\begin{aligned} \lambda = & w_1(x - x_{goal})^2 + w_2(y - y_{goal})^2 \\ &+ w_3(\theta - \theta_{goal})^2 + w_4(\dot{x} - \dot{x}_{goal})^2 \\ &+ w_5(\dot{y} - \dot{y}_{goal})^2 + w_6(\dot{\theta} - \dot{\theta}_{goal})^2 \end{aligned} \tag{2.3}$$

The loss function takes the difference between the prescribed goal value at the end of the 20 ms simulation, and where the realization actually ended up. This is calculated for the head-thorax motion ($\theta$), rectilinear position ($x$ and $y$), and their respective derivatives($\dot{\theta}$, $\dot{x}$, and $\dot{y}$). Each term has a prescribed weighting coefficient ($w_{1-6}$ see Appendix) intended to minimize deviations of the head-thorax motion and rectilinear motion.

Drawing inspiration from MPC, we incorporated a receding horizon to minimize the time-accumulated error throughout the 20 ms simulation time. After the loss function

selects the realization with the lowest loss function value, the model travels 25% of the selected path. The state variables at this 25% point become the new initial conditions, and we simulate a new batch of 2500 realizations (Figure 2.2). This method is repeated until the simulation time of 10 seconds is completed.

*Evaluating simulated flight performance*

The model simulation flight performance was evaluated using two key metrics: (1) non-dimensional tracking error, (2) cost of transport.

We defined the non-dimensional tracking error (equation 2.4) as the rectilinear distance between the the final location of the 20 ms simulation ($x_{sim}$, and $y_{sim}$) and the goal position. This distance is normalized by dividing the body by length of the organism.

$$\frac{\sqrt{(x_{sim} - x_{goal})^2 + (y_{sim} - y_{goal})^2}}{body\ length} \tag{2.4}$$

The generalized form of mechanical work is defined in equation 2.5 as a summation of rectilinear work (work done by the wing force in translational motions), rotational work (work done by the torque resulting from wing forces), and the work due to applied torques (wing torque and abdominal flexion torque).

$$\begin{aligned} Work = \ & \vec{F} \mid \Delta\vec{r} \mid + \mid (\vec{r} \times \vec{F})\theta \mid \\ & + \mid \tau_{wing}\theta \mid + \mid \tau_{abdo}\beta \mid \end{aligned} \tag{2.5}$$

where $\vec{r}$ is the generalized positional vector (see appendix), $|\Delta\vec{r}|$ is the distance traveled in each time step of the simulation. The absolute value of each term in equation 2.5 represents the energy expenditure of movement in space. Note each model treatment as denoted in Figure 2.1 may not contain every term in equation 2.5 for the instantaneous work.

The cost of transport describes the normalized energy expenditure of movement in space. The cost of transport normalizes the mechanical work, as referred to in equation 2.5, by dividing the product of the weight and distance traveled by the moth at any 20 ms interval as seen in equation 2.6.

$$C = \frac{Work}{mg \mid \Delta \vec{r} \mid} \tag{2.6}$$

where $m$ is the mass of the head-thorax section, and $g$ is the acceleration due to gravity.

*Experimental materials and methods*

*Hawkmoth preparation and abdominal restriction methods*

Tobacco hawkmoths (*Manduca sexta*) were collected from a colony at the University of Washington. The moths were maintained on a 12:12 hour light-dark cycle. For the free flight experiment, we used 2-5 days post-eclosion hawkmoths, and specifically selected adults who showed eagerness to feed (actively flew or hovered in front of a red-light headlamp) ∼2 hours after the beginning of the dark cycle.

For the experimental treatment (3 moths, a total of 12 trials), a single carbon fiber rod (0.048-0.095 g) was glued on the dorsal side across the thorax and abdomen joint using superglue to restrict the motion of this joint. Carbon fiber rods for the experimental treatment composed 0.40% +/- 0.14% (mean +/- standard deviation) of moth body mass.

A sham treatment was also incorporated in a separate set of moths (4 moths, total of 14 trials). These sham treatment moths had two separate carbon fiber rods glued to the thorax and abdomen respectively (total weight range 0.047-0.067 g). Carbon fiber rods for the sham treatment composed 0.24% +/- 0.03% (mean +/- standard deviation) of moth body mass. The purpose of the sham treatment was to account for the weight of the carbon fiber rod. For moths that flew, their last exposure to light was 1.03-4.78 hours (or 62-287 minutes) before flight experiments.

All free flight experiments were performed during the active, night period of hawkmoths including dusk and dawn at 20-25°C. All moths were flower-naïve and had never fed as adults prior to experimentation.

A separate set of 10 hawkmoths (5 males, 5 females) were used to measure the percentage of abdominal mass (as reported in the Introduction). For these measurements, we used 1-3 days post-eclosion hawkmoths. The total mass of the moth was weighed prior to cold

anesthetization. After at least 45 minutes of cold anesthetization, the head, thorax, and abdomen were all excised and weighed separately. The value reported in the introduction is the range of percentages of abdominal mass for each individual moth (See Appendix, Table 2.4).

*Free flight behavioral setup*

To document flight behaviors we used an experimental system established by Deora *et. al* [35]. Moths flew in an artificial arena (36" x 27" x 36"), darkened, and enclosed from all external lighting. We used an overhead video camera (Basler piA640-210gm GigE) recording at 100 frames per second, 200 $\mu$sec exposure under infrared illumination. The enclosure was illuminated with diffuse white light at 0.1 lux with a custom-made LED lightbox (SpyeGrey film, Spyeglass$^{TM}$).

The moths were tasked with feeding from an artificial, 3D printed, funnel shaped, stationary flower [35]. We used a 7-component scent mixture which mimicked the scent of hawk moth-pollinated flowers to motivate flight ([24, 105]: 0.6% benzaldehyde, 17.6% benzyl alcohol, 1.8% linalool, 24% methyl salicylate, 3% nerol, 9% geraniol, 0.6% methyl benzoate in mineral oil). A few drops of this scent was placed on filter paper. The filter paper was placed directly above the artificial flower on the ceiling of the artificial enclosure, and covered with a dark cloth so as not to cause a visual distraction for moths during the experiment.

*Evaluation of moth free flight performance*

We tracked the moth head using DeepLabCut (DLC, [85], see also methods of Deora *et. al* [35]) to capture and analyze flight paths of the abdominally restricted and sham treated moths. The DLC model was trained on a previous training data set in [35] which used similar overhead view of moth feeding from artificial flower. We wrote custom codes (available on https://github.com/itsMahad/MothAbdominalRestriction) to analyze these flight tracks. We used several metrics to capture flight dynamics and flight path characteristics like mean velocity, mean acceleration, flight path tortuosity, box dimension as well as analyzed the spectral characteristics of the path. We used a Wilcoxon rank sum test to analyze the

differences between abdominally restricted and sham moths across all metrics.

We computed the path tortuosity (equation 2.7), a metric of how much a moth deviates from a mean or straight flight path to compare flight paths across our treatments. Because moths flight path often cross themselves in this behavioral paradigm, we analyzed tortuosity along smaller segments of the path, essentially creating a sliding window estimate of tortuosity of 40 frames (100ms, equivalent to 10 wing beats which we felt was an adequate time scale to capture relevant flight trajectory features) for each trajectory and computed the total distance and displacement for each window. We used the following equation to compute tortuosity of each segment (Equation 2.7), and average across these to compute the mean tortuosity for each flight path. Similarly, we also used fast Fourier transform on each trajectory segment to compute the mean power at various temporal frequencies.

$$Tortuosity = \frac{\sum_{k=i}^{i+40} \sqrt{(x_{k+1} - x_k)^2 + (y_{k+1} - y_k)^2}}{\sqrt{(x_c - x_0)^2 + (y_c - y_0)^2}} \tag{2.7}$$

where $i = [i, N - 40]$ and $N$ is the number of frames for any trial. This represents a sliding window of tortuosity estimates.

We also used fractal dimensions (box counting dimension) to quantify the complexity (i.e. jaggedness) of each flight trajectory. Fractal dimensions have been previously used to quantify the geometry of animal paths [9]. They measure how shapes and patterns scale in comparison to the space they occupy. Hence smaller a fractal value ($\sim$1) means a measured dimension is more similar to a line; higher values ($>$1.5) means a measured dimension more similar to that of an area. Prior to analysis, each trajectory was saved as an image, so that the space between discrete centroid positions was linearly interpolated. This allowed us to analyze the entire shape of the trajectory irrespective of the moth's velocity.

*Double-blind scoring of rolling maneuvers*

With a single camera system, body pitch and roll are difficult to quantify, but human observers are able to assess the presence or absence of such motions. To determine whether or not there was an increased incidence of rolling in experimental treatment moths relative to sham moths, we used a double-blind study of the moth video trials. Eight volunteers

were tasked with the simple binary scoring (yes/no) of whether or not they witnessed rolling in the 26 flight bouts (12 videos of experimental treatment flight bouts, and 14 videos of sham treatment flight bouts). The order of the videos was randomized, and the treatment of the moth was hidden to the volunteer. The metric of evaluation for this scoring was if the incidence of rolls in experimental treatment moths were higher than the incidence of rolls in the sham treatment moths.

*Torsional spring constant measurements*

The torsional spring constant was empirically measured for our multibody dynamics model. All torsional spring constant experiments were performed on 1-2 days post-eclosion dead hawkmoths ($N = 20$ moths). There were two groups of dead moths: moths in the freezer (-20°C) for 1 hour before ($N = 10$ moths; 5 male, 5 female) and 10 minutes before ($N = 10$ moths; 5 male, 5 female) the head was excised. At the time of head ablation, the wings and legs were also ablated. The scales were removed from the thorax so as to mount the moth into its measurement rig more easily.

Moths were mounted on a micro manipulator with the thorax firmly pierced by two nails to maintain its position during measurements. The abdomen was aligned with a the true vertical as best as possible, and lassoed to the lever arm of a Dual Mode Muscle Lever System (Aurora Scientific, Model 360) firmly with thread.

The Dual Mode Muscle Lever System had the dual task of applying the sinusoidal oscillations and recording the torque that the abdomen exerted back on the lever arm as a response. Calibration of the Dual Mode Muscle Lever System to the corresponding angles and torques was done by tying a rubberband (Sparco Premium Quality Rubber Bands, 1614LB, Size 16, 2 1/2" x 1/16") to a vertical rod. All data acquisition was performed with a National Instruments DAQ (NI USB-6229) at a sampling frequency of 1000 Hz.

The prescribed sinusoidal signal was 15 seconds long, and composed of one of five driving frequencies (0.2, 1, 5, 10, 20 Hz), with one of three input voltages (2, 5, 9 Volts) which correspond to the different angular excursions of the lever arm. Each of these 15 signals had three replicates. The order of these 45 trials were randomly permuted for each of the

20 moths to ensure there was no statistical bias or unusual response by the moth abdomen to different driving frequencies and amplitudes.

We recorded the time series for both the abdominal angle and applied torque for these 45 trials. Both time series signals were Fourier transformed. These two Fourier transformed signals each have a real component and an imaginary component. The real components of the two Fourier transformed signals is used to calculate the torsional spring constant:

$$\kappa = Real\left(\frac{T}{\Theta}\right) + I\omega^2 \tag{2.8}$$

where $T$ is the Fourier transform of the torque signal, $\Theta$ is the Fourier transform of the angle signal, $I$ is the moment of inertia of the moth abdomen, and $\omega$ is the driving frequency. For the full derivation, see the Appendix.

All instantaneous torsional spring constants (for all trials and moths) were plotted with respect to driving frequency and fit with a second degree polynomial function. The $x$-intercept of this polynomial fit was the torsional spring constant used in all of our simulations. The torsional spring constant value we used in the simulations is 0.0023 $kg\ m^2\ rad^{-1}\ s^{-2}$ (see Results).

### *2.4 Results*

*Torsional spring constant measurements*

Moths which were in the freezer for 10 minutes prior to head excision had a torsional spring constant of 0.0023229 +/- 0.00071788 $kg\ m^2\ rad^{-1}\ s^{-2}$ (mean +/- standard deviation). Moths which were in the freezer for 1 hour prior to head excision had a torsional spring constant of 0.0033906 +/- 0.0019621 $kg\ m^2\ rad^{-1}\ s^{-2}$ (mean +/- standard deviation). We decided to use a value within the range of the moths which were in the freezer 10 minutes prior to head excision because such moths have material properties more directly relevant to the live moths.

*Simulated flight: non-dimensional tracking error*

Non-dimensional tracking error denotes the 2-dimensional rectilinear distance between the final state of the model in a 20 ms simulation run time, and the goal position normalized to body length ($L_1 + L_2$, constant for all simulations) of the simulated moth. A Kruskal-Wallis one-way analysis of variance test showed at least one of the groups were significantly different from the other (Kruskal-Wallis, $\chi^2 = 294.14$, $df = 7$, $P = 2.2\text{e-}16$): the Dunn's test for multiple comparisons revealed the treatments which had the lowest non-dimensional tracking error were the two fully actuated treatments for the regular-sized abdomen, and one underactuated treatment for the reduced mass abdomen (regular-sized abdomen "fa" and "fs" in Figure 2.3a, and reduced mass abdomen "us").

*Simulated flight: cost of transport*

The cost of transport is defined as the non-dimensional work normalized to the weight of the simulated insect multiplied by the distance it traveled in the 20 ms time frame. Cost of transport was lowest for the regular-sized abdomen fully-actuated simulations (Figure 2.3b, treatments "fa" and "fs") and were significantly different from the other statistical groupings (Kruskal-Wallis $\chi^2 = 295.27$, $df = 7$, $P = 2.2\text{e-}16$).

Energy expenditure was minimized for fully actuated treatments. Decreasing the abdomen mass by 90% yields flight dynamics similar to a normal abdomen (see Appendix, Figures 2.4, 2.5) for the underactuated and location of applied force shifted treatments. However, the cost of transport is higher for all reduced abdomen size treatments than the fully actuated, regular-sized abdomen treatments.

*Moth free flight: incidence of flight*

One metric to observe any differences between the two treatments is the incidence of flight. After dark adaptation, moths were brought into the darkened arena and allowed 10 minutes to initiate flight. Flight or no flight was scored and compiled. Of 40 experimental treatment trials, 7 trials resulted in moth flight. Of 37 sham treatment trials, 18 resulted in moth flight. The incidence of flight is much lower in experimental treatment moths (17.5%) than in sham

treatment moths (48.6%).

*Moth free flight: kinematics and path metrics*

For all moths which successfully flew, we used various metrics to evaluate the dynamics of the flight paths, and observe the differences between the two treatments. These metrics included root mean square (RMS) velocity, RMS acceleration, tortuosity, box dimension, the log-log transform of the spatial frequencies of flight path, and flight duration.

The RMS velocity was not significantly different for both the experimental and sham treatments (Wilcoxon rank sum exact test, $P = 0.6947$). The RMS acceleration was not significantly different for both the experimental and sham treatments (Wilcoxon rank sum exact test, $P = 0.6505$). The sliding window tortuosity was not significantly different for both the experimental and sham treatments (Wilcoxon rank sum exact test, $P = 0.261$). The box dimension was not significantly different for both the experimental and sham treatments (Wilcoxon rank sum exact test, $P = 0.6495$). Neither the slopes nor intercepts of the log-log transform of the spatial frequencies of tortuosity were significantly different between experimental and sham treatments (Wilcoxon rank sum exact test, slope: $P = 0.9408$; intercept $P = 0.3312$ ).

However, the flight duration was significantly different for both the experimental and sham treatments (Wilcoxon rank sum exact test, $P = 0.01561$). This implies inhibition of abdominal movements yields shorter flight bouts for experimental treatment moths.

*Double-blind scoring of rolling maneuvers*

The incidence of rolls in the experimental treatment was 45 of 96 (46.9%). The incidence of rolls in the sham treatment was 23 of 112 (20.5%). This difference was statistically significant (Wilcoxan rank sum exact test, $W = 132$, $P = 0.01332$). This implies inhibition of abdominal movements yields a greater incidence of rolls for experimental treatment moths, although it remains unclear if this is a behavioral compensation or an inertial consequence of the abdominal restriction.

## *2.5 Discussion*

In this study we have provided both theoretical and experimental evidence that abdominal motions can play a critical role in flight control. This is shown in both the inertial dynamics model of this study and in experimental treatments of freely flying hawkmoths. Three key results arise from our computational analysis. First, our computational approach, inspired by Model-Predictive Control (MPC), successfully predicts forces and torques required to accomplish the complex motor task of tracking a moving target. Second, we find that both fully actuated and underactuated models of control can successfully accomplish these tasks. However, the error associated with tracking is generally greater for underactuated systems. Third, we find that the energetic cost of transport, as measured by the energy divided by the product of the thorax muscle weight and distance traveled, depends quite strongly on the abdominal motions. We showed that all computational model variations were able to successfully track the vertically oscillating goal, yet two treatments in particular minimized the cost of transport (both fully actuated, regular-sized abdomen models, see Figure 2.3b, left columns, treatments "fa" and "fs"). We also showed that when abdomen motion was inhibited in freely flying moths attempting to feed from a stationary 3D printed flower, yielded a drastically lower incidence of flight, and for moths which successfully flew, the duration of the flight bouts were significantly shorter and less stable.

*Inverse solutions using MPC-inspired models*

Flight control is a non-linear problem in which the inverse solution–finding forces and torques required to follow a specified path–can be quite challenging. As mentioned previously, a number of outstanding studies have solved this inverse problem using a variety of approaches. For example, Hedrick and Daniel [59] used a genetic algorithm melded with a simplex optimization in which 10 parameters were used to solve the inverse problem of hovering and level flight control with the same four degrees of motion we allowed in our simulations. With 10 control parameters, they simulated an overactuated system, particularly given that the state space is dominantly four degrees of freedom. Nonetheless, that study showed it was possible to fix all but two kinematic parameters and still accomplish successful flight

([59], Table 2). Interestingly, that study also showed that a single underactuated kinematic parameter set could perform the task of hovering, albeit with considerably higher error. This particular underactuated kinematic parameter set was the inspiration for our study as underactuated systems have been of particular interest in synthetically designed engineered systems [60, 86].

Genetic algorithms have been used elsewhere in studies of flight control including but not limited to: identifying actuator placement, controller design, vehicle design to launch small satellites, and other general optimization processes [121]. While, to our knowledge, only Hedrick and Daniel [59] incorporate the use of a genetic algorithm for computing the inverse problem of hovering in a biological context, a similar approach was used to compute wing kinematics in flight that minimized the energy required for hovering [12].

Analogously, MPC approaches for flight control have gained considerable attention in recent literature including on-board control of quadrotors [17], target tracking in fixed wing aircraft [120, 140], and other synthetic systems [115]. However, to our knowledge, it has not been widely deployed as a method for exploring natural flight systems. MPC approaches also lend themselves to future studies in which deep neural networks (DNNs) can be developed, refined, and influence the basis of problems with otherwise infinite state-space permutations. In summary, the implementation of MPC approaches coupled with DNNs can provide unique insight into a vast array of physically bounded, biologically relevant questions.

*Fully actuated and underactuated controls*

For our model of a flying moth moving with four degrees of freedom–in our cases two translational $(x, y)$ and two rotational $(\theta, \phi)$ directions–we explored two control scenarios, one in which the model is fully actuated using four control inputs and one in which it is underactuated, where we use just three control inputs. Formally, underactuated systems are those for which the control system cannot accomplish any acceleration in some of the degrees of freedom at any instant in time [116]. Underactuated systems have received considerable attention in recent years, often because they are commonly seen in a variety of biological systems. For example, Deng *et. al* [137] show that time invariant averaging theory can be

used for controlling bioinspired insect robots that are underactuated. Similar approaches have been used for underactuated fish-like robots [89].

Similar to the time-averaging methods above, in our underactuated scenario, we use a fixed force and fixed abdominal torque during the equivalent time of half a wing stroke to effect control, effectively serving as a stroke averaged control. As we noted above, this approach leads to effective tracking, though an intriguing trade-off appears. When the abdominal mass is close to that observed in *Manduca* the cost of transport in both underactuated configurations ("ua" and "us") is greater than that associated with the fully actuated system ("fa" and "fs") (Figure 2.3b). If, however, the abdominal mass is drastically smaller, as in our reduced mass abdomen models, the cost of transport is actually greater for the fully actuated system. In that case the underactuated system for both the normal abdominal mass and the reduced mass are similar in magnitude (Figure 2.3b).

Taken together, the flight dynamics (Appendix, Figures 2.4, 2.5), non-dimensional tracking error (Figure 2.3a), and cost of transport (Figure 2.3b) yield conflicting results with the findings of [59] (see Hedrick and Daniel, Table 2). For the normal mass simulations, a higher non-dimensional tracking error, and cost of transport was shown for both underactuated treatments ("ua" and "us") when compared to the fully actuated treatments ("fa" and "fs") which is in accordance with Hedrick and Daniel [59]. However, the flight dynamics (Appendix, Figures 2.4, 2.5) reveals that while the model can track rectilinear motions accurately $(x, y)$, and even maintain a relatively reasonable head-thorax rotation ($\theta$, with some abrupt jostling), the abdominal motions spin indefinitely for both underactuated configurations ("ua" and "us"). This dramatic abdominal spin demonstrates a conflict with the findings of Hedrick and Daniel [59].

In all instances when applied wing torques or offset origin of wing forces are absent from the system, we observe unstable dynamics ("ua" treatment in Appendix, Figures 2.4, 2.5), high energy expenditure, and high tracking error (Figure 2.3, "ua" models). This implies the necessity of an applied torque, regardless of how miniscule, is essential for dynamical stability. Interestingly, the pitch moment of inertia about the center of mass for the entire head/thorax and abdomen system will depend on abdominal flexion angle: greater flexion has a lower pitch moment of inertia.

*Restricting natural abdominal motions compromises flight*

For freely flying moths given the task of feeding from a stationary 3D printed flower, our sham treatment moths flew successfully with no discernible inhibition to their flight pattern. Flight incidence was dramatically decreased for moths given this same task with the carbon fiber rod restricting their abdominal motion. Additionally, if moths flew, various flight dynamics (e.g. velocities, path tortuosity) were not significantly different between treatments, except for length of flight duration. This indicates the experimental treatment moths that were able to fly were inhibited to the point of having shorter flight bouts.

While simple metrics of flight dynamics such as speeds, accelerations, or tortuosities did not yield significant differences between moths with restricted abdominal motions and control individuals, moths in the experimental treatment group were observed to engage in a higher incidence of rolling motions than sham treatment moths. We suspect that abdominal flexion could increase the rotational moment of inertia in the roll axis: a straight cylinder has a lower roll moment of inertia than a bent cylinder of identical length and mass. Indeed, maneuvering via abdominal flexion may allow roll motions when straight and roll stability when bent.

Similarly, this inhibition of abdominal movements is shown to have adverse effects on other animals as seen in a number of other studies. For example, juvenile mantids that had their abdominal segments restricted by superglue resulted in slower rotations necessary to complete a jump [20], sometimes causing them to crash head-first into their task goal–an otherwise easy to accomplish task for normal juvenile mantids. Wingless aphids passively correct their body posture when falling without the use of their nervous system (though achieve a better rate of body posture correction while alive, [104]) which indicates a purely physical method of aerial righting. At critical stages of aerial righting, wingless nymphal stick insects actively use their legs to reorient while falling [141]. Gliding ants (wingless ant workers) apply active control over their aerodynamic forces when righting their path back to tree trunks [91] despite their lack of having aerodynamically streamlined appendages to accomplish this task.

Future work could include 3D motion tracking of moths using the same vertically os-

cillating signal in our MPC-inspired model on live moths. This potential new study could also include varying degrees of inhibited abdominal motion ranges (*i.e.*, potential halfway degrees of treatment–sticks which get stiffer as flexion increases).

## *2.6 Conclusion*

*Airframe deformation: inertial reconfiguration contributes to flight control*

Taken together, both the computational and experimental results point to an important role for inertial reconfiguration of body elements in movement control. While wings are clearly the most important structures for animal flight control, this study shows that inertial components of non-wing structures also play an important role.

## *2.7 Appendix*

*Model formulation and methods*

The Euler-Lagrange equations form a system of four coupled second order ordinary differential equations for the state variables $q$, ($q = x, y, \theta, \phi$)

The Euler-Lagrange equation is written in the following general form:

$$\frac{\mathrm{d}}{\mathrm{d}t}\frac{\partial T^*}{\partial \dot{q}} - \frac{\partial T^*}{\partial q} + \frac{\partial V}{\partial q} + \frac{\partial D}{\partial \dot{q}} = e_q^s \tag{2.9}$$

Where $q$ is a placeholder for a flow variable ($x$, $y$, $\theta$, $\phi$). $x$ and $y$ are with respect to the standard Cartesian coordinates, $\theta$ is the angle of the head-thorax mass with respect to the x-axis, and $\phi$ is the angle between the midline of the abdomen with respect to the x-axis (Figure 2.1b).

Furthermore, $T^*(p)$ is defined as the kinetic co-energy, V is defined as the potential energy, $D(p)$ is defined as the dissipative energy, and $e_q^s$ the external effort exerted that affects the respective flow variable (either $x$, $y$, $\theta$, $\phi$). This yields four Euler-Lagrange equations for the four variables of this model:

$$\frac{\mathrm{d}}{\mathrm{d}t}\frac{\partial T^*}{\partial \dot{x}} - \frac{\partial T^*}{\partial x} + \frac{\partial V}{\partial x} + \frac{\partial D}{\partial \dot{x}} = e_x^s \tag{2.10}$$

$$\frac{\mathrm{d}}{\mathrm{d}t}\frac{\partial T^*}{\partial \dot{y}} - \frac{\partial T^*}{\partial y} + \frac{\partial V}{\partial y} + \frac{\partial D}{\partial \dot{y}} = e_y^s \tag{2.11}$$

$$\frac{\mathrm{d}}{\mathrm{d}t}\frac{\partial T^*}{\partial \dot{\theta}} - \frac{\partial T^*}{\partial \theta} + \frac{\partial V}{\partial \theta} + \frac{\partial D}{\partial \dot{\theta}} = e_\theta^s \tag{2.12}$$

$$\frac{\mathrm{d}}{\mathrm{d}t}\frac{\partial T^*}{\partial \dot{\phi}} - \frac{\partial T^*}{\partial \phi} + \frac{\partial V}{\partial \phi} + \frac{\partial D}{\partial \dot{\phi}} = e_\phi^s \tag{2.13}$$

The positional vectors of our two masses with respect to the thorax-abdomen joint are the following:

$$\vec{r_1} = (x + L_1 cos\theta)\hat{i} + (y + L_1 sin\theta)\hat{j} \tag{2.14}$$

$$\vec{r_2} = (x + L_2 cos\phi)\hat{i} + (y + L_2 sin\phi)\hat{j} \tag{2.15}$$

Where $L_1$ is a fixed length between the thorax-abdomen joint to the center of the head-thorax mass (Figure 2.1b). Similarly, $L_2$ is a fixed length between the thorax-abdomen joint to the center of the abdomen mass (Figure 2.1b).

The velocity vectors for each of the two masses are simply the derivatives of the positional vectors with respect to time as follows:

$$\dot{\vec{r_1}} = (\dot{x} - L_1\dot{\theta} sin\theta)\hat{i} + (\dot{y} + L_1\dot{\theta} cos\theta)\hat{j} \tag{2.16}$$

$$\dot{\vec{r_2}} = (\dot{x} - L_2\dot{\phi} sin\phi)\hat{i} + (\dot{y} + L_2\dot{\phi} cos\phi)\hat{j} \tag{2.17}$$

The kinetic energy of the system is as follows:

$$T^* = \frac{1}{2}m_1\dot{\vec{r_1}}\dot{\vec{r_1}} + \frac{1}{2}I_1\dot{\theta}^2 + \frac{1}{2}m_2\dot{\vec{r_2}}\dot{\vec{r_2}} + \frac{1}{2}I_2\dot{\phi}^2 \tag{2.18}$$

Where $m_1$ is the mass of the head-thorax, $I_1$ is the moment of inertia of the same mass, $m_2$ is the mass of the abdomen, and $I_2$ is the moment of inertia of the abdomen. When the velocity vectors are substituted in, (2.18) becomes the following form:

$$\begin{aligned} T^* = & \frac{1}{2}m_1(\dot{x}^2 + \dot{y}^2 + 2L_1\dot{\theta}(\dot{y}cos\theta - \dot{x}sin\theta) + L_1^2\dot{\theta}^2) \\ & + \frac{1}{2}I_1\dot{\theta}^2 \\ & + \frac{1}{2}m_2(\dot{x}^2 + \dot{y}^2 + 2L_2\dot{\phi}(\dot{y}cos\phi - \dot{x}sin\phi) + L_2^2\dot{\phi}^2) \\ & + \frac{1}{2}I_2\dot{\phi}^2 \end{aligned} \tag{2.19}$$

The potential energy of the system is as follows:

$$\begin{aligned} V = & \frac{1}{2}\kappa((\phi - \theta - \pi) - (\phi_o - \theta_o - \pi))^2 \\ & + m_1g(y + L_1sin\theta) \\ & + m_2g(y + L_2sin\phi) \end{aligned} \tag{2.20}$$

Where $\kappa$ is the torsional spring constant of the joint that connects the thorax to the abdomen, $g$ is the acceleration due to gravity, $\phi_o$ is the initial abdomen angle, and $\theta_o$ is the initial head-thorax angle. And $\beta_{rest}$ is defined as: $\phi_o$ - $\theta_o$ - $\pi$.

The dissipative energy of the system is as follows:

$$D = \frac{1}{2}\eta(\dot{\phi} - \dot{\theta})^2 \tag{2.21}$$

Where $\eta$ is the torsional damping constant of the joint that connects the thorax to the abdomen. The work done by the applied efforts to the system are as follows:

$$\delta W_x = Q_x\delta x \tag{2.22}$$

$$\delta W_y = Q_y\delta y \tag{2.23}$$

$$\delta W_\theta = Q_\theta\delta\theta \tag{2.24}$$

$$\delta W_\phi = Q_\phi\delta\phi \tag{2.25}$$

Therefore, the applied efforts are as follows:

$$\begin{aligned} e_x^s = Q_x =& Fcos(\theta+\alpha) - \frac{1}{2}\rho_a S_{head} C_{dhead} \mid \dot{x} \mid \dot{x} \\ & - \frac{1}{2}\rho_a S_{abdo} C_{dabdo} \mid \dot{x} \mid \dot{x} \end{aligned} \tag{2.26}$$

$$\begin{aligned} e_y^s = Q_y =& Fsin(\theta+\alpha) - \frac{1}{2}\rho_a S_{head} C_{dhead} \mid \dot{y} \mid \dot{y} \\ & - \frac{1}{2}\rho_a S_{abdo} C_{dabdo} \mid \dot{y} \mid \dot{y} \end{aligned} \tag{2.27}$$

$$e_\theta^s = Q_\theta = \tau_{abdo} + \tau_{wing} + L_3 Fsin(\alpha) \tag{2.28}$$

$$e_\phi^s = Q_\phi = -\tau_{abdo} \tag{2.29}$$

Where $F$ is the averaged aerodynamic lift force over the course of the 20 ms simulation time period caused by the flapping wings of the insect, $\alpha$ is the angle of the aerodynamic lift force with respect to the midline of the head-thorax mass, $\rho_a$ is the density of air, $S$ is the surface area of the insect which is experiencing aerodynamic drag (modeled as a sphere). $C_{dx}$, and $C_{dy}$ are the coefficients of drag in the x-direction and in the y-direction respectively, $\tau_{abdo}$ is the torque applied to the thorax-abdomen joint for flight correctional purposes and/or to counteract external perturbations (note: conservation of angular momentum requires an equal and opposite torque applied by the abdomen), and $L_3$ is the fixed length between the thorax-abdomen joint to the center of the aerodynamic lift of the thorax-abdomen joint to the center of aerodynamic lift of the insect located in the head-thorax mass.

Taking the appropriate derivatives of equations 2.19-2.21 as required by equations 2.10-2.13, yield the following four equations of motion (note, not all derivatives mentioned in equations 2.10-2.13 are necessary):

Equation of motion in the x-direction:

$$\begin{aligned} & (m_1+m_2)\ddot{x} - m_1 L_1 \ddot{\theta} sin\theta - m_2 L_2 \ddot{\phi} sin\phi \\ & - m_1 L_1 \dot{\theta}^2 cos\theta - m_2 L_2 \dot{\phi}^2 cos\phi = Fcos(\theta+\alpha) \\ & - \frac{1}{2}\rho_a S_{head} C_{dhead} \mid \dot{x} \mid \dot{x} - \frac{1}{2}\rho_a S_{abdo} C_{dabdo} \mid \dot{x} \mid \dot{x} \end{aligned} \tag{2.30}$$

Equation of motion in the y-direction:

$$\begin{aligned}&(m_1+m_2)\ddot{y}+m_1L_1\ddot{\theta}cos\theta+m_2L_2\ddot{\phi}cos\phi\\&-m_1L_1\dot{\theta}^2sin\theta-m_2L_2\dot{\phi}^2sin\phi+(m_1+m_2)g\\&=Fsin(\theta+\alpha)-\frac{1}{2}\rho_aS_{head}C_{dhead}\mid\dot{y}\mid\dot{y}\\&-\frac{1}{2}\rho_aS_{abdo}C_{dabdo}\mid\dot{y}\mid\dot{y}\end{aligned}\tag{2.31}$$

Equation of motion in the theta-direction:

$$\begin{aligned}&(m_1L_1^2+I_1)\ddot{\theta}-m_1L_1\ddot{x}sin\theta+m_1L_1\ddot{y}cos\theta\\&-\kappa((\phi-\theta-\pi)-(\phi_o-\theta_o-\pi))+m_1gL_1cos\theta\\&-\eta(\dot{\phi}-\dot{\theta})=\tau_{abdo}+\tau_{wing}+L_3Fsin\alpha\end{aligned}\tag{2.32}$$

Equation of motion in the phi-direction:

$$\begin{aligned}&(m_2L_2^2+I_2)\ddot{\phi}-m_2L_2\ddot{x}sin\phi+m_2L_2\ddot{y}cos\phi\\&+\kappa((\phi-\theta-\pi)-(\phi_o-\theta_o-\pi))+m_2gL_2cos\phi\\&+\eta(\dot{\phi}-\dot{\theta})=-\tau_{abdo}\end{aligned}\tag{2.33}$$

These equations of motion (Equations 2.30 - 2.33) are the ones used in our inertial dynamics model.

*Loss function weighting coefficients*

The loss function weighting coefficients are defined in Table 2.3. These coefficients ensure that deviations from our goal position and rotation heavily penalize rectilinear motion deviations $(x, y)$, with head motion deviations penalized secondarily as strong $(\theta)$. The derivatives of these motions $(\dot{x}, \dot{y}, \dot{\theta})$ are not as strongly penalized.

*Prescribed goal motion frequencies and amplitudes*

The frequencies of the prescribed goal motion are 11 prime number frequencies drawn directly from Roth *et. al* [107]. The purpose of these prime number frequencies is two-fold: 1) to determine if the output of the system is linear or non-linear, 2) to ensure that any

potential harmonics of the system can be distinguished from their basal frequencies (*i.e.* not overlap).

The amplitude(s) of the goal motion signal decrease by a prescribed factor as shown in equation 2.34. This amplitude decrease is necessary to ensure that the derivative of the models tracking this goal do not accelerate substantially causing unwanted instabilites in the system.

$$A_n = \frac{A_1}{2\pi f_n} 2\pi f_1 \tag{2.34}$$

*Derivation of torsional spring constant system*

As stated in Methods, the moths used in this experiment can be modeled as a system of two masses (thorax and abdomen) connected with a torsional spring constant and a torsional damper (Figure 2.1b), and represented by Equation 2.35

$$\tau = \kappa\theta + \eta\dot{\theta} + I\ddot{\theta} \tag{2.35}$$

Which can be transformed into Equation 2.36

$$T = \kappa\Theta + \eta(i\omega)\Theta + -I(\omega^2)\Theta \tag{2.36}$$

This can be rearranged into a torque-angle ratio form as seen in equation 2.37

$$\frac{T}{\Theta} = \kappa + i\eta\omega - I\omega^2 \tag{2.37}$$

The system yields two components: the real component (Equation 2.38), and the imaginary component (Equation 2.39).

$$Real\left(\frac{T}{\Theta}\right) = \kappa - I\omega^2 \tag{2.38}$$

$$Imag\left(\frac{T}{\Theta}\right) = i\eta\omega \tag{2.39}$$

The real component corresponds to the torsional spring constant and can be rearranged into Equation 2.8 (see Methods) to calculate the torsional spring constant. The imaginary component corresponds to the torsional damping coefficient which is not calculated in this study, but rather, a value previously calculated by Dyhr *et. al* [45] is used.

*Measurements of body segment masses*

Five male hawkmoths, and five female hawkmoths had their total mass, head, thorax, and abdomen weighed. For a full distribution of these values, see Table 2.4.

## *2.8 Acknowledgments*

We thank Mark Jankauski, and Chaoyi Yang for their assistance in model development and parallelization of the code. We are grateful to Alison Weber for her critical feedback on the manuscript. This work was supported by AFOSR grants FA9550-14-1-0398 and FA9550-19-1-0386 to TLD, an NSF Graduate Research Fellowship to JB, an Human Frontier Science Program Long-term Postdoctoral Fellowship to TD.

## *2.9 Figures for Chapter 2*

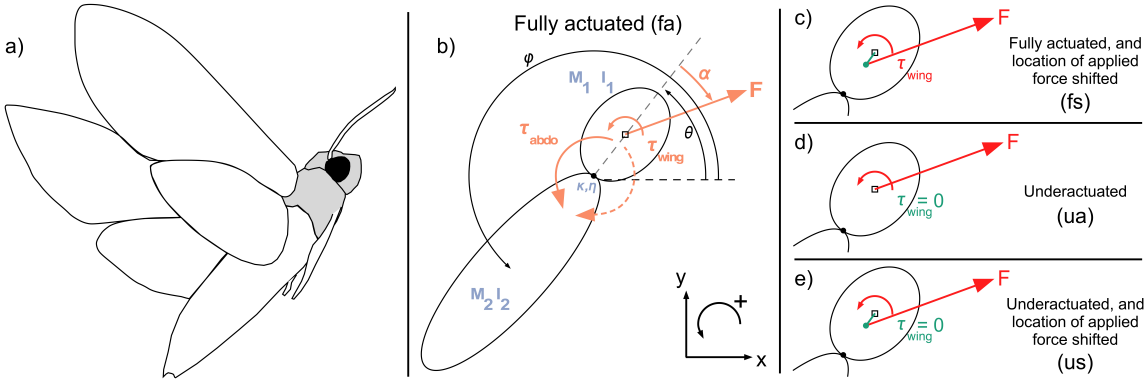


Figure 2.1: **Model basis and modifications.** The model has mechanical properties described in blue, and the randomized applied efforts in red. Modifications to the basic model are highlighted in green in (c-e). a) a tracing of a hawkmoth in flight. b) The fully actuated model ("fa") has two spheroids of prescribed masses and moment of inertia. Reference frame describes positive motion coordinates and rotational motions (counterclockwise). The spheroid of the head-thorax mass is indicated in grey. c) The fully actuated and location of applied force shifted treatment ("fs") allows for an additional implicit torque on the system. d) The underactuated treatment ("ua") is identical to the fully actuated treatment (b), with the applied wing torque set to zero. e) The underactuated with location of applied force shifted treatment ("us") is most similar to treatment (c) but with the applied wing torque set to zero.

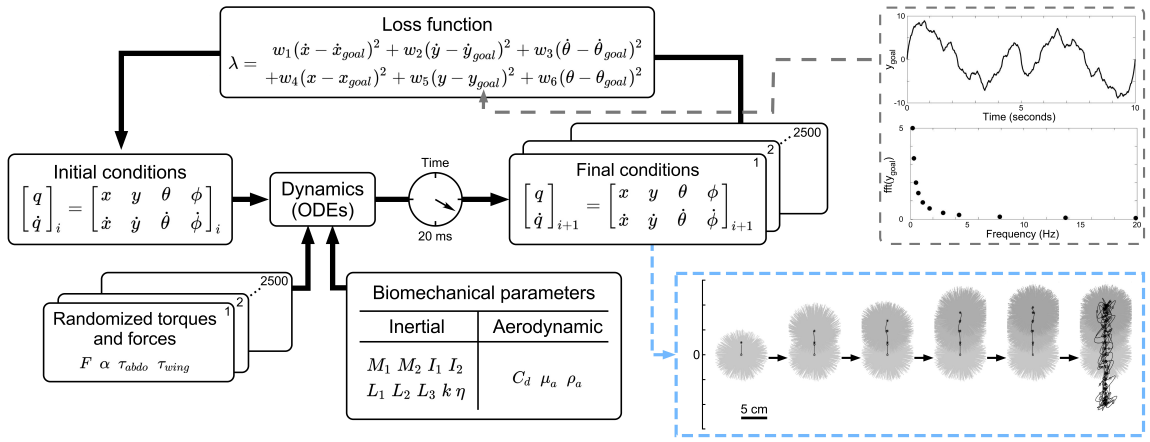


Figure 2.2: **Methods for simulating trajectories.** The model has a prescribed set of biomechanical properties: both inertial parameters (masses: $M_1$, $M_2$, moments of inertia: $I_1$, $I_2$, vector lengths: $L_1$, $L_2$, $L_3$, torsional spring constant: $\kappa$, and torsional damping coefficient: $\eta$) and aerodynamic parameters (coefficient of drag: $C_d$, dynamic viscosity of air: $\mu_a$, and density of air: $\rho_a$). Each simulation begins with a prescribed set of initial conditions (the set of positions: $q$ and their respective velocities: $\dot{q}$). Monte-Carlo methods randomized the applied forces (magnitude of force: $F$, direction of force: $\alpha$) and torques (abdominal torque: $\tau_{abdo}$, and wing torque: $\tau_{wing}$). There are a set of 2500 randomized forces and torques for each time 20 ms time period, yielding the final conditions. The initial conditions, randomized torques and forces, and biomechanical parameters are all passed into the ordinary differential equations (ODEs) of the system (to see the ODEs and their full derivations, see Appendix Equations 2.30 - 2.33). A loss function ($\lambda$) selects the trajectory with the lowest loss function value. The loss function contains various weights ($w_{1-6}$, see Appendix Table 2.3) which penalize deviations from $y$ and $x$ more than $\theta$. The composition of the vertically oscillating signal $y_{goal}$ is noted in the grey dashed box on the upper right. The time series of the $y_{goal}$ is displayed for a 10 second time period, the frequency components of this signal are noted in the figure below. The values of amplitude and frequency are noted in Appendix Table 2.1. The trajectory selected by the loss function uses the values 25% through the trajectory as the new initial conditions for the next 20 ms time period. A visualization of the trajectories and the selection of one trajectory through time is included in the light blue dashed box on the lower right.

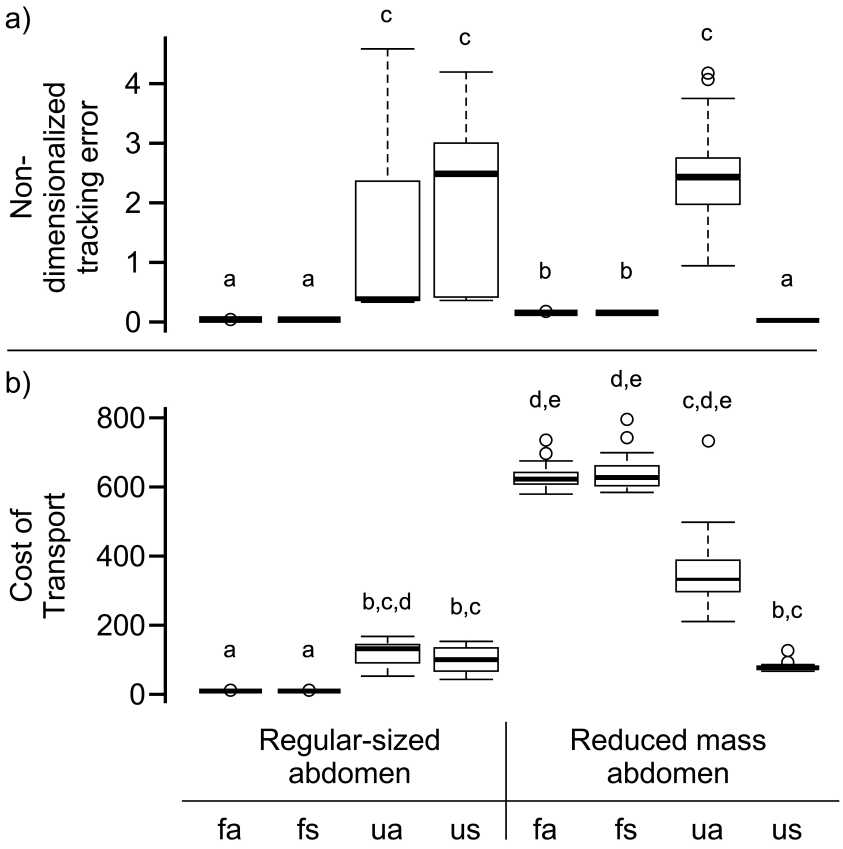


Figure 2.3: **Evaluating simulated flight performance.** Panel (a) is the non-dimensional tracking error. Panel (b) is the Cost of Transport. The regular-sized abdomen is based off of our measured parameters (Appendix, Table 2.2), and the reduced mass abdomen is an abdomen mass decreased by ∼90% to evaluate the role of effectively eliminating the abdomen mass from the system. The grouping of four treatments on the left side of the panel correspond to the regular-sized abdomen, while the grouping of four treatments of the right side of the panel correspond to the reduced mass abdomen. For both panels, and both sizes of abdomen all treatment shorthands are defined as follows: fully actuated ("fa"), fully actuated and location of applied force shifted treatment ("fs"), underactuated ("ua"), and underactuated with location of applied force shifted treatment ("us"). All results here are based on 40 full simulations per treatment. Each full simulation run time of 10 seconds of simulated flight. The letters above each box plot indicate statistical groupings. All statistical tests for significance were performed by a Kruskal-Wallis rank sum test. All statistical groupings were based on Bonferroni correction factor (*i.e.*, reject hypothesis if $P > 0.05/2$). For non-dimensional tracking error, all model modifications except both fully actuated regular-sized abdomen treatments (left columns, "fa" and "fs"), and the reduced mass "us" treatment had significantly higher non-dimensional tracking error ($P > 0.025$). For cost of transport, all model modifications except both fully actuated regular-sized abdomen treatments (left columns, "fa" and "fs") had significantly higher cost of transport ($P > 0.025$).

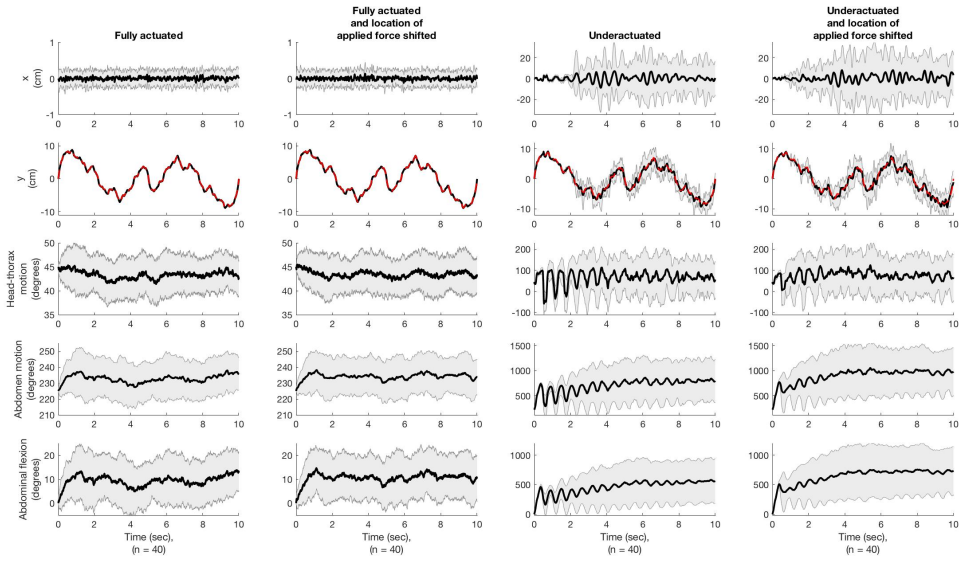


Figure 2.4: **Model dynamics output for all model variations of the regular-sized abdomen model.** All plots are with respect to time for a 10 second simulation period. Top row is the x-motion in cm. Second row is the y motion in cm (note the dashed red line is the goal motion of our vertically oscillating goal). The third row is the head-thorax ($m_1$) mass motion in degrees. The fourth row is the abdominal motion ($m_2$) in degrees. The bottom row is the abdominal flexion angle (i.e. difference between rows 4 and 3 respectively) in degrees. For all treatments, the model tracks the input y-motion well.

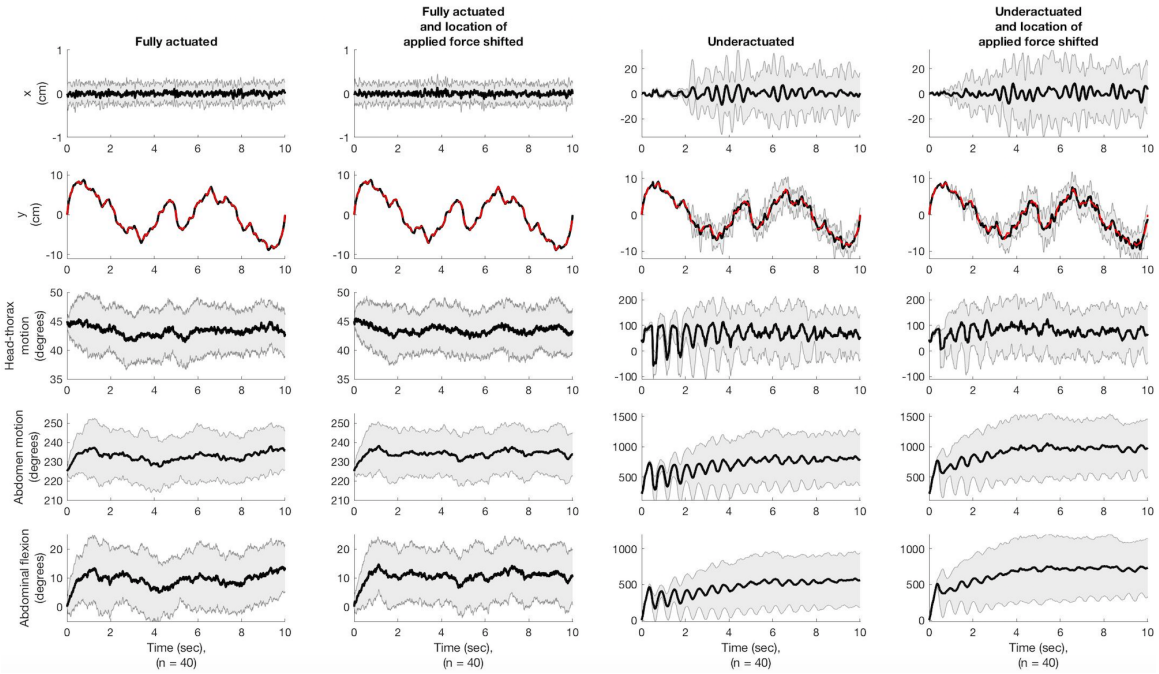


Figure 2.5: **Model dynamics output for all model variations of the reduced-sized abdomen model.** All plots are with respect to time for a 10 second simulation period. Top row is the x-motion in cm. Second row is the y motion in cm (note the dashed red line is the goal motion of our vertically oscillating goal). The third row is the head-thorax ($m_1$) mass motion in degrees. The fourth row is the abdominal motion ($m_2$) in degrees. The bottom row is the abdominal flexion angle (i.e. difference between rows 4 and 3 respectively) in degrees. For all treatments, the model tracks the input y-motion well.

### *2.10 Tables for Chapter 2*

### *2.11 Acknowledgments for Chapter 2*

We thank Mark Jankauski, and Chaoyi Yang for their assistance in model development and parallelization of the code. We are grateful to Alison Weber for her critical feedback on the manuscript. This work was supported by AFOSR grants FA9550-14-1-0398 and FA9550-19-1-0386 to TLD, an NSF Graduate Research Fellowship to JB, an Human Frontier Science Program Long-term Postdoctoral Fellowship to TD.

| Goal motion Frequency | Goal motion amplitude |
|---|---|
| 0.2 | 5 |
| 0.3 | 3.3333 |
| 0.5 | 2 |
| 0.7 | 1.4286 |
| 1.1 | 0.9091 |
| 1.7 | 0.5882 |
| 2.9 | 0.3448 |
| 4.3 | 0.2326 |
| 7.9 | 0.1266 |
| 13.7 | 0.0730 |
| 19.9 | 0.0503 |

Table 2.1: The prime number frequencies listed out in sequential order and their respective amplitudes. Amplitudes decreased with increasing frequency to prevent the system from going unstable.

| Mechanical property | Numerical value |
|---|---|
| $L_1$ | 0.908 cm |
| $L_2$ | 1.9 cm |
| $L_3$ | 0.75 cm |
| $a_{head}$ | 0.908 cm |
| $a_{butt}$ | 1.9 cm |
| $b_{head}$ | 0.5 cm |
| $b_{butt}$ | 0.75 cm |
| $\kappa$ | 23000 $cm^2g/(rad * s^2)$ |
| $\eta$ | 14075.8 $cm^2g/s$ From [45] |
| $\rho_{head}$ | 0.9 $g/cm^3$ |
| $\rho_{butt}$ | 0.4 $g/cm^3$ |
| $\rho_{air}$ | $1.18 * 10^{-3} g/cm^3$ |
| $\mu_{air}$ | $1.86 * 10^{-4} g/(cm * s)$ |
| $g$ | 980 $cm/s^2$ |

Table 2.2: The mechanical properties of the model are fixed throughout the duration of all simulations. All values were calculated from our own measurements and rounded as appropriate with the exception of one: the torsional damping coefficient $\eta$ which was previously measured in Dyhr *et. al* [45].

| Loss function weighting coefficients | | |
|---|---|---|
| Coefficient | Value | State variable assigned to: |
| $w_4$ | $10^9$ | $x$ |
| $w_5$ | $10^{10}$ | $y$ |
| $w_6$ | $10^{10}$ | $\theta$ |
| $w_1$ | $10^{-5}$ | $\dot{x}$ |
| $w_2$ | $10^{-5}$ | $\dot{y}$ |
| $w_3$ | $10^8$ | $\dot{\theta}$ |

Table 2.3: The weighting coefficients of the loss function penalize rectilinear motions higher than head-thorax motion. Such weights are critical for the loss function to function.

| Sex - Statistic | Total mass (g) | Head mass (g) | Thorax mass (g) | Abdomen mass (g) |
|---|---|---|---|---|
| *Male average* | 2.0758 | 0.135 (6.5%) | 0.584 (28.3%) | 1.0252 (49.3%) |
| *st.dev* | 0.145 | 0.0267 | 0.0449 | 0.126 |
| *min.* | 1.953 | 0.100 (5.1%) | 0.532 (24.9%) | 0.916 (46.0%) |
| *max.* | 2.302 | 0.173 (7.5%) | 0.651 (32.7%) | 1.187 (53.1%) |
| *Female average* | 3.550 | 0.183 (5.2%) | 0.686 (19.6%) | 2.206 (61.9%) |
| *st.dev* | 0.489 | 0.0264 | 0.0692 | 0.394 |
| *min.* | 2.790 | 0.148 (4.2%) | 0.618 (15.8%) | 1.660 (59.3%) |
| *max.* | 4.054 | 0.214 (6.2%) | 0.796 (22.7%) | 2.728 (67.3%) |

Table 2.4: Body segment mass distribution in grams. The mean and standard deviation values are calculated of the set of five male moths and five female moths respectively. The minimum and maximum of each set of five male moths and five female moths are also reported. The parenthetical values report the corresponding percentages of the value within the cell. Note the percentages summed across rows do not sum to 100% because 1) the wings and legs were not included in this measurement, and 2) the distribution reported reflects the value of the set (*i.e.*, the minimum/maximum values not be shared by the same individual moth).

Chapter 3

# ABDOMINAL MOVEMENTS IN INSECT FLIGHT RESHAPE THE ROLE OF NON-AERODYNAMIC STRUCTURES FOR FLIGHT MANEUVERABILITY II: PERFORMANCE TRADE-OFFS OF INERTIAL, ELASTIC, AND MORPHOLOGICAL DETERMINANTS OF FLIGHT

Jorge Bustamante, Jr. [1,∗], Tanvi Deora [1], and Thomas L. Daniel [1]

[**1**] Department of Biology, University of Washington, Box 351800, 98195, WA, USA

[*****] Primary author

## *3.1 Abstract*

While flight control due to wing shape, size, and motion has been studied extensively, a lesser studied mechanism of motion control and maneuverability includes the changing configuration of the body shape during flight (*i.e.* airframe configuration). Insects in particular change airframe configuration during flight, and span a broad range of shapes and sizes. Insects must also manage a variety of physiological and developmental, and elastic changes throughout their respective lifespans. An existing inertial-elastic dynamics model was modified to reflect the various morphological and inertial-elastic changes. This study modified a previously published inertial dynamics model to survey the flight performance trade-offs of two inertial-elastic modifications (*i.e.*, torsional spring constant, and abdominal mass). Additionally, our modified model explored these flight performance trade-offs in a broader morphospace by modifying size and morphological shape of a previously published inertial dynamics model. We find that 1) increasing abdominal mass reduced tracking error across size ranges while also increasing the mechanical work and cost of transport, and 2) increasing petiole length reduced tracking error across size ranges while also increasing the mechanical work and cost of transport. Additional nuanced trade-offs are discussed in this study. Such examination of inertial-elastic modifications, and morphospace modifications

can provide insight into flight stability of various insect morphologies, and further inform development of bioinspired robotics.

### *3.2 Introduction*

Flight control in insects involves a variety of both active and passive dynamics. Wings, for example, are actively controlled and also undergo significant, and aerodynamically important, deformations. Similarly, the entire body of insects is also subject to both active and passive deformations, largely mediated via abdominal flexion and extension which change the shape of the airframe, and thus alter the inertial dynamics of the body. While the consequences of wing size and shape have been subjects of considerable focus in the literature, far less is know about size and shape determinants of airframe deformations. There is a stunning range of body sizes and shapes among flying insects with body length range that spans 6 orders of magnitude, from aerial plankton such as fairy wasps (approximately 0.13 mm *Dicopomorpha echmepterygis*, [64]) to massive and extinct protodonates with a body length estimated to be about 350 mm).

Just as there is considerable variation in body size, so too is there variation in the body shape of flying insects. From elongated abdomens of dragonflies and damselflies to the stout body forms of flying beetles the shapes of airframes varies dramatically. Some particularly extreme examples include, at one extreme, the massive Hercules beetles with a thick ellipsoidal and, at another extreme certain Hymenoptera such as mud daubers (*Sceliphron caementarium*), or hover wasps (*Parischnogaster mellyi*) which have their thorax and abdomen separated by an impressively elongated abdominal segment known as the petiole.

In addition to taxonomic differences in size and shape, there are a host of physiological and developmental mechanisms that can contribute to significant changes in the mass distribution within the airframe of flying insects. For example, egg-development and deposition in gravid females, or ingesting particularly large meals. Female dragonflies, for example, increase their total mass by 125% +/- 64% (mean +/- standard deviation) in the time between the teneral stage and mature adulthood, while males increase their total mass by 84% +/- 69% (various species [6]); with one species where female dragonflies increase their total body mass by 248% in a matter of weeks (*Libellula luctuosa*). [6] describe the increase

in mass is observed in the thorax for males, and both the thorax and abdomen in females. As another example, female mosquitoes (*Anopheles quadrimaculatus*, *Anopheles albimanus*, and *Aedes aegypti*) have been observed to ingest more than their own body weight during a blood meal [68], [28], [55]. Mosquitoes of various species have been observed to fly at least one mile (most likely more) between the time of blood feeding and when the blood meal was completely digested [46]. Whether dragonflies or mosquitoes, or any other insect fauna which have a dramatic change in abdominal mass, successful flight is necessary to avoid predation and perpetuate the species.

While size and shape variation found among flying insects are important determinants of flight performance, there are also potential biomechanical differences in the ability to deform the airframe through active and passive mechanisms. Though this aspect of airframe reconfiguration has received far less attention, some earlier studies have shown that, in *Manduca sexta*, the joint between the abdomen and thorax is a critically damped spring [45] and provides stability in response to perturbations.

Over the broad span of size, shape, and inertial-elastic factors, flying insects are able to accomplish amazingly complex flight dynamics, including maneuvering through foliage, while minimizing collisions with foliage or other insects, attacking prey [29, 30, 97, 96, 131], and avoiding predators. Some insects also perform the task of hovering while feeding from moving flowers [107, 117]. One can naturally ask the question: given the broad range of morphologies (*i.e.* size and shape), and inertial-elastic changes (*i.e.* abdominal mass, and muscle flexion), what are the kinematic and energetic trade-offs that occur over a range of sizes, shapes and airframe mechanics?

Recently developed simulations of insect flight [21, 59, 125] provide inroads for exploring the theoretical trade-offs for insects of varying morphologies and inertial-elastic changes during flight maneuvers. In this study we use a model previously developed in Bustamante *et. al* [21] to to explore how size, shape, and airframe biomechanics influence the energetic and kinematic trade-offs in two flight tasks: hovering and target tracking.

## *3.3 Model formulation and methods*

We use an inertial dynamics model coupled with Monte Carlo methods previously developed [21] to address two different sets of modifications to a fully actuated model: 1) inertial-elastic modifications of abdominal mass ($m_2$), and torsional spring constant ($\kappa$), and 2) morphological modifications of: 1) all body length scales, and 2) petiole length extension. Our model simulates the dynamics of a flying moth as a reduced-order two-mass rigid body system consisting of four simultaneous non-linear ordinary differential equations that are solved numerically, similar to previous methods [21]. Both sets of modifications were tasked with two kinematic conditions associated with flower tracking: 1) a vertically oscillating flower (target tracking), and 2) stationary flower (hovering).

### *3.3.1 Base model formulation*

The base model for this study was previously developed, and is fully actuated ([21], "fa" treatment): two applied torques and two components of a wing-force vector control a four degree of motion model of a flexing flying airframe (Figure 3.1). In brief summary, the inertial dynamics model designates two spheroid masses: the head-thorax mass ($m_1$), and the abdominal mass ($m_2$). Each mass has a fixed moment of inertia ($I_1$ and $I_2$, head-thorax, and abdomen respectively). The two masses connect with a pin joint modeled by a torsional spring constant ($\kappa$) and a torsional damper ($\eta$) [7]. The model contains four external applied efforts: the aerodynamic force ($F$), the direction of the aerodynamics force ($\alpha$), the abdominal torque produced at the pin joint ($\tau_{abdo}$), and the wing torque ($\tau_{wing}$). The inertial dynamics model uses a right-handed coordinate system where $x$ motions are defined positive going right, $y$ are defined positive going upward. Likewise, all counter-clockwise rotations are defined as positive for the head-thorax mass ($\theta$), and the abdominal mass ($\phi$). Numerical values for all parameters of this base model are provided in Appendix, Table 2.2.

### *3.3.2 Modifications of the base model*

We varied two inertial-elastic parameters associated with airframe biomechanics: abdominal mass ($m_2$) and torsional spring constant ($\kappa$). We did so by modifying the base parameters by scale factors that span two orders of magnitude: the abdominal mass ($m_2$) and torsional spring constant ($\kappa$) with multipliers of 0.1, 1, and 10. These two parameter modifications yielded nine pairwise combinations of the modified parameters (see Figure 3.1).

In addition, we varied two size and shape parameters: a length scale factor (LSF) and the petiole length extension (PLE). LSF values were 0.5, 1, and 2 and applied to all linear dimensions in the model. The three petiole length extension (PLE) values were: 0, 0.2, and 0.4 (*i.e.*, no petiole, 20%, 40% of the respective body length of the model). These two morphological modifications also yielded nine pairwise combinations of the modified parameters.

### *3.3.3 Metrics of simulated flight performance*

Similar to Bustamante *et. al* [21], the model simulation flight performance was evaluated using three key metrics: (1) non-dimensional tracking error, (2) mechanical work, and (3) cost of transport. Additionally, we examined the fraction of each term relative to the total mechanical work and cost of transport (see Equations 3.2-3.3).

The non-dimensional tracking error (equation 3.1) is the rectilinear distance between the the predicted location of the 20 ms simulation ($x_{sim}$, and $y_{sim}$) and the goal position [21]. This term is normalized by dividing by the body length of the simulated organism. In this study, the body length of the set of morphological modification simulations vary by the LSF multiplier and PLE.

$$\frac{\sqrt{(x_{sim} - x_{goal})^2 + (y_{sim} - y_{goal})^2}}{body\ length} \tag{3.1}$$

The mechanical work is the sum of rotational work, and the work due to applied torques and applied forces:

$$Work = \vec{F} \mid \Delta\vec{r} \mid + \mid \tau_{wing}\theta \mid + \mid \tau_{abdo}\beta \mid \tag{3.2}$$

where $F$ is the vector of the applied wing force, $\tau_{wing}$ is the torque applied by the wing, $\tau_{\beta}$ is the torque applied by the abdominal flexors and extensors and $|\Delta\vec{r}|$ is defined as the distance traveled in each time step of the simulation. The angles $\theta$ and $\beta$ are defined in Figure 3.1. To represent energy expenditure of movement in space, the absolute value was taken of each term in equation 3.2.

The non-dimensional cost of transport describes the expenditure of movement in space normalized to the product of the weight and distance traveled by the simulated moth during the 20 ms interval [21]. The cost of transport is defined in equation 3.3.

$$C = \frac{Work}{m_1 g \mid \Delta\vec{r} \mid} \tag{3.3}$$

where $m_1$ is the head-thorax mass, and $g$ is the acceleration due to gravity.

### *3.3.4 Statistical analysis*

All flight performance metrics were statistically analyzed with the same statistical methods. We analyzed the effects of abdominal mass multiplier, torsional spring constant multiplier, length scale factor (LSF), and petiole length extension (PLE) on each of the flight performance metric: non-dimensional tracking error, mechanical work, and cost of transport for both hovering and vertically oscillating target using a linear regression model (custom codes written in Python can be found at https://github.com/JorgeBJr/multibodyDynamicsModel.gitGitHub). In addition to estimating the effect of individual parameters we also analyzed how the interaction of the inertial-elastic parameters: abdominal mass and torsional spring constant as well as the interaction of the two morphological parameters: length scale factor and petiole length extension effected the flight performance metrics.

To further evaluate the statistical significance between simulations of the same length scale factor or abdominal mass multiplier, a Kruskal-Wallis one-way analysis of variance test was performed on each trio of simulations. For all within-trio analyses, the statistical

groupings were denoted as brackets above the box plots (*i.e.*, "n.s." means not significant, and * means $P < 0.05/2$). All statistical groupings were determined by the Kruskal-Wallis test in R (kruskal.test), with a post hoc Dunn's test for multiple comparisons with Bonferroni correction.

## *3.4 Results*

For both target tracking and hovering (all inertial-elastic and morphological modifications) we evaluated simulated flight performance with three core metrics: 1) non-dimensional tracking error, 2) mechanical work required to perform the task, and 3) cost of transport (*i.e.*, non-dimensional mechanical work) for performing the task.

### *3.4.1 Non-dimensional tracking error for tracking a vertically oscillating signal (inertial-elastic modifications)*

The linear regression model reveals that the abdominal mass multiplier is negatively correlated with tracking error such that the lowest abdominal mass multiplier ($0.1 * m_2$) simulations, yielded the highest non-dimensional tracking error whereas the highest abdominal mass multiplier ($10 * m_2$) had the lowest non-dimensional tracking error for a vertically oscillating flower (Figure 3.2A). Neither the torsional spring constant multiplier by itself, nor the interaction of the abdominal mass multiplier and the torsional spring constant have a significant effect on the tracking error according to the linear regression. However, a Kruskal-Wallis one-way analysis of variance within each abdominal mass multiplier reveals that the torsional spring constant has an effect depending on the abdominal mass multiplier. Non-dimensional tracking errors are significantly different for the different torsional spring constant multipliers across the highest abdominal mass multiplier, as well as in the intermediate abdominal mass multiplier (post hoc Dunn's test for multiple comparisons with Bonferroni correction, $P < 0.05/2$, Figure 3.2A). All statistical significance and regression model coefficients are reported in Table 3.1.

### *3.4.2 Mechanical work for tracking a vertically oscillating signal (inertial-elastic modifications)*

Both the abdominal mass and the torsional spring constant have a significant effect on mechanical work. The highest mechanical work was with the highest abdominal mass multiplier ($10 * m_2$), whereas the lowest mechanical work was the intermediate abdominal mass multiplier simulations ($1 * m_2$), (Figure 3.2B). Mechanical work is significantly different for the different torsional spring constant multipliers across all abdominal mass multipliers (Kruskal-Wallis, post hoc Dunn's test for multiple comparisons with Bonferroni correction, $P < 0.05/2$, Figure 3.2B).

### *3.4.3 Cost of transport for tracking a vertically oscillating signal (inertial-elastic modifications)*

Increasing abdominal mass increases the cost of transport. The effect of torsional spring constant, however, depends on the abdominal mass: at a lower mass, the spring constant has a negative effect on cost of transport. Cost of transport is significantly different for the highest torsional spring constant in the lowest and intermediate abdominal mass, and only significantly different from the intermediate torsional spring constant for the highest abdominal mass (Kruskal-Wallis, post hoc Dunn's test for multiple comparisons with Bonferroni correction, $P < 0.05/2$, Figure 3.2C)

### *3.4.4 Non-dimensional tracking error for hovering (inertial-elastic modifications)*

Similar to the vertically oscillating signal, the abdominal mass multiplier is also negatively correlated with tracking error (Figure 3.3A). The torsional spring constant multiplier has a slight positive effect on non-dimensional tracking error, however, this effect is dependent on the abdominal mass. When the abdominal mass increases, the positive effect of torsional spring constant is reduced (linear regression model Table 3.2). Non-dimensional tracking error is significantly different across all torsional spring constants for the highest abdominal mass, but not for the lowest abdominal mass (Kruskal-Wallis, post hoc Dunn's test for multiple comparisons with Bonferroni correction, $P < 0.05/2$, Figure 3.3A).

### *3.4.5 Mechanical work for hovering (inertial-elastic modifications)*

Increasing both the abdominal mass and the torsional spring constant reduces the mechanical work (linear regression model Table 3.2). The highest torsional spring constant always significantly reduces the work as compared with the other torsional spring constant (Kruskal-Wallis, post hoc Dunn's test for multiple comparisons with Bonferroni correction, $P < 0.05/2$, Figure 3.3B).

### *3.4.6 Cost of transport for hovering (inertial-elastic modifications)*

Increasing abdominal mass results in a large increase in the cost of transport, whereas the torsional spring constant has only a slight negative effect (linear regression model Table 3.2). Cost of transport is significantly different for the highest torsional spring constant in the intermediate and highest abdominal mass (Kruskal-Wallis, post hoc Dunn's test for multiple comparisons with Bonferroni correction, $P < 0.05/2$, Figure 3.3C)

### *3.4.7 Non-dimensional tracking error for tracking a vertically oscillating signal (morphological modifications)*

Increasing both petiole length and length scale factor decreases the non-dimensional tracking error. Recall that the goal signal has a peak-to-peak amplitude of 10 cm (see Methods). Thus, the larger length scale factor simulated insects travel a shorter distance relative to the smaller length scale factor simulated insects. However, the effect of petiole length increase on the non-dimensional tracking error is dependent on the size itself: at larger sizes, the effect of petiole length is smaller (Table 3.1). Within each length scale factor, an increase in petiole length extension decreases the non-dimensional tracking error (Kruskal-Wallis, post hoc Dunn's test for multiple comparisons with Bonferroni correction, $P < 0.05/2$, Figure 3.4A). Notably, we observed a 3 fold decrease for non-dimensional tracking error by increasing petiole length to 40% of the body length.

### *3.4.8 Mechanical work for tracking a vertically oscillating signal (morphological modifications)*

Mechanical work increases with an increase in both length scale and petiole length. However, at larger length scales, increasing petiole length decreases work. Similar to non-dimensional tracking error, within each length scale factor, an increase in petiole length extension decreases the mechanical work especially at larger length scales (Kruskal-Wallis, post hoc Dunn's test for multiple comparisons with Bonferroni correction, $P < 0.05/2$, Figure 3.4B).

### *3.4.9 Cost of transport for tracking a vertically oscillating signal (morphological modifications)*

Again, increasing both the overall size as well as petiole length increases the cost of transport. Although at larger length scales, increasing petiole length decreases the cost of transport. An increase in petiole length extension significantly decreases the cost of transport for the smallest and largest length scales, however this trend was reversed for the intermediate length scale factor (Kruskal-Wallis, post hoc Dunn's test for multiple comparisons with Bonferroni correction, $P < 0.05/2$, Figure 3.4C).

### *3.4.10 Non-dimensional tracking error for hovering (morphological modifications)*

The trends for hovering are the same as those for the vertical oscillating signal: both the length scale and petiole length decrease the tracking error, however the effect of petiole length change depends on the length scale. At higher length scales, changing petiole length does not decrease the error as much. Also analogous to the vertically oscillating signal, within each length scale factor, an increase in petiole length extension decreases the non-dimensional tracking error (Kruskal-Wallis, post hoc Dunn's test for multiple comparisons with Bonferroni correction, $P < 0.05/2$, Figure 3.5A)

### *3.4.11 Mechanical work for hovering (morphological modifications)*

Like the vertically oscillating signal, increasing both the petiole length and length scale increases work. However, the effect of petiole length depends on the length scale: at larger

length scales, the effect of the petiole length reduces. Also like the vertically oscillating signal, within each length scale factor, an increase in petiole length extension decreases the mechanical work especially at larger length scales (Kruskal-Wallis, post hoc Dunn's test for multiple comparisons with Bonferroni correction, $P < 0.05/2$, Figure 3.5B)

### *3.4.12 Cost of transport for hovering (morphological modifications)*

Increasing both the length scale factor and petiole length increases the cost of transport. Interestingly, for hovering flight the effect of petiole length increases at larger size, thereby increasing the cost even further. An increase in petiole length extension significantly decreases the cost of transport for the smallest length scales, however this trend was reversed for both the intermediate and largest length scale factor (Kruskal-Wallis, post hoc Dunn's test for multiple comparisons with Bonferroni correction, $P < 0.05/2$, Figure 3.5C).

### *3.4.13 Trade-offs in components of mechanical work*

Recall that in this study, the mechanical work is composed of three terms (Equation 3.2). We visualized the averages of each work component as a fraction of the total mechanical work in Figure 3.6.

In the inertial-elastic modification simulations (Figure 3.6A), the dominant component of work is associated with airframe deformations ($|\tau_{abdo}\beta|$) for the smaller and intermediate abdominal masses. The airframe deformation component of work remains the dominant component of work for hovering in the simulations with the largest abdominal mass multiplier. However, the other two other components associated with wing forces and wing torques increase their contribution towards the total mechanical work. Lastly, the work component associated wing forces ($|\Delta\vec{r}|$) was dominant in the vertical flower tracking inertial-elastic modification simulations. This implies increasing wing forces is necessary to maintain vertical flower tracking as abdominal mass increases.

In the morphological modification simulations (Figure 3.6B), a different trend arises with respect to body length. For both the intermediate and larger length scale factor simulations, the dominant component of work is associated with airframe deformations

($|\tau_{abdo}\beta|$). Additionally, as length scale factor increased, the component of work associated with wing torques ($|\tau_{wing}\theta|$) increased. Yet for the smaller length scale factor simulations, wing forces were the dominant component of work.

### *3.5 Discussion*

In this study we have used a computational analysis of insect flight based on Model Predictive Control (MPC) approaches [21]. Using a four degree of freedom forward dynamics model for two-dimensional motions of a model insect with a deformable airframe, we examined the theoretical trade-offs between the precision of trajectory control versus the cost of that control for two, two-dimensional, flight tasks: tracking a vertically moving target or hovering, both of which correspond to an insect feeding from a flower while flying. In solving for four actuation variables (two rectilinear and two rotational controls) that determine control in this fully actuated model, we focused on the role of airframe deformation in flight control. In particular, we asked how size, shape, and body mechanical properties determine the precision and cost of flower tracking.

Three key results emerge from our study: (1) non-dimensional tracking error and the cost of transport (*i.e.* non-dimensional work) both increase with body size (2) the size dependence of these two performance metrics implies a trade-off between cost of transport and the control of the flight trajectory and (3) the underlying mechanical work components for flight control similarly trade-off with body size, with wing forces dominating for smaller sizes and airframe control dominating for larger sizes.

*Trajectory Tracking*

Various flight maneuvers including flower tracking have been studied for the hawkmoth (*Manduca sexta*), the model organism we have focused on here. Sprayberry and Daniel [118], for example, explored the energetics of tracking a sinusoidally moving flower and found that moths tracking flowers moving with higher oscillation frequencies necessarily incur greater acceleration costs, but those costs are tiny with respect to the energy gained through nectar feeding. Roth *et. al* [107] explored how visual and mechanosensory information combine as moths feed from horizontally moving flowers and found that both modalities play important,

parallel, and redundant roles in the sensorimotor control of flight. Similarly, Sponberg *et. al* [117] found that ambient light levels also influence floral tracking capabilities. Together these studies show that moths are capable of feeding from flowers during flight, and can do so for complex floral motions. But, because these studies logically focused on one model organism, their ability to explore variation in size, shape and mechanics were limited.

Our MPC approach was developed to explicitly explore how morphology and mechanics combine to determine flight performance. The model successfully provides relatively accurate motion tracking, regardless of the tracking task for all sizes, shapes, and mechanical properties we examined. In general the worst non-dimensional tracking occurred at the smallest sizes (smallest length scales or masses). That said, sizes varied by two orders of magnitude and the absolute tracking error is quite small – a maximum of $\sim$7 mm for floral motions of 10 cm excursions – and generally decreases with size (Figure 3.7). The errors in tracking we predict in this study are consistent with the level of error predicted in a previous analysis of the inverse problem of hovering flight control [59].

*Trade-offs between flower tracking accuracy and energetics*

The precision with which flight trajectories are controlled comes with some energetic cost – both in terms of absolute mechanical work and in terms of the non-dimensional cost of transport. In general the highest mechanical work and cost of transport occurred at the largest sizes (largest length scales or masses). This size dependence provides an interesting trade-off: lower tracking error (higher precision) comes at a higher energetic cost. Interestingly, we found that either smaller mass or smaller length scales are associated with lower work and cost. This trend stands in sharp contrast to the traditional size-dependent cost of transport which, for all modes of locomotion, decreases with increasing body size [5, 51, 52, 112]. The key difference between the traditional measures of cost and those developed here lies in how cost is measured. In our study, we simulate different sized animals undergoing identical tasks: all had to either hover at a fixed location or track a moving flower. In contrast, scaling studies of cost of transport have size dependent kinematics (*e.g.* speed, actuator frequency and amplitude), thus the kinematics vary.

To our knowledge, the trade-off between accuracy of trajectory control (hovering or flower tracking) and the cost of transport has not been previously examined. The increased cost of tracking for larger sizes is likely related to the larger forces needed to correct for trajectory errors, either in hovering or tracking. And, for hovering, the work is generally lower, since the body undergoes much smaller displacement. The additional decrease in work for hovering is likely due body inertia affording greater stability for hovering. And, for hovering, that size-dependent stability contributes to a lower tracking error.

At the largest body size, the mechanical properties (the torsional spring stiffness) of the abdominal joint also influence the work and cost (and to some extent tracking error). Interestingly, there are specific combinations of body mass and spring stiffness values that minimize cost of transport, representing the possibility of size-dependent tuning of body mechanical properties.

It is interesting to note, that mass changes occur not only between individuals and species, but also within an individual. One example of mass change within an individual includes the large egg loads have been observed to negatively effect the flight performance of flesh flies (*Neobellieria bullata*) by reducing lift [13]. Our simulations suggest that during this particular morphological state, gravid flesh flies may minimize their tracking error while hovering, while simultaneously increasing the mechanical work (and cost of transport) due to this additional mass in the abdomen. That said, the energetic consequences of trajectory tracking for large egg loaded flesh flies remain unexplored.

Additionally, insects with long, spindle-like abdomens, such as the Odonates and robber flies, may function in a similar capacity to an extended, and shifted center of mass (*i.e.* a petiole length extension). While both the dragonflies and robber flies, both exceptionally effective predators, use visual interception strategies to capture prey in flight (dragonflies: [87, 96, 95]; robber flies: [131]) our models suggest that the long, spindle-like abdomens of both predators may provide an inertial mechanism of aid in their tracking of prey at the expense of a higher mechanical work and cost of transport.

By coincidence, one particular morphology we modeled was similar to that of a mud dauber (*Sceliphron caementarium*, [72]). This morphology is of the lowest length scale factor (LSF = 0.5), paired with the longest petiole length extension (PLE = 0.4) set of

simulations (3rd column in Figures 3.4A and 3.5A). Our model suggests that insects of this particular morphology tasked with vertical flower tracking or hovering may benefit greatly in the three key performance metrics presented in this study simply by virtue of their morphology.

In synthetic systems, trade-offs are frequently analyzed in robotics and engineering, recently with terrestrial robotics [71]. Trade-offs in flight have more traditionally been examined in the negotiations of size, weight, and power (SWaP) in synthetic systems [90].

*Contributions to mechanical work by wings and airframe deformations*

Another interesting pattern that emerged from our simulations, is how the actuation from wings contributes to mechanical work when compared to the actuation from the airframe deformations.

At smaller sizes (LSF = 0.5), we observed that the rectilinear work term associated with wing force actuation is the dominant component of mechanical work (see orange-red bars in Figure 3.6B corresponding to $\vec{F}|\Delta\vec{r}|$). Recall that in all simulations we used the wing beat frequency of the hawkmoth (*Manduca sexta*), 25 Hz. Interestingly, Greenewalt, 1975 [54] demonstrated that as wing length decreases, wing beat frequency increases – where simultaneously, wing length is directly proportional to the mass of the animal. This suggests that a possible reason for increased wing beat frequency in smaller flapping flight organisms is to perform the wing actuation work necessary for flight.

For larger sizes, and both the lowest and intermediate abdominal mass multipliers, the dominant component of mechanical work was the component associated with abdominal actuation. This result is consistent with Dyhr *et. al* [45] which found that abdominal flexions redirect the forces generated by wings and are thus a mechanism for flight control and stability. Our simplified model also stands in contrast to the findings of Hedrick and Daniel [59] as our model finds that the rotational work due to abdominal actuation is greater in most variations to our simulations than the work due to wing torques – except in the case of the largest abdominal mass multiplier simulations.

Lastly, our results show that as size increased (either abdominal masses or length scale

factor), the component of wing torque also increased its fraction of mechanical work. This is consistent with previous literature which indicates that wing torques provide a greater role in flight control as sizes of organism increase.

## *3.6 Conclusion*

This study examined the theoretical trade-offs in negotiating flower tracking accuracy with flight performance energetics (such as mechanical work and cost of transport) for both vertical flower tracking and hovering. We modified an existing forward dynamics model for two-dimensional motions of a model insect with a deformable airframe [21]. In general, we find an inverse relationship between flower tracking accuracy and the cost of transport as masses or sizes increase to perform the given task. We also find a greater role for wing forces for smaller sized simulations, while larger sized simulations generally relied more on airframe deformations to vertically track or hover. This study has theoretically demonstrated the role for abdominal deformations in flower tracking flight for a range of inertial-elastic, and morphological modifications.

## *3.7 Appendix*

*Mechanical properties of the previously described model*

The mechanical properties described in Table 2.2 were previously defined and described in Bustamante *et. al* [21]. These mechanical properties were also defined in the code available on https://github.com/JorgeBJr/multibodyDynamicsModel.gitGitHub. To reiterate, the mechanical properties of the model were defined as follows: $L_1$ is a fixed length between the thorax-abdomen joint to the center of the head-thorax mass (in cm), $L_2$ is a fixed length between the thorax-abdomen joint to the center of the abdomen mass (in cm), and $L_3$ is the fixed length between the thorax-abdomen joint to the center of the aerodynamic lift of the thorax-abdomen joint to the center of aerodynamic lift of the insect located in the head-thorax mass (in cm), (Figure 3.1A). $a_{head}$ is the major axis of the head-thorax ellipsoid mass (in cm). $a_{butt}$ is the major axis of the abdomen ellipsoid mass (in cm). $b_{head}$ is the minor axis of the head-thorax ellipsoid mass (in cm). $b_{butt}$ is the minor axis of the

abdomen ellipsoid mass (in cm). $\kappa$ is the torsional spring constant of the thorax-petiole joint as experimentally measured in [21] (in $cm^2g/(rad*s^2)$). $\eta$ is the torsional damping coefficient of the thorax-petiole joint as reported in [45] (in $cm^2g/s$). $\rho_{head}$ is the density of the head-thorax mass (in $g/cm^3$). $\rho_{butt}$ is the density of the abdomen mass (in $g/cm^3$). $\rho_{air}$ is the density of air (in $g/cm^3$). $\mu_{air}$ is the dynamic viscosity of air at 27°C (in $g/(cm*s)$). And lastly, $g$ is the acceleration due to gravity (in $cm/s^2$).

*Prescribed goal motion frequencies and amplitudes*

The frequencies of the prescribed goal motion are 11 prime number frequencies drawn directly from [107]. The purpose of these prime number frequencies is two-fold: 1) to determine if the output of the system is linear or non-linear, 2) to ensure that any potential harmonics of the system can be distinguished from their basal frequencies (*i.e.* not overlap).

The amplitude(s) of the goal motion signal decrease by a prescribed factor as shown in equation 3.4.

$$A_n = \frac{A_1}{2\pi f_n} 2\pi f_1 \tag{3.4}$$

This amplitude decrease is necessary to ensure that the derivative of the models tracking this goal do not accelerate substantially causing unwanted instabilites in the system.

*Absolute tracking error for all model variations*

The absolute tracking error was the dimensional counterpart of panel A in Figures 3.2 - 3.5 (in cm). For the inertial-elastic modification simulations, this trend was identical as the body length of all simulations was identical (3.7A). For the morphological modification simulations, there were different body lengths depending on length scale factor and petiole length extension (3.7B). This change in body length as petiole length extension increased, amplified the differences in tracking error.

*General Linear Model statistics*

The general linear model statistics were defined in Tables 3.1 and 3.2. All general linear model statistics were performed in R.

*Model dynamics for all model variations*

The model dynamics for all model variations are plotted in this appendix section. Figures 3.8-3.10 are the model dynamics of the inertial-elastic models tracking a vertically oscillating signal. Figures 3.11-3.13 are the model dynamics of the inertial-elastic models hovering. Figures 3.14-3.16 are the model dynamics of the morphological models tracking a vertically oscillating signal. Figures 3.17-3.19 are the model dynamics of the morphological models hovering. In both Figures 3.10 and 3.13, an oscillation was observed for the simulations of the highest abdominal mass multiplier ($10 * m_2$), paired with the lowest torsional spring constant multiplier ($0.1 * \kappa$). Given the nature of dynamics, mass, inertia, and spring constant which connects the two masses, an oscillation is expected to occur though the specific cause of this oscillation is currently not known. Future work will address this issue.

## *3.8 Figures for Chapter 3*

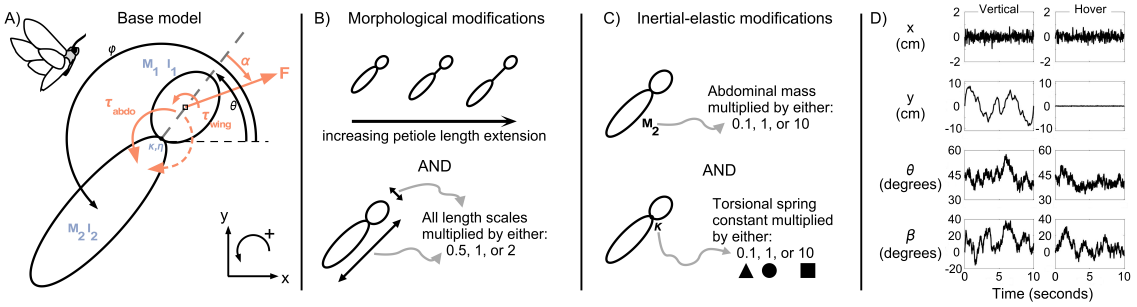


Figure 3.1: **Model basis and modifications.** A) The base model as previously described ([21]) has mechanical properties described in black, and the randomized applied efforts (using Monte Carlo methods) in orange-red. Reference frame describes positive motion coordinates and rotational motions (counterclockwise). B) Morphological modifications to the base model. There were three sets of simulations of petiole length extension where a petiole of prescribed length was inserted between the head-thorax mass ($m_1$) and the abdominal mass ($m_2$). Such prescribed lengths were one of the following three values: 0%, 20%, or 40%. Additionally, there were three sets of simulations of length scale factor multipliers applied to the base model. This length scale factor value was multiplied to all length scales in the base model. The length scale factor simulations were one of the following three values: 0.5, 1, or 2. C) Inertial-elastic modifications to the base model. There were three different abdominal mass multipliers. The abdominal mass multipliers were multiplied only to the abdominal mass and were one of the following three values: 0.1, 1 or 10. There were three different torsional spring constant multipliers. The torsional spring constant multipliers were: 0.1, 1 or 10. D) A sample tracing of the state variables progressing through the full 10 second simulation. The left column is the vertically oscillating signal. The right column is hovering. $x$, and $y$ correspond to the rectilinear motion of the pin joint. $\theta$ is the head motion. $\beta$ is the abdominal flexion (where $\beta = \phi$ - $\theta$ - $\pi$).

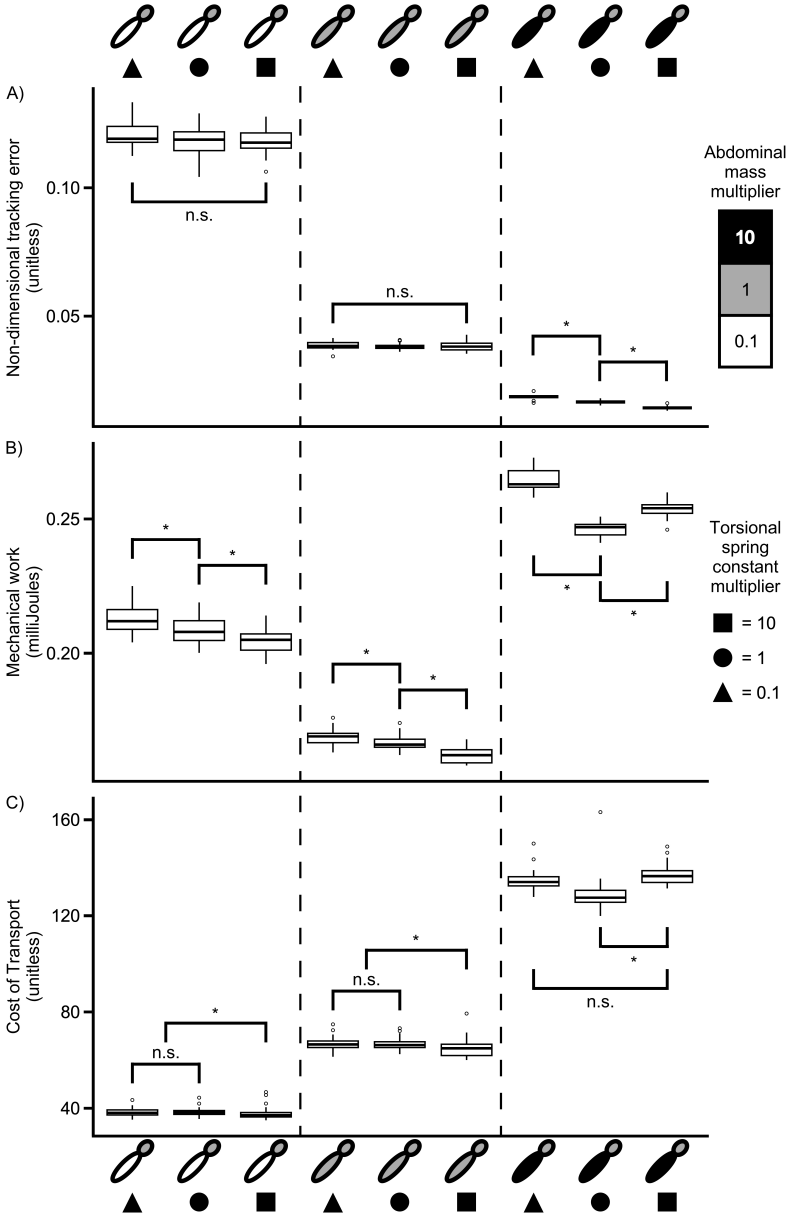


Figure 3.2: **Inertial-elastic modification simulation results for tracking a vertically oscillating signal.** Figure legend indicates the inertial-elastic modifications as such: abdominal mass multiplier increases in a single order of magnitude (*i.e.*, white corresponds to $0.1 * m_2$, grey corresponds to $1 * m_2$, black corresponds to $10 * m_2$); torsional spring constant multiplier also increases by an order of magnitude twice (*i.e.*, circle corresponds to $0.1 * \kappa$, triangle corresponds to $1 * \kappa$, square corresponds to $10 * \kappa$). For all figures, the head mass ($m_1$) does not change in magnitude. All results here are based on 40 full simulations for each inertial-elastic combination. Each full simulation run time was 10 seconds of simulated flight. All statistical groupings are indicated by their respective box plot in lower-case letters. All statistical groupings were based on Bonferroni correction factor (*i.e.*, reject hypothesis if $P > 0.05/2$). Panel A) is the non-dimensional tracking error for tracking a vertically oscillating signal. Panel B) is the mechanical work expended to track a vertically oscillating signal. Panel C) is the cost of transport for tracking a vertically oscillating signal.

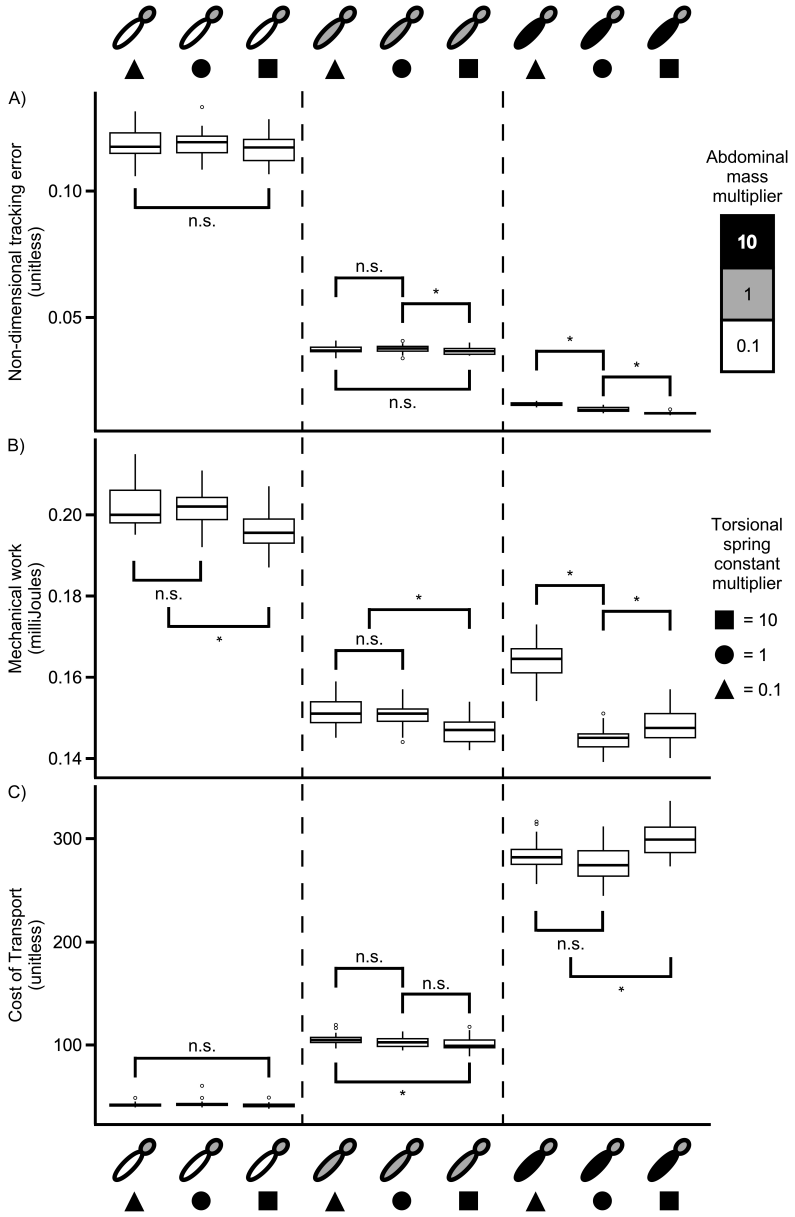


Figure 3.3: **Inertial-elastic modification simulation results for hovering.** Figure legend indicates the inertial-elastic modifications as such: abdominal mass multiplier increases in a single order of magnitude (*i.e.*, white corresponds to $0.1{*}m_2$, grey corresponds to $1{*}m_2$, black corresponds to $10{*}m_2$); torsional spring constant multiplier also increases by an order of magnitude twice (*i.e.*, circle corresponds to $0.1 * \kappa$, triangle corresponds to $1 * \kappa$, square corresponds to $10 * \kappa$). For all figures, the head mass ($m_1$) does not change in magnitude. All results here are based on 40 full simulations for each inertial-elastic combination. Each full simulation run time was 10 seconds of simulated flight. All statistical groupings are indicated by their respective box plot in lower-case letters. All statistical groupings were based on Bonferroni correction factor (*i.e.*, reject hypothesis if $P > 0.05/2$). Panel A) is the non-dimensional tracking error for hovering. Panel B) is the mechanical work expended to hover. Panel C) is the cost of transport for hovering.

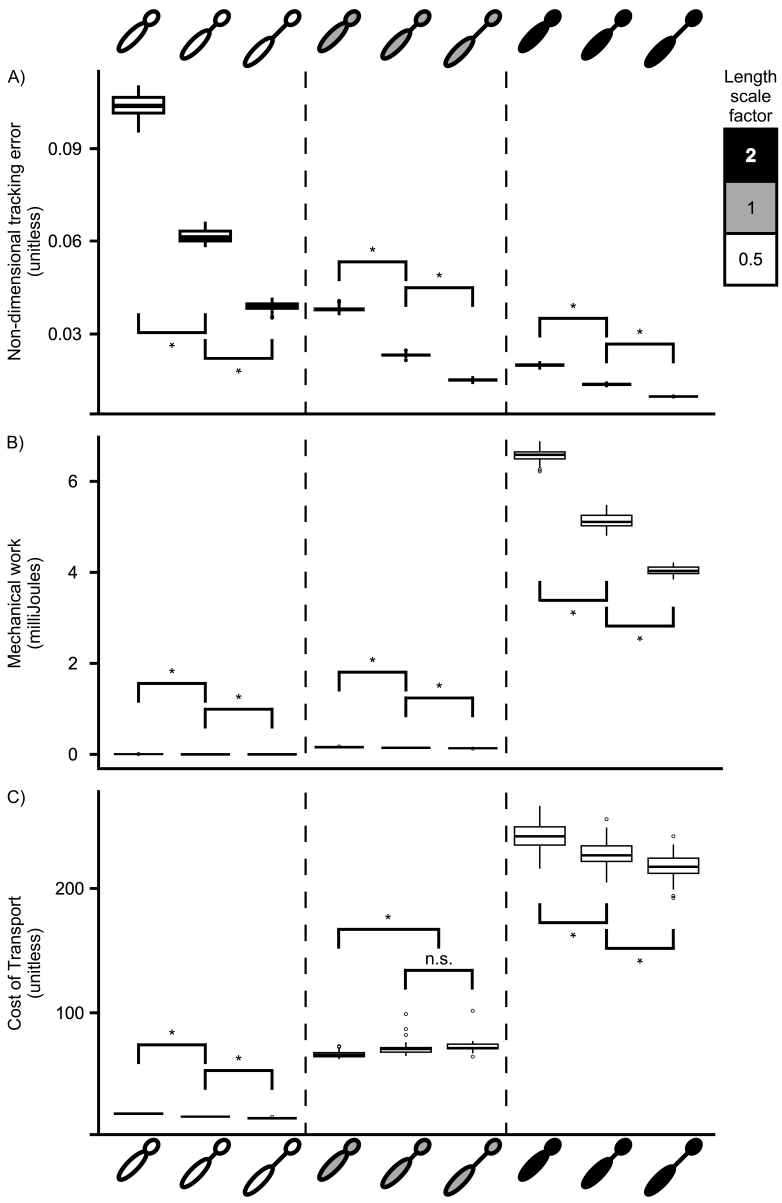


Figure 3.4: **Morphological modification simulation results for tracking a vertically oscillating signal.** Figure legend indicates the morphological modifications as such: length scale factor increases from 0.5 to 2 (*i.e.*, white corresponds to a length scale factor of 0.5, grey corresponds to a length scale factor of 1, black corresponds to a length scale factor of 2); petiole length extension values are: 0%, 20%, and 40% of the total body length, and are visually described. All results here are based on 40 full simulations for each morphological combination. Each full simulation run time was 10 seconds of simulated flight. All statistical groupings are indicated by their respective box plot in lower-case letters. All statistical groupings were based on Bonferroni correction factor (*i.e.*, reject hypothesis if $P > 0.05/2$). Panel A) is the non-dimensional tracking error for tracking a vertically oscillating signal. Panel B) is the mechanical work expended to track a vertically oscillating signal. Panel C) is the cost of transport for tracking a vertically oscillating signal.

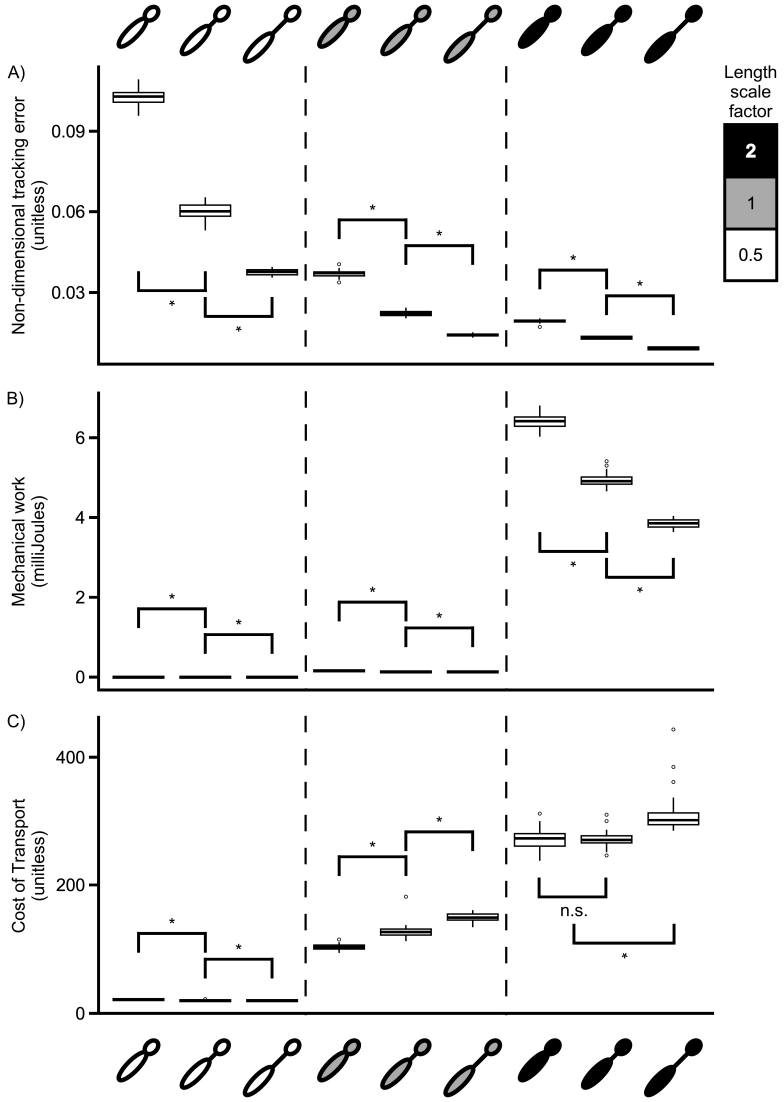


Figure 3.5: **Morphological modification simulation results for hovering.** Figure legend indicates the morphological modifications as such: length scale factor increases from 0.5 to 2 (*i.e.*, white corresponds to a length scale factor of 0.5, grey corresponds to a length scale factor of 1, black corresponds to a length scale factor of 2); petiole length extension values are: 0%, 20%, and 40% of the total body length, and are visually described. All results here are based on 40 full simulations for each morphological combination. Each full simulation run time was 10 seconds of simulated flight. All statistical groupings are indicated by their respective box plot in lower-case letters. All statistical groupings were based on Bonferroni correction factor (*i.e.*, reject hypothesis if $P > 0.05/2$). Panel A) is the non-dimensional tracking error for hovering. Panel B) is the mechanical work expended to hover. Panel C) is the cost of transport for hovering.

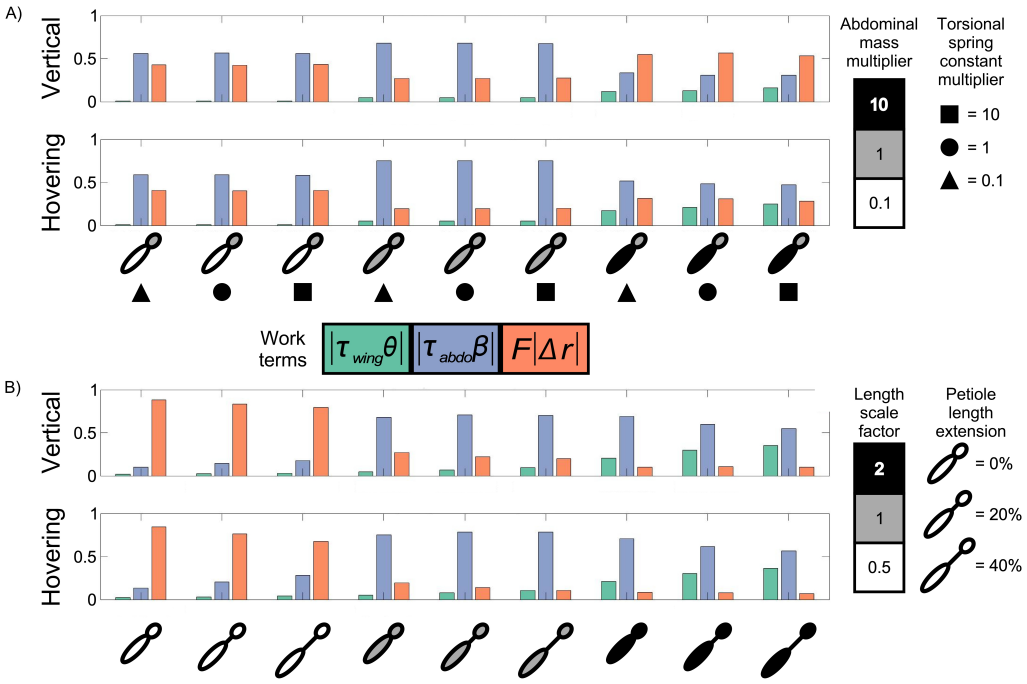


Figure 3.6: **Trade-offs in components of mechanical work.** The figure legend in the center describes the different colors pertaining to the different work terms. There were two rotational work components, and one rectilinear work component. Green is the rotational work component from the product of the wing torque ($\tau_{wing}$) and the head-thorax rotational motion ($\theta$). Blue is the rotational work component from the product of the abdominal torque ($\tau_{abdo}$) and the rotational abdominal flexion motion ($\beta$). Lastly, red is the rectilinear work component from the product of the applied force ($F$) and the distance the simulation traveled in the 20 ms time period ($|\ \Delta\vec{r}\ |$). The figure legends on the right are the same as previous figures.

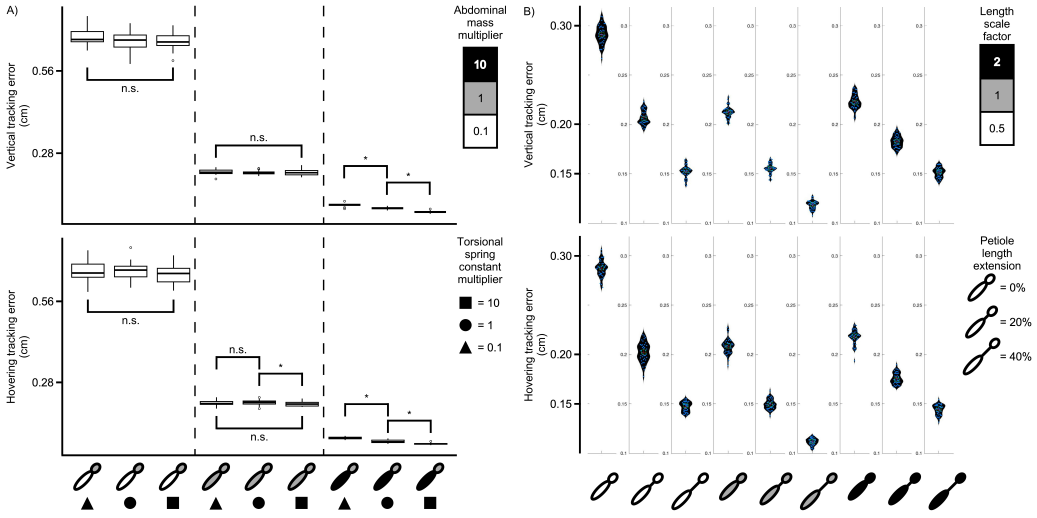


Figure 3.7: **Absolute tracking error for all model variations.** Figure legends are the same as previous figures. All results here are based on 40 full simulations for each morphological combination. Each full simulation run time was 10 seconds of simulated flight. All statistical groupings were based on Bonferroni correction factor (*i.e.*, reject hypothesis if $P > 0.05/2$). Panel A) is the tracking error for the inertial-elastic modification simulations (in cm). Panel B) is the tracking error for the morphological modification simulations (in cm).

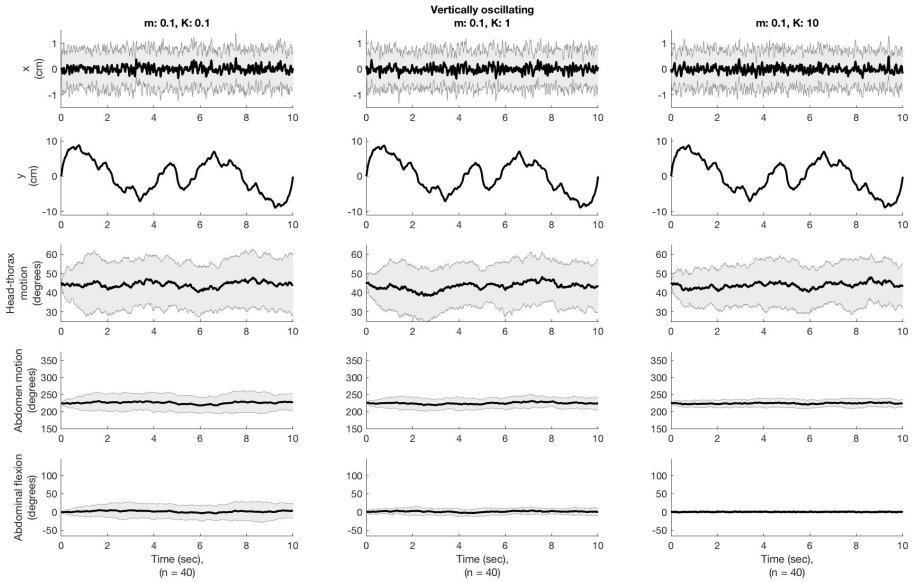


Figure 3.8: **Model dynamics output for the lowest abdominal mass multiplier ($0.1 * m_2$) tracking a vertically oscillating signal**. Torsional spring constants increase from left to right (0.1, 1, 10 respectively). All plots are with respect to time for a 10 second simulation period. All plots display the mean +/- standard deviation ($n = 40$). Top row is the x-motion in cm. Second row is the y-motion in cm. The third row is the head-thorax ($m_1$) mass motion in degrees. The fourth row is the abdominal motion ($m_2$) in degrees. The bottom row is the abdominal flexion angle (i.e. difference between rows 4 and 3 respectively) in degrees. For all simulations, the model tracks the input y-motion well.

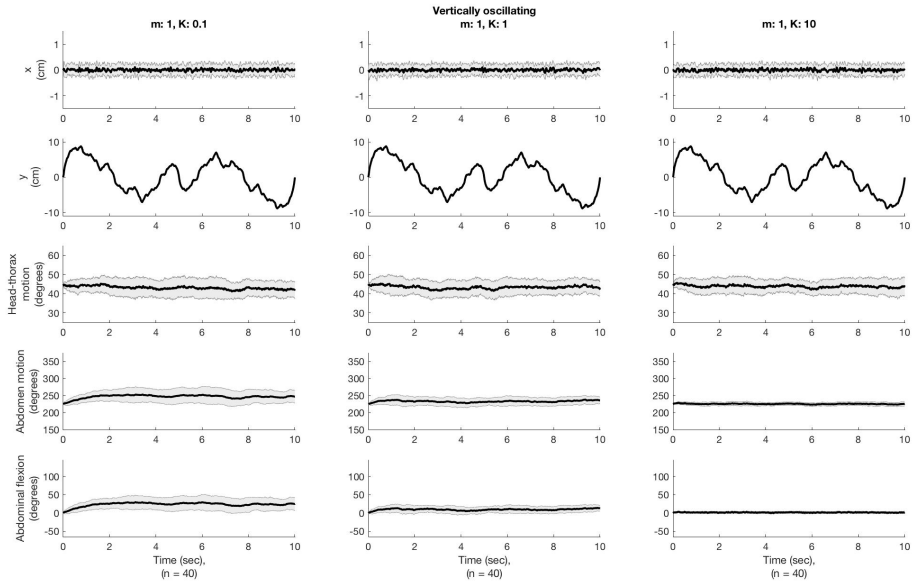


Figure 3.9: **Model dynamics output for the intermediate abdominal mass multiplier ($1 * m_2$) tracking a vertically oscillating signal**. Torsional spring constants increase from left to right (0.1, 1, 10 respectively). All plots are with respect to time for a 10 second simulation period. All plots display the mean +/- standard deviation ($n = 40$). Top row is the x-motion in cm. Second row is the y-motion in cm. The third row is the head-thorax ($m_1$) mass motion in degrees. The fourth row is the abdominal motion ($m_2$) in degrees. The bottom row is the abdominal flexion angle (i.e. difference between rows 4 and 3 respectively) in degrees. For all simulations, the model tracks the input y-motion well.

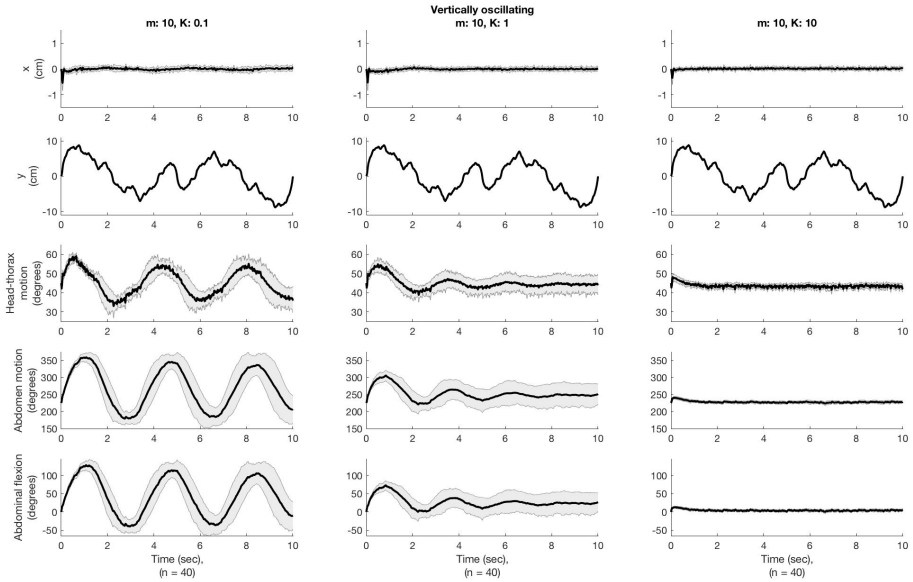


Figure 3.10: **Model dynamics output for the highest abdominal mass multiplier ($10 * m_2$) tracking a vertically oscillating signal**. Torsional spring constants increase from left to right (0.1, 1, 10 respectively). All plots are with respect to time for a 10 second simulation period. All plots display the mean +/- standard deviation ($n = 40$). Top row is the x-motion in cm. Second row is the y-motion in cm. The third row is the head-thorax ($m_1$) mass motion in degrees. The fourth row is the abdominal motion ($m_2$) in degrees. The bottom row is the abdominal flexion angle (i.e. difference between rows 4 and 3 respectively) in degrees. For all simulations, the model tracks the input y-motion well.

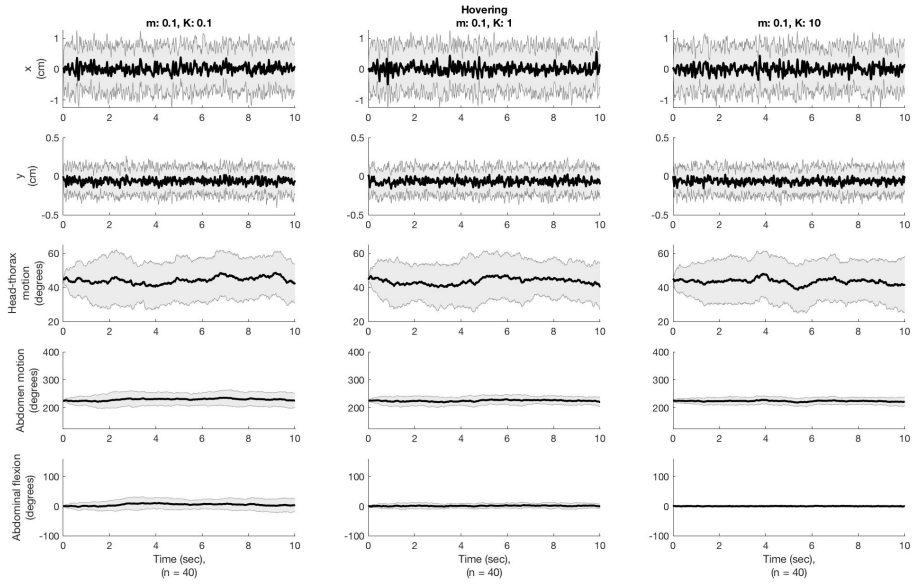


Figure 3.11: **Model dynamics output for the lowest abdominal mass multiplier ($0.1 * m_2$) for hovering**. Torsional spring constants increase from left to right (0.1, 1, 10 respectively). All plots are with respect to time for a 10 second simulation period. All plots display the mean +/- standard deviation ($n = 40$). Top row is the x-motion in cm. Second row is the y-motion in cm. The third row is the head-thorax ($m_1$) mass motion in degrees. The fourth row is the abdominal motion ($m_2$) in degrees. The bottom row is the abdominal flexion angle (i.e. difference between rows 4 and 3 respectively) in degrees. For all simulations, the model tracks the input y-motion well.

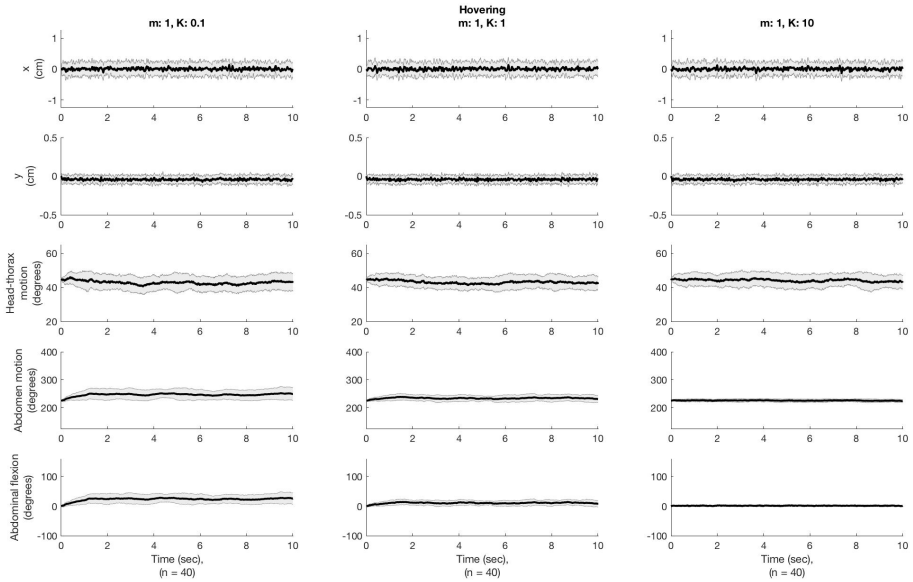


Figure 3.12: **Model dynamics output for the intermediate abdominal mass multiplier ($1 * m_2$) for hovering**. Torsional spring constants increase from left to right (0.1, 1, 10 respectively). All plots are with respect to time for a 10 second simulation period. All plots display the mean +/- standard deviation ($n = 40$). Top row is the x-motion in cm. Second row is the y-motion in cm. The third row is the head-thorax ($m_1$) mass motion in degrees. The fourth row is the abdominal motion ($m_2$) in degrees. The bottom row is the abdominal flexion angle (i.e. difference between rows 4 and 3 respectively) in degrees. For all simulations, the model tracks the input y-motion well.

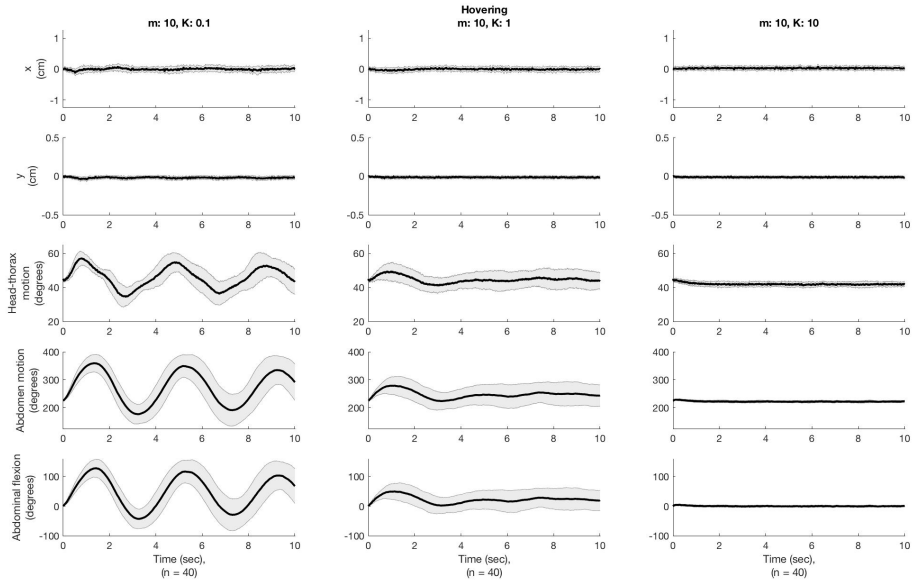


Figure 3.13: **Model dynamics output for the highest abdominal mass multiplier ($10 * m_2$) for hovering**. Torsional spring constants increase from left to right (0.1, 1, 10 respectively). All plots are with respect to time for a 10 second simulation period. All plots display the mean +/- standard deviation ($n = 40$). Top row is the x-motion in cm. Second row is the y-motion in cm. The third row is the head-thorax ($m_1$) mass motion in degrees. The fourth row is the abdominal motion ($m_2$) in degrees. The bottom row is the abdominal flexion angle (i.e. difference between rows 4 and 3 respectively) in degrees. For all simulations, the model tracks the input y-motion well.

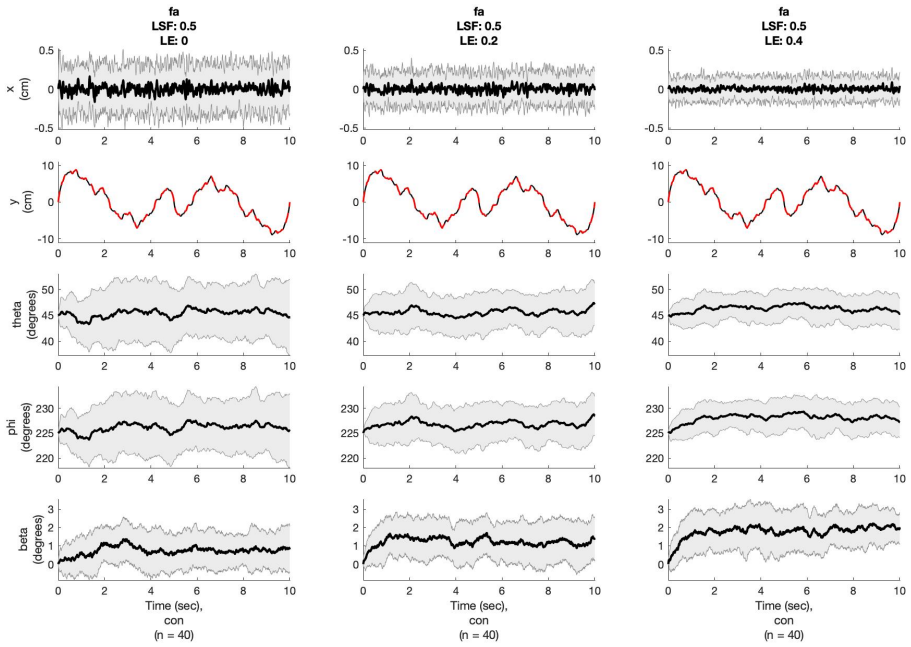


Figure 3.14: **Model dynamics output for the lowest length scale factor multiplier (LSF = 0.5) tracking a vertically oscillating signal**. Petiole length extension increases from left to right (0, 0.2, 0.4 respectively). All plots are with respect to time for a 10 second simulation period. All plots display the mean +/- standard deviation ($n = 40$). Top row is the x-motion in cm. Second row is the y-motion in cm. The third row is the head-thorax ($m_1$) mass motion in degrees. The fourth row is the abdominal motion ($m_2$) in degrees. The bottom row is the abdominal flexion angle (i.e. difference between rows 4 and 3 respectively) in degrees. For all simulations, the model tracks the input y-motion well.

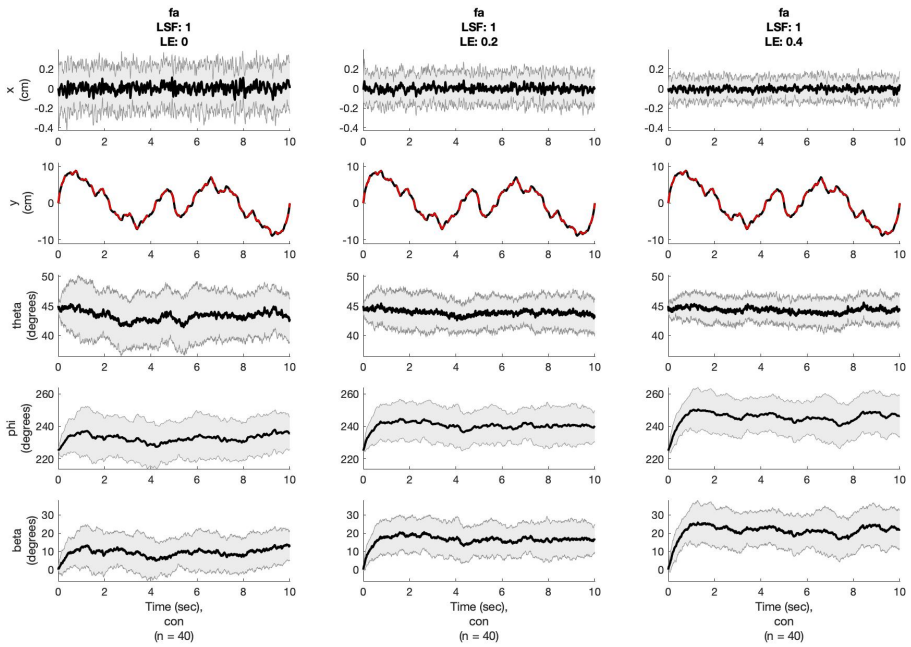


Figure 3.15: **Model dynamics output for the intermediate length scale factor multiplier (LSF = 1) tracking a vertically oscillating signal**. Petiole length extension increases from left to right (0, 0.2, 0.4 respectively). All plots are with respect to time for a 10 second simulation period. All plots display the mean +/- standard deviation ($n = 40$). Top row is the x-motion in cm. Second row is the y-motion in cm. The third row is the head-thorax ($m_1$) mass motion in degrees. The fourth row is the abdominal motion ($m_2$) in degrees. The bottom row is the abdominal flexion angle (i.e. difference between rows 4 and 3 respectively) in degrees. For all simulations, the model tracks the input y-motion well.

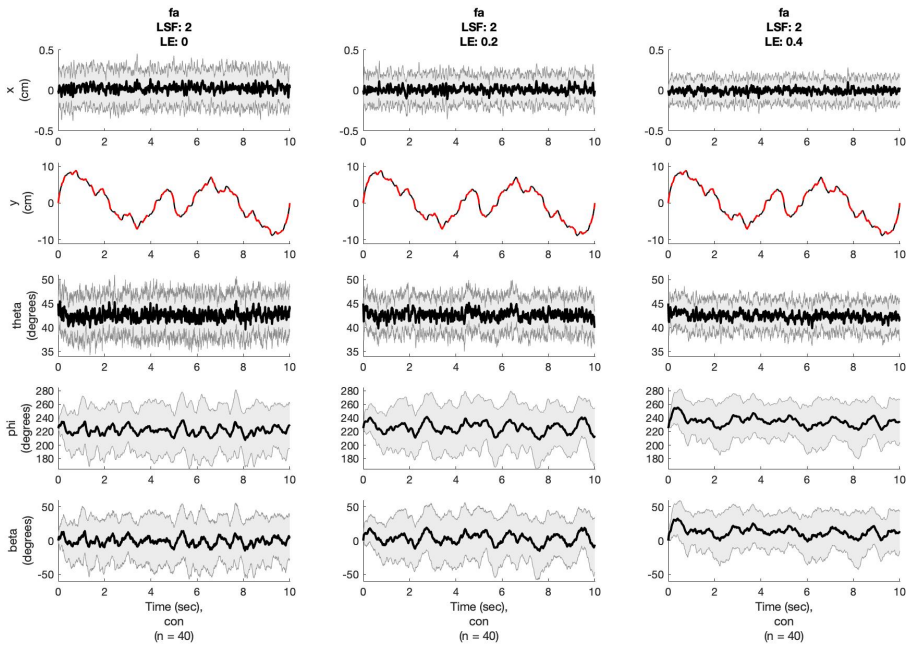


Figure 3.16: **Model dynamics output for the highest length scale factor multiplier (LSF = 2) tracking a vertically oscillating signal**. Petiole length extension increases from left to right (0, 0.2, 0.4 respectively). All plots are with respect to time for a 10 second simulation period. All plots display the mean +/- standard deviation ($n = 40$). Top row is the x-motion in cm. Second row is the y-motion in cm. The third row is the head-thorax ($m_1$) mass motion in degrees. The fourth row is the abdominal motion ($m_2$) in degrees. The bottom row is the abdominal flexion angle (i.e. difference between rows 4 and 3 respectively) in degrees. For all simulations, the model tracks the input y-motion well.

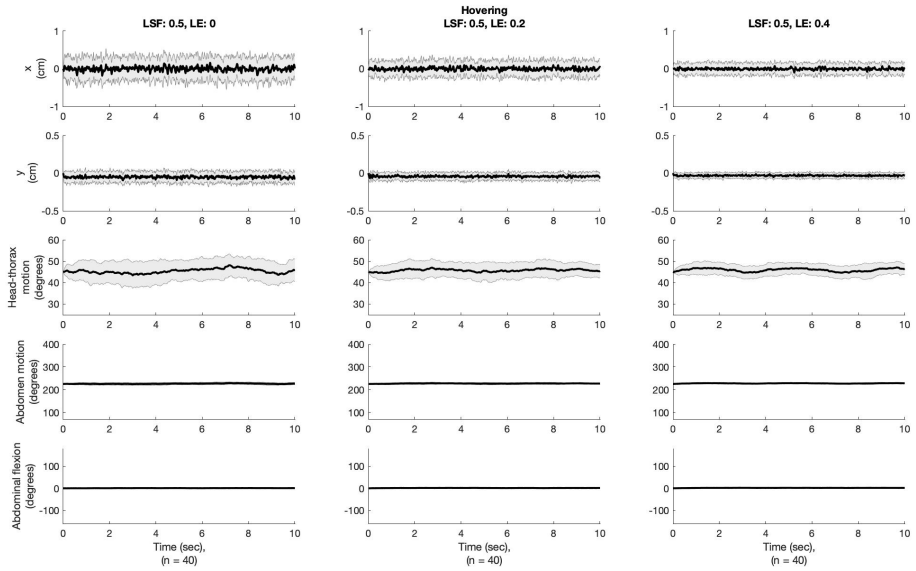


Figure 3.17: **Model dynamics output for the lowest length scale factor multiplier (LSF = 0.5) for hovering**. Petiole length extension increases from left to right (0, 0.2, 0.4 respectively). All plots are with respect to time for a 10 second simulation period. All plots display the mean +/- standard deviation ($n = 40$). Top row is the x-motion in cm. Second row is the y-motion in cm. The third row is the head-thorax ($m_1$) mass motion in degrees. The fourth row is the abdominal motion ($m_2$) in degrees. The bottom row is the abdominal flexion angle (i.e. difference between rows 4 and 3 respectively) in degrees. For all simulations, the model tracks the input y-motion well.

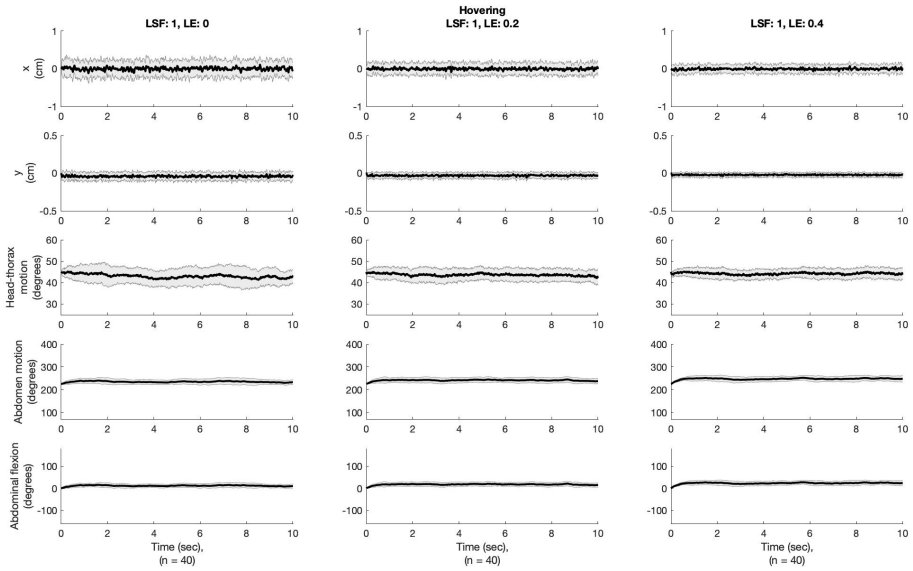


Figure 3.18: **Model dynamics output for the intermediate length scale factor multiplier (LSF = 1) for hovering**. Petiole length extension increases from left to right (0, 0.2, 0.4 respectively). All plots are with respect to time for a 10 second simulation period. All plots display the mean +/- standard deviation ($n = 40$). Top row is the x-motion in cm. Second row is the y-motion in cm. The third row is the head-thorax ($m_1$) mass motion in degrees. The fourth row is the abdominal motion ($m_2$) in degrees. The bottom row is the abdominal flexion angle (i.e. difference between rows 4 and 3 respectively) in degrees. For all simulations, the model tracks the input y-motion well.

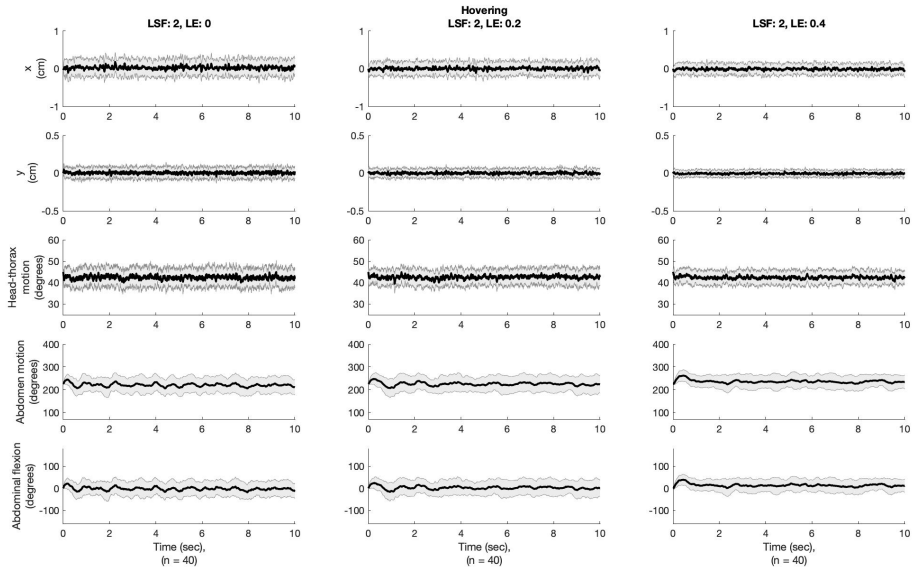


Figure 3.19: **Model dynamics output for the highest length scale factor multiplier (LSF = 2) for hovering**. Petiole length extension increases from left to right (0, 0.2, 0.4 respectively). All plots are with respect to time for a 10 second simulation period. All plots display the mean +/- standard deviation ($n = 40$). Top row is the x-motion in cm. Second row is the y-motion in cm. The third row is the head-thorax ($m_1$) mass motion in degrees. The fourth row is the abdominal motion ($m_2$) in degrees. The bottom row is the abdominal flexion angle (i.e. difference between rows 4 and 3 respectively) in degrees. For all simulations, the model tracks the input y-motion well.

### *3.9 Tables for Chapter 3*

### *3.10 Acknowledgments for Chapter 3*

We thank Alison Weber and Berry Brosi for their guidance in which statistical analyses to use. This work was supported by AFOSR grants FA9550-14-1-0398 and FA9550-19-1-0386 to TLD, an NSF Graduate Research Fellowship to JB, an Human Frontier Science Program Long-term Postdoctoral Fellowship to TD.

| Vertical flower tracking motion<br>Non-dimensional tracking error<br>($R^2 = 0.658$) | | |
|---|---|---|
| Regressors | P | coefficients |
| Intercept | 2.824747e-159 | 0.1363 |
| Abdominal mass multiplier | 5.922190e-69 | -0.0068 |
| Torsional spring constant | 5.822850e-1 | 0.0002 |
| Abdominal mass multiplier:<br>Torsional spring constant | 3.990169e-1 | -5.16e-5 |
| Length scale factor | 3.940395e-58 | -0.0547 |
| Petiole length extension | 6.542726e-50 | -0.2395 |
| Length scale factor:<br>Petiole length extension | 4.020455e-16 | 0.1002 |
| Mechanical work<br>($R^2 = 0.880$) | | |
| Regressors | P | coefficients |
| Intercept | 4.095407e-157 | -3.9803 |
| Abdominal mass multiplier | 1.602505e-8 | -0.0580 |
| Torsional spring constant | 2.225490e-10 | -0.0653 |
| Abdominal mass multiplier:<br>Torsional spring constant | 1.233514e-3 | 0.0059 |
| Length scale factor | 1.159264e-245 | 4.8850 |
| Petiole length extension | 4.862947e-37 | 5.9160 |
| Length scale factor:<br>Petiole length extension | 1.288715e-43 | -5.2854 |
| Cost of transport<br>($R^2 = 0.962$) | | |
| Regressors | P | coefficients |
| Intercept | 9.168632e-192 | -97.3372 |
| Abdominal mass multiplier | 9.259754e-152 | 7.2360 |
| Torsional spring constant | 3.749781e-11 | -1.4045 |
| Abdominal mass multiplier:<br>Torsional spring constant | 1.081050e-6 | 0.1831 |

| Hovering<br>Non-dimensional tracking error<br>($R^2 = 0.493$) | | |
|---|---|---|
| Regressors | P | coefficients |
| Intercept | 8.805088e-77 | 0.4577 |
| Abdominal mass multiplier | 2.665695e-50 | -0.0322 |
| Torsional spring constant | 1.053008e-4 | 0.0078 |
| Abdominal mass multiplier:<br>Torsional spring constant | 1.852378e-2 | -0.0008 |
| Length scale factor | 7.666801e-6 | -0.0814 |
| Petiole length extension | 2.228747e-21 | -0.8460 |
| Length scale factor:<br>Petiole length extension | 7.814085e-4 | 0.2380 |
| Mechanical work<br>($R^2 = 0.866$) | | |
| Regressors | P | coefficients |
| Intercept | 4.630745e-168 | -4.1330 |
| Abdominal mass multiplier | 1.196009e-9 | -0.0631 |
| Torsional spring constant | 1.197474e-9 | -0.0631 |
| Abdominal mass multiplier:<br>Torsional spring constant | 2.083802e-3 | 0.0057 |
| Length scale factor | 2.079187e-245 | 4.8336 |
| Petiole length extension | 2.189303e-44 | 6.6415 |
| Length scale factor:<br>Petiole length extension | 9.040791e-46 | -5.5298 |
| Cost of transport<br>($R^2 = 0.967$) | | |
| Regressors | P | coefficients |
| Intercept | 4.022451e-138 | -97.9502 |
| Abdominal mass multiplier | 0 | 21.0860 |
| Torsional spring constant | 2.070096e-5 | -1.2149 |
| Abdominal mass multiplier:<br>Torsional spring constant | 1.792286e-10 | 0.3297 |

Chapter 4

# PRUNING DEEP NEURAL NETWORKS GENERATES A SPARSE, BIO-INSPIRED NONLINEAR CONTROLLER FOR INSECT FLIGHT

Olivia Zahn [1,∗], Jorge Bustamante, Jr. [2,∗], Callin Switzer [2], Thomas L. Daniel [2] and J. Nathan Kutz [3]

**[1]** Department of Physics, University of Washington, Seattle, WA USA

**[2]** Department of Biology, University of Washington, Seattle, WA USA

**[3]** Department of Applied Mathematics, University of Washington, Seattle, WA USA

**[*]** Primary author(s)

***Abstract***

Insect flight is a strongly nonlinear and actuated dynamical system. As such, strategies for understanding its control have typically relied on either model-based methods or linearizations thereof. Here we develop a framework that combines model predictive control on an established flight dynamics model and *deep neural networks* (DNN) to create an efficient method for solving the inverse problem of flight control. We turn to natural systems for inspiration since they inherently demonstrate network pruning with the consequence of yielding more efficient networks for a specific set of tasks. This bio-inspired approach allows us to leverage network pruning to optimally sparsify a DNN architecture in order to perform flight tasks with as few neural connections as possible. But there are limits to sparsification. Specifically, as number of neurons are below a critical threshold, flight performance drops considerably. We develop sparsification paradigms and explore their limits for control tasks. Monte Carlo simulations also quantify the statistical distribution of network weights during pruning given initial random weights of the DNNs. We demonstrate that on average, the network can be pruned to approximately 7% of the original networks weights, with statistical distributions quantified at each layer of the network. Overall, this work shows that sparsely connected DNN is capable of predicting the forces required to follow complex

trajectories. Additionally, sparsification has sharp performance limits.

### *Introduction*

Between childhood and adolescence, the number of synaptic connections between neurons sharply decreases through a process called synaptic pruning [26]. Depending on the neural system, synaptic pruning can improve the brain's efficiency and affect cognitive function. In fact, synaptic pruning is seen as a mechanism for learning, in which the environment affects which neural connections are maintained and which are removed [33]. Refinement of neural connections via pruning occurs in wide ranging taxa, from humans to *Drosophila* and in systems ranging from sensory input to motor control [70, 129]. For example, during metamorphosis of the hawkmoth, *Manduca Sexta*, synapses are pruned and reconnected to enable adult-specific behaviors [1]. Synaptic pruning plays a significant role in task-specific behavioral development across many different taxa, the result of which is a more sparsely connected network that can still perform complex cognitive and motor tasks.

Deep neural networks (DNNs) are capable of modeling high-dimensional, complex, non-linear mappings for a large diversity of problems, ranging from image and speech recognition to fluid flow control [15, 78, 84]. DNNs learn these mappings by combining gradient descent with the backpropagation algorithm. However, most DNNs are highly over-parameterized and their layers are fully-connected. For example, the natural language processing model, GPT-3, is the largest DNN ever built with 175 billion parameters [19] and successful models with millions of parameters are not uncommon. There are many different methods to make DNNs more sparse, ranging from regularization during training [111] to specifying sparse architectures [88]. Biologically inspired neural network pruning has also been shown to be an effective method for sparsifying a DNN without compromising performance [58, 75, 79, 82, 83]. In neural network pruning, the connectivity of a DNN is made more sparse by forcing select weights between the layers to zero and then retraining, resulting in a more sparse network that is capable of performing comparably to the fully-connected network up to a certain limit. Pruning has been used to prevent network overfitting and to reduce overall model size. In fact, dropout regularization is a form of random pruning, where weights are made zero during training to prevent overfitting [119]. Pruned DNNs have the

advantage of being computationally less expensive than their fully-connected counterparts. They are also more representative of biological neural systems, in which neural pathways are sparsely and specifically connected for task performance.

The inverse problem of insect flight is a highly non-linear dynamical system, in part due to the unsteady mechanisms of flapping flight [40, 108]. As such, the inverse problem of insect flight serves as an exemplar to study whether a DNN can solve a biological control problem while mandating a sparse connectivity pattern. In an inverse problem, the initial and final conditions of a dynamical system are known and used to find the parameters necessary to control the system. In other words, the DNN in this study is trained to predict the controls required to move the simulated insect from one state space to another. Solving the inverse problem of insect flight has been previously simulated using a genetic algorithm wedded with a simplex optimizer for hawkmoth level forward flight and hovering [59]. Another study linearized the dynamical system of simulated hawkmoth flight finding the system to operate on the edge of stability [45]. Recently, a study developed an inertial dynamics model of *M. sexta* flight as it tracked a vertically oscillating signal, which modeled the control inputs using Monte Carlo methods in a model-inspired by model predictive control (MPC) [21].

In this work, we use the inertial dynamics model in [21] to simulate examples of *M. sexta* hovering flight. Fig. 4.1 shows the physical parameters of the simulated moth and the inertial dynamics model. These data are used to train a DNN to learn the controllers for hovering. Drawing inspiration from pruning in biological neural systems, we sparsify the network using neural network pruning. Here, we prune weights based simply on their magnitudes, i.e. remove the weights closest to zero. This bio-inspired approach to sparsity allows us to find the optimally sparse network for completing flight tasks. We employed two methods for neural network pruning: either through manually setting weights to zero or by utilizing binary masking layers. Furthermore, the DNN is pruned sequentially, meaning groups of weights are removed slowly from the network, with retraining in between prunes, until a target sparsity is reached. Monte Carlo simulations are also used to quantify the statistical distribution of network weights during pruning given random initialization of network weights. This work shows that sparse DNNs are capable of predicting the controls

required for a simulated hawkmoth to move from one state-space to another.

## *Materials and methods*

### *Moth model*

The simulated insect uses an inertial dynamics model developed in Bustamante et al., 2021 [21] and was modeled after the hawkmoth, *M. sexta* with body proportions rounded to the nearest 0.1 cm. The simulated moth was made up of two ellipsoid body segments, the head-thorax mass ($m_1$) and the abdomen mass ($m_2$). The body segments are connected by a pin joint consisting of a torsional spring and a torsional damper as seen in [7]. The simulated moth model could move in two linear dimensions ($x$,$y$), both the head-thorax mass, and the abdominal mass could rotate clockwise or counter-clockwise ($\theta$,$\phi$). See Fig. 4.1 and Table 2.2 for more description of the simulated insect.

The computational model of the moth had three control variables and four state-space variables (as well as the respective state-space derivatives). This model is by definition underactuated because the number of control variables is less than the degrees of freedom. The controls are as follows: $F$, the magnitude of force applied; $\alpha$ the direction of force applied (with respect to the midline of the head-thorax mass); and $\tau$, the abdominal torque exerted about the pin joint connecting the two body segment masses (with its equal and opposite response torque). The controls are randomized every 20 ms, which is approximately the period of the wing downstroke or upstroke for *M. sexta* (25 Hz wing beat frequency).

The motion of the moth state-space is described by four parameters ($x$: horizontal position, $y$: vertical position, $\theta$: head-thorax angle, and $\phi$: abdomen angle), as well as the respective state-space derivatives ($\dot{x}$: horizontal velocity, $\dot{y}$: vertical velocity, $\dot{\theta}$: head-thorax angular velocity, and $\dot{\phi}$: abdomen angular velocity). The x and y position are indicate the position of the pin joint where the head-thorax connects with the abdomen.

### *Generating training data*

We used the ordinary differential equations from [21] (See 2.7, Equations 30-33) to generate a dataset for training the deep neural network. We started all simulated trajectories from

the origin (*i.e.*, ($x_0$,$y_0$) = (0,0)). We randomly sampled initial horizontal velocity ($\dot{x}_0$), vertical velocity ($\dot{y}_0$), head-thorax angle ($\theta_0$), abdomen angle ($\phi_0$), head-thorax angular velocity ($\dot{\theta}_0$), and abdomen angular velocity ($\dot{\phi}_0$). We also randomly sampled force ($F$), force angle ($\alpha$), and torque ($\tau$). We created a training data set of 10 million simulated trajectories and a test set containing an additional 5 million trajectories. The trajectories were simulated using the Python (Python Software Foundation, https://www.python.org/) function, `scipy.integrate.odeint` [127]. Fig. 4.1 shows which variables were inputs and outputs from the differential equation solver.

*Data preparation for deep neural network training*

The force ($F$) and force angle ($\alpha$) were converted to horizontal and vertical components ($F_x$ and $F_y$), using the following equations: $F_x = F \cdot cos(\alpha)$ and $F_y = F \cdot sin(\alpha)$. The data were split into training and validation sets for cross validation (80:20 split). The validation data is a sample used to provide an unbiased evaluation of a model fit while tuning the hyper parameters (such as number of hidden units, number of layers, optimizer, *etc.*). The data were scaled using a min-max scaler according to the training data set and transformed values to be between -0.5 and +0.5. The same scaler was then used to transform the validation and test data. See Fig. 4.1 for a diagram comparing the data generation process vs. the training of the neural network.

*Training and pruning a deep neural network*

The deep, fully-connected neural network was constructed with ten input variables and seven output variables (see Fig. 4.1). The initial and final state space conditions are the inputs to the network: ($\dot{x}_i$, $\dot{y}_i$, $\phi_i$, $\theta_i$, $\dot{\phi}_i$, $\dot{\theta}_i$, $x_f$, $y_f$, $\phi_f$, $\theta_f$). The network predicts the control variables and the final derivatives of the state space in its output layer ($F_x$, $F_y$, $\tau$, $\dot{x}_f$, $\dot{y}_f$, $\dot{\theta}_f$, $\dot{\phi}_f$). The final derivatives of the state space were made outputs for the neural network to be able to chain 20 ms allow the moth to complete a complex trajectory. The training and pruning protocols were developed using Keras [27] with the TensorFlow backend [2]. To scale up training for the statistical analysis described in a later section, the training and pruning

protocols were parallelized using the Jax framework [18].

To demonstrate the effects of neural network pruning, the network was chosen to have a deep, feed-forward architecture with wide hidden layers (many more nodes than in the input and output layer). The network had four hidden layers with 400, 400, 400, and 16 nodes, respectively. Wide hidden layers were used rather than using a bottleneck structure (narrower hidden layer width) to allow the network to find the optimal mapping with little constraint. The inverse tangent activation function was used for all hidden layers to introduce non-linearity in the model. To account for the multiple outputs, the loss function was the uniformly-weighted average of the mean squared error for all the outputs combined. There are several hyper-parameter differences in the TensorFlow model and the Jax model in order to optimize performance. In developing the training and pruning protocol in TensorFlow, the network was trained using the rmsprop optimizer with a batch size of $2^{12}$ samples. However, for scaling up and speeding up training using the Jax framework, the Adam optimizer [73] was used and the batch size was reduced to 128 samples. Regularization techniques such as weight regularization, batch normalization, or dropout were not used. However, early stopping (with a minimum delta of 0.000001 with a patience of 150 epochs) was used to reduce overfitting by monitoring the mean squared error on the validation data.

After the fully-connected network is trained to a minimum error, the method of neural network pruning was used to promote sparsity between the network layers. Other regularization techniques (such as lasso) promote sparsity during training. In contrast, pruning achieves sparse connections between layers by setting weights below a specified threshold to zero. In this work, a target sparsity (percentage of pruned network weights) is specified and those weights are forced to zero. The network is then retrained until a minimum error is reached. This process is repeated until most of the weights have been pruned from the network.

Two methods to prune the neural network were developed: 1) a manual method that involves setting a number of weights to zero after each training epoch and 2) pruning using TensorFlow's Model Optimization Toolkit which involves creating a masking layer to control sparsity in the network. Both methods are described in detail in the following sections.

*Manual Pruning*

Our algorithm describes the a method of pruning in which the $n$ weights whose magnitudes are closest to zero are manually set to zero. If $N$ is the total number of weights in the network, the $n$ weights are chosen such that $n/N$ is equivalent to a specified pruning percentage (e.g. 15%, 25%, ..., 98%). After the $n$ weights are set to zero, the network is retrained for one epoch. This process is repeated until the loss is minimized. After the network has been trained to a minimum loss, we select the next pruning percentage from the predetermined list and repeat the above steps. The entire process is repeated until the network has been pruned to the final pruning percentage in the list.

Upon retraining, the weights are able to regain a non-zero weight and the network is evaluated using these non-zero weights. Although this likely still captures the effects of pruning the network over the training time, it is not true pruning in the sense that connections that have been pruned can regain weight.

*Pruning using Model Optimization Toolkit*

The manual pruning method described above has the downside of allowing weights to regain non-zero value after training. These weights are subsequently set back to zero on the next epoch, but the algorithm does not guarantee that the same weights will be pruned every time.

To ensure weights remain pruned during retraining, a TensorFlow built toolkit called the Model Optimization Toolkit was implemented in the pruning protocol. The toolkit contains functions for pruning deep neural networks. In the Model Optimization Toolkit, pruning is achieved through the use of binary masking layers that are multiplied element-wise to each weight matrix in the network. A four-layer neural network can be mathematically described the following way.

$$\hat{y} = \sigma_4(\mathbf{A_4}...(\sigma_1(\mathbf{A_1}x)) \tag{4.1}$$

In Eq. 4.1, the inputs to the network are represented by $x$, the predictions by $\hat{y}$, the weight matrices by $\mathbf{A_i}$, and the activation function by $\sigma_i$, where $i = 1, 2, 3, 4$ for the four

layers of the network. During pruning, the binary masking matrix, $\mathbf{M_i}$ is placed between each layer.

$$\hat{y} = \mathbf{M_4} \circ \sigma_4(\mathbf{A_4}...(\mathbf{M_1} \circ (\sigma_1(\mathbf{A_1}x))) \tag{4.2}$$

In Eq. 4.2, the binary masking matrices, $\mathbf{M_i}$, are multiplied element-wise to the weight matrices ($\circ$ denotes the element-wise Hadamard product). The sparsity of each layer is controlled by a separate masking matrices to allow for different levels of sparsity in each layer. Before pruning, all elements of $\mathbf{M_i}$ are set to 1. At each pruning percentage (e.g. 15%, 25%, ..., 98%), the $n$ weights whose magnitudes are nearest to zero are found and the corresponding elements of the the $\mathbf{M_i}$ are set to zero. The network is then retrained until a minimum error is achieved. The masking layers are non-trainable, meaning they will not be updated during backpropagation. Then, the next pruning percentage is selected and the process is repeated until the network has been pruned to the final pruning percentage.

In the Model Optimization Toolkit, the binary masking layer is added by wrapping each layer into a prunable layer. The binary masking layer controls the sparsity of the layer by setting terms in the matrix equal to either zero or one. The masking layer is bi-directional, meaning it masks the weights in both the forward pass and backpropagation step, ensuring no pruned weights are updated [144]. A separate algorithm describes the pruning paradigm utilizing the Model Optimization Toolkit.

Rather than controlling for sparsity at each epoch of training, as done in the manual pruning method described above, we control for sparsity each time we want to prune more weights from the network. Sparsity is kept constant throughout each pruning cycle and therefore we can use TensorFlow's built-in functions for training the network and regularization.

*Preparing for statistical analysis of pruned networks*

To be able to train and analyze many neural networks, the training and pruning protocols were parallelized in the Jax framework [18]. Rather than requiring data to be in the form of tensors (such as in TensorFlow), Jax is capable of performing transformations on NumPy

[56] structures. Jax however does not come with a toolkit for pruning, therefore pruning by way of the binary masking matrices was coded into the training loop.

The networks were trained and pruned using a NVIDIA Titan Xp GPU operating with CUDA [93]. At most, 400 networks were trained at the same time and the total number of networks used in the analysis was 1306. These networks were all trained with identical architectures, pruning percentages, and hyper-parameters. The only difference between the networks is the random initialization of the weights before training and pruning. The Adam optimizer [73] and a batch size of 128 were used to speed up training and cross-validation was omitted. However, early stopping was used on the training data to avoid training beyond when the loss was adequately minimized. Additionally, early stopping was used to evaluate the decrease in loss across batches, rather than epochs.

### *Results*

#### *Network pruning results*

Fig. 4.2 shows the learning curve for a network trained using the sequential pruning protocol with TensorFlow's Model Optimization Toolkit (see Methods section for details) [2]. The network is trained until a minimum error is reached, and then pruned to a specified sparsity percentage and then retrained until the loss is once again minimized. The sparsity (or pruning) percentages are shown in Fig. 4.2 where they occur in the training process. A threshold error of $10^{-3}$ (shown as a red, dashed line) was chosen to define the sparsest optimal network. This threshold was chosen because it is near the performance of the trained, fully-connected network. In the example in Fig. 4.2, the sparsest optimal network occurs at 94% sparsity (or when only 6% of the connections remain). Beyond 94% sparsity, the performance of the network breaks down because too many critical weights have been removed.

#### *Monte Carlo results*

To compare results across networks, 1320 networks were trained with different random initialization on the same dataset. In training these networks, the hyper-parameters, pruning

percentages, and architecture are held constant. Fig. 4.3 shows the training curves of 9 sample networks. The red, dashed line in each of the panels represents the same threshold as in Fig. 4.2 ($10^{-3}$). The black, solid lines in Fig. 4.3 represent the sparsest, optimal network. Although the majority of networks in this subset breakdown at 93% sparsity, a few breakdown before and after.

On average, before pruning, the fully-connected networks reach a minimum loss of $10^{-3}$. The average loss of all the networks can be seen in Fig. 4.4. The first box in the box plot in Fig. 4.4 corresponds to the losses of all the trained networks before any pruning occurs. The variance on the loss is relatively small, but there are several outliers. Once again, the red, dashed line in the box plot in Fig. 4.4 represents the threshold. Many networks make it to 93% sparsity before the performance breakdown. Of the 1320 networks trained, 858 of the networks are optimally sparse at 93% sparsity. The optimal, sparse networks are shown in the bar plot at the top of Fig. 4.4. Note that the total number of networks represented in the bar plot does not add up to 1320. This is because several networks never perform below the threshold throughout the sequential pruning process (see outliers in Fig. 4.4).

*Analysis of layer sparsity*

The subset of optimally sparse networks pruned to 93% are used in the following analysis of network structure. The sparsity across all the layers was found to be uniform (7% of weights remain in each layer) despite not explicitly requiring that in the pruning protocol. Table 4.1 shows the average number of remaining connections across the 858 networks, as well as the variance and the fraction of remaining connections.

To study the affects of random network initialization on network structure, we trained and pruned 1320 networks and compared their performance. Fig. 4.4 shows the loss after pruning the 1320 networks at varying pruning percentages (from 0% sparsity to 98% sparsity). Fig. 4.4 can be compared directly to Fig. 4.2 but is the compilation of the results for many different networks. The networks do not all converge to the same set of weights, which is evident by the numerous outliers, as well as the variance around the average loss. Many networks, however follow a similar pattern and perform under the threshold under

they are more that 93% sparse. Some networks remain under the threshold up until 95% pruned. Many networks perform better when pruned up to 85% sparsity.

We looked at the subset of networks (858 networks) that were pruned to 93% sparsity. Fig. 4.5 shows a box plot of the number of connections from the input layer to the first hidden layer for the subset of pruned networks. Interestingly, the initial head-thorax angular velocity was completely pruned out of all of the networks in the subset, meaning it has no impact on the output and predictive power of the network. Additionally, the initial abdomen angular velocity connects to either zero, one, or two nodes in the second hidden layer, while all the other inputs are connected to at least 5% of the weights in the first hidden layer on average.

***Discussion***

In this study, we set out to investigate whether a sparse DNN can control a biological, motor-task (i.e. moth hovering). Taking inspiration from synaptic pruning found across wide ranging animal taxa, we pruned a DNN to different levels of sparsity in order to find the optimal sparse network capable of controlling moth hovering. The DNN uses data generated by the inertial dynamics model in [21] which models the forward problem of flight control. In this work, the DNN models the inverse problem of flight control by learning the controls given the initial and final state-space variables.

Through this work, we found that sparse DNNs are capable of solving the inverse problem of flight control, i.e. predicting the controls that are required for a moth to hover to a specified state-space. In addition, we demonstrate that across many networks, a network can be pruned by as much as 93% and perform comparably to the average performance of a fully-connected network. However, there are sharp performance limits and on average, most networks pruned beyond 93% see a breakdown in performance. We found that although uniform pruning was not enforced, on average, each layer in the network pruned to match the overall sparsity (i.e. sparsity of each layer was 93% for networks pruned to overall sparsity of 93%). Finally, we looked at the sparsity of individual layers and found that the initial head-thorax angular velocity is consistently pruned from the input layer of networks pruned to 93% sparsity, indicating a redundancy in the forward original model.

Though we have shown that a DNN is capable of learning the controls for a flight task, there are several limitations to this work. Firstly, though the model in [21] used to generate the training data provided control predictions for accurate motion tracking in a two-dimensional task, biological reality is more rich and complex than can be captured by the forward model. Thus, since the DNN is trained with this data, it is only capable of learning the dynamics captured in the model in [21]. Furthermore, the size, shape, and body biomechanics of this systems all matter. This study uses the same global parameters across the data set (see morphometrics measured in Chapter 2), but, in reality, these parameters vary significantly (across insect taxa and within the life of an individual) and this likely affects the performance of the DNN.

We have shown here that DNNs are capable of learning the inverse problem of flight control. The fully-connected DNN used here learned a nonlinear mapping between input and output variables, where the inputs are the initial and final state-space variables and the outputs are the controls and final velocities. On average, a fully-connected network can learn this task with a loss of approximately 0.001. However, due to the random initialization of weights preceding training, some networks perform as much as an order of magnitude worse (see Fig. 4.4). This suggests that the performance of a trained DNN is heavily influenced by the random initialization of its weights.

We used magnitude-based pruning to sparsify the DNNs in order to find the optimal, sparse network capable of controlling moth hovering. For the task of moth hovering, a DNN can be pruned to approximately 7% of its original network weights and still perform comparably to the fully-connected network. The results of this analysis show that when trained to perform a biological task, fully-connected DNNs are indeed overparameterized. Much like their biological counterparts, DNNs do not require fully-connected connectivity to accomplish this task. The performance threshold represented by the red dashed line in Figs. 4.2, 4.3, and 4.4 was chosen to represent a loss comparable to the loss of the fully-connected network (i.e. 0.001). In other words, this line represents a noise threshold, below which the network is considered well-performing. It has been shown that biological motor control systems are adapted to handle noise [50]. Biological pruning may be a mechanism for identifying sparse connectivity patterns that allow for control within a noise threshold.

On average, when the networks are pruned beyond 7% connectivity, there is a dramatic performance breakdown. Beyond 93% sparsity, the performance of the networks break down because too many critical weights have been removed. A significant proportion of the 1320 networks breakdown before they reach 7% connectivity (approximately 30% of the networks). This again supports the aforementioned claim that the random initialization of the weights before training affects the performance of a DNN and can be exacerbated by neural network pruning. Additionally, this shows that there exists a diversity of network structures that perform within the bounds of the noise threshold.

To investigate the substructure of the well-performing, sparse networks, we looked closer at the subset of networks that were optimally sparse at 93% pruned (858 networks). We have shown that the average sparsity of each layer in this subset is uniform, meaning each of the five layers have approximately 7% of their original connections remaining. However, the variance on the number of remaining connections between input layer and first hidden layer and between the final hidden layer and the output layer is markedly higher than the variance in the weight matrices between the hidden layers. This suggests that in networks pruned to 93% sparsity, the greatest amount of change in network connectivity occurs in input and output layers. However, there are notable features in the connectivity between the input and first hidden layer that are consistent across the 858 networks. Fig. 4.5 shows that the input parameter, initial head-thorax angular velocity ($\dot{\theta}_i$), is completely pruned from all of the 858 networks. The initial abdomen angular velocity ($\dot{\phi}_i$) is also almost entirely pruned from all of the networks. All of the other input parameters maintain an average of at least 5% connectivity to the first hidden layer. The complete pruning of $\dot{\theta}_i$ suggests a redundancy in the original forward model. However, this redundancy makes physical sense because $\theta_i$ and $\phi_i$ are coupled in the original forward model.

In this work, we have shown that a sparse neural network can learn the controls for a biological motor task and we have also shown, via Monte Carlo simulations, that there exists at least some aspects of network structure that are stereotypical. In future work, we will investigate network structure further by comparing network motifs across the 1320 networks. Network motifs are statistically significant substructures in a network and have been shown to be indicative of network functionality in control systems [63]. Other areas

of future work include investigating the sparse network's response to noise and changes in the biological parameters. Biological control systems are adapted to function adequately in the presence of noise. Does the sparsity of biological neural networks play a role in their response to a noisy environment? Furthermore, is a sparse neural network more equipped to handle changes in the biological parameters (such as size and shape of the simulated moth)?

## 4.1 *Figures for Chapter 4*

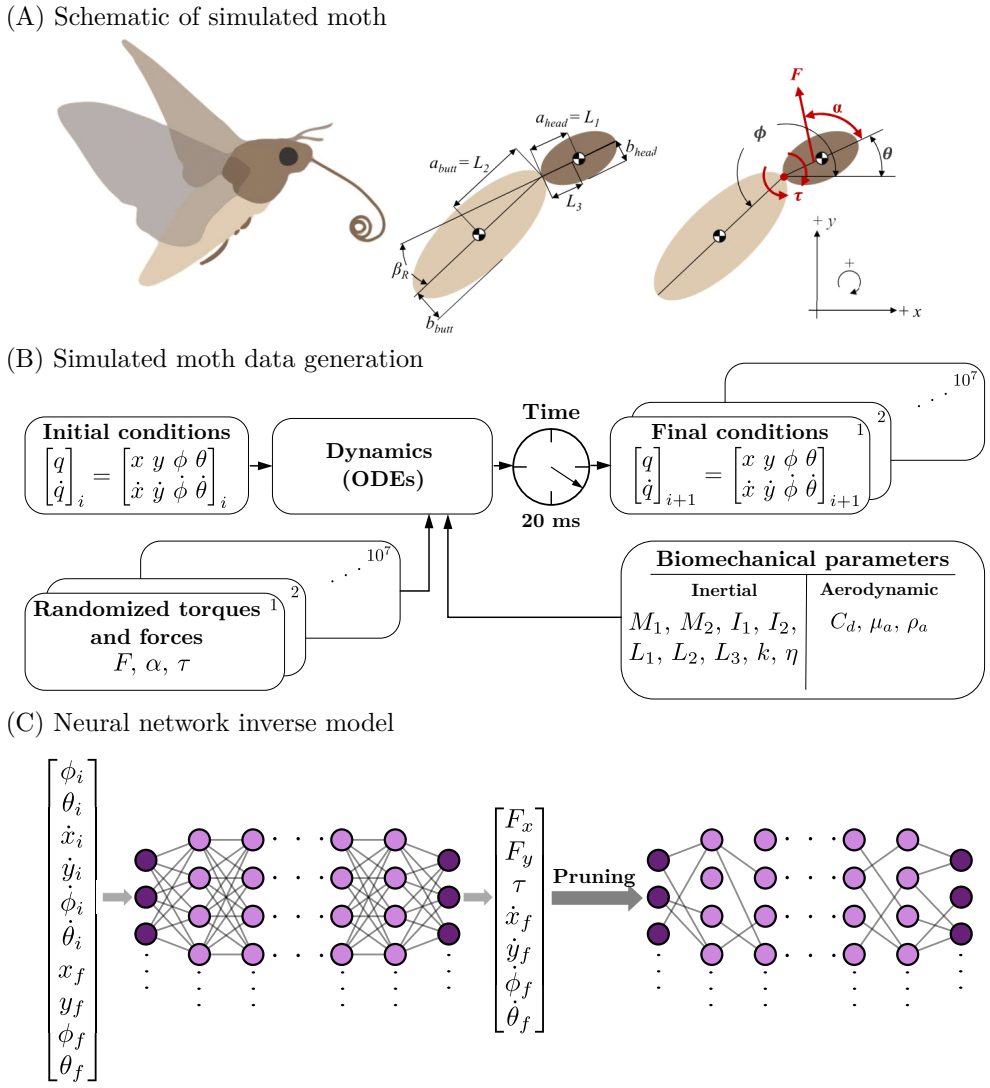


Figure 4.1: **Inverse problem of flight control.** (A) The moth body is made of two ellipses attached with a spring. There are three control variables ($F$, $\alpha$, and $\tau$) and four parameters to describe the state space ($x$, $y$, $\theta$, and $\phi$). See Table **??** and **??** for a full description of model parameters. (B) The differential equation solver solves the forward problem of insect flight control. (C) The neural network is an attempt to solve the inverse problem of flight control.

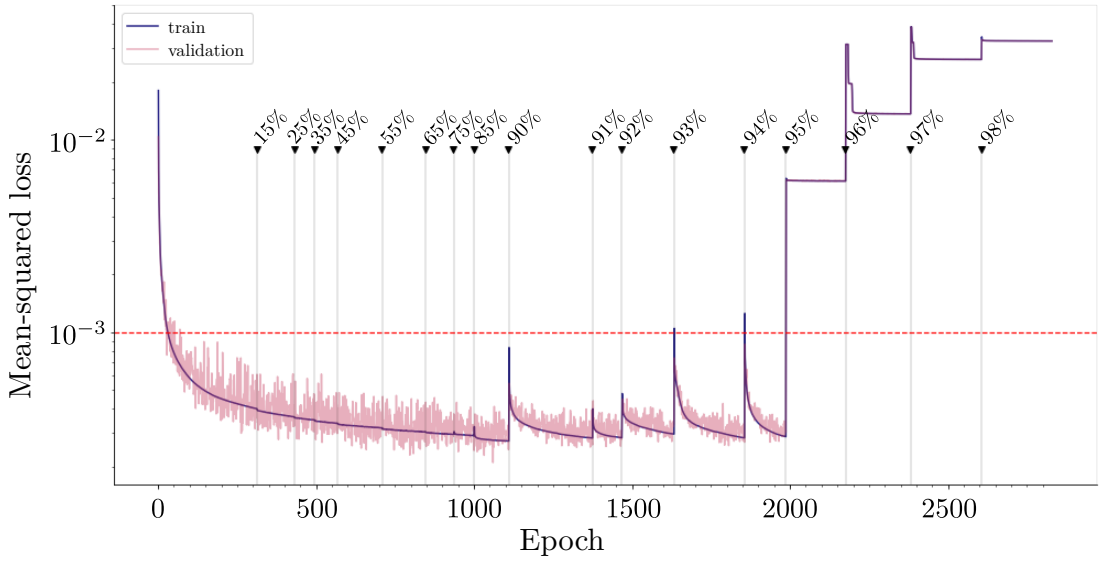


Figure 4.2: **Learning curve for sequential pruning of network.** Fully-connected neural network is trained until the mean-squared error is minimized. Then the network is sequentially pruned by adding in a masking layer and trained again. The performance of the network improves below the minimum error achieved by the fully connected network for low levels of pruning, but performs comparably to the fully-connected network until 95% of the network is pruned.

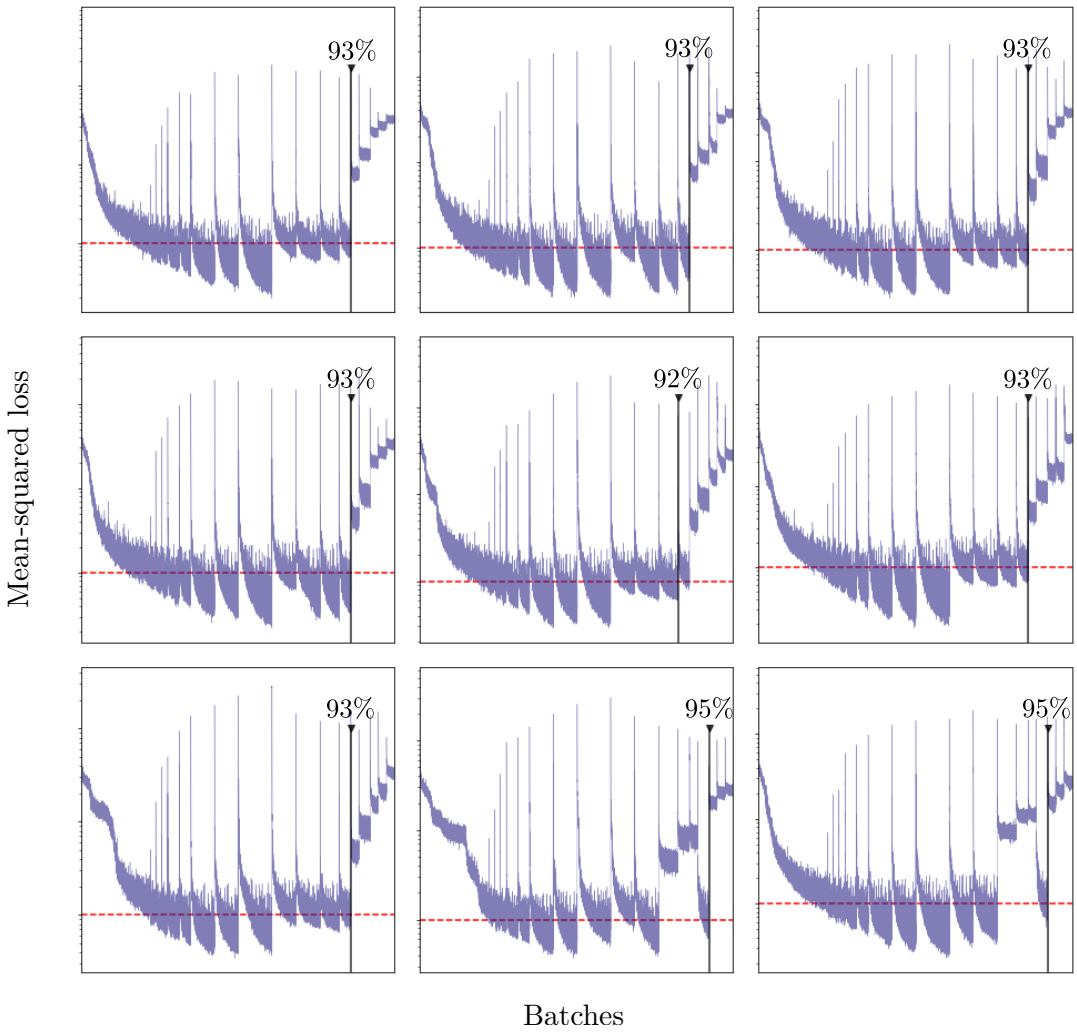


Figure 4.3: **Performance breakdown of 9 sample pruned networks.** The networks are sequentially pruned. Each network is evaluated to find the sparsest, optimally performing network. The red dashed line represents the performance threshold ($10^{-3}$). The sparsest network that performs below this threshold is shown by the solid, black vertical line.

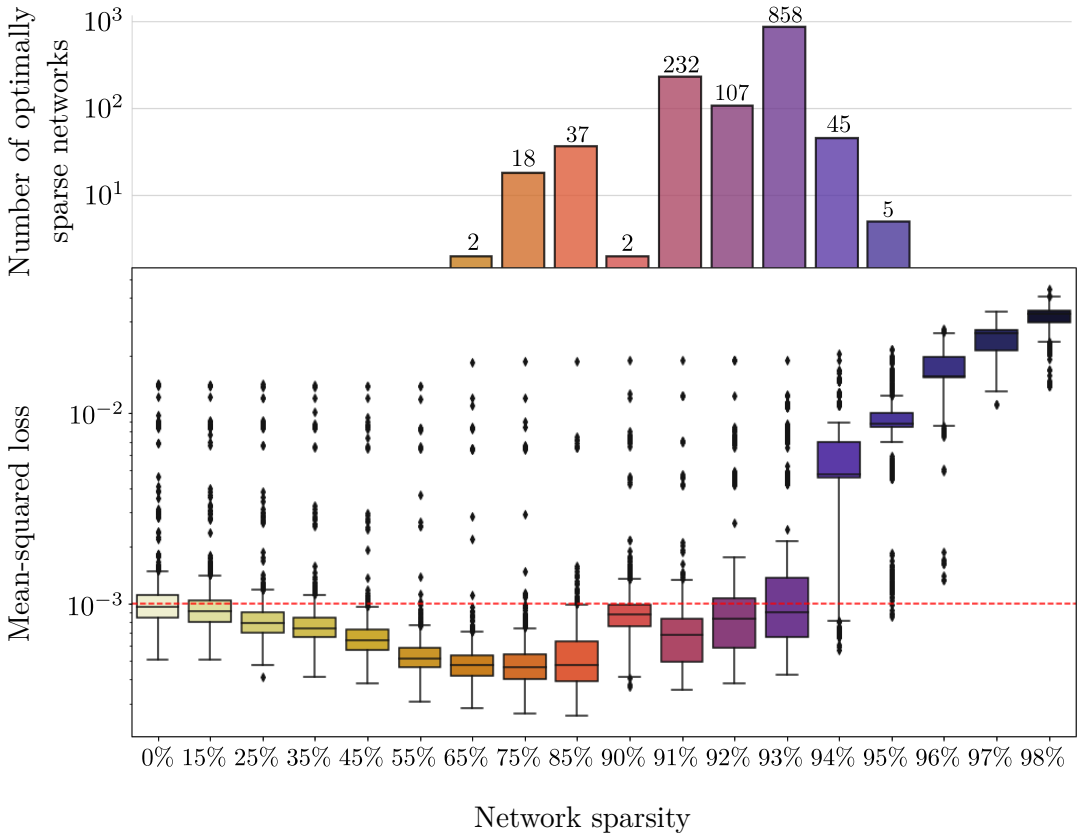


Figure 4.4: **Monte Carlo analysis of pruned networks.** 1306 networks are sequentially pruned and loss of the pruned networks at each sparsity percentage is recorded in the box plot. The bar plot records the number of networks that make it to the corresponding sparsity percentage before exceeding the hypothetical threshold ($10^{-3}$).

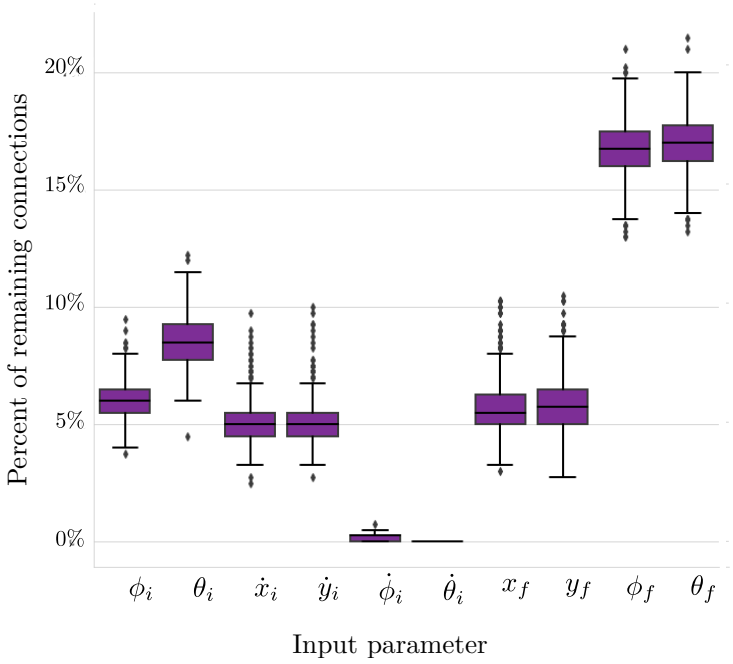


Figure 4.5: **Sparsity of input layer of networks pruned to** 93% **sparsity.** Each box represents the average number of connections remaining between a parameter in the input layer and the first hidden layer. For all 858 networks in this group, $\dot{\theta}_i$ was pruned entirely from the network.

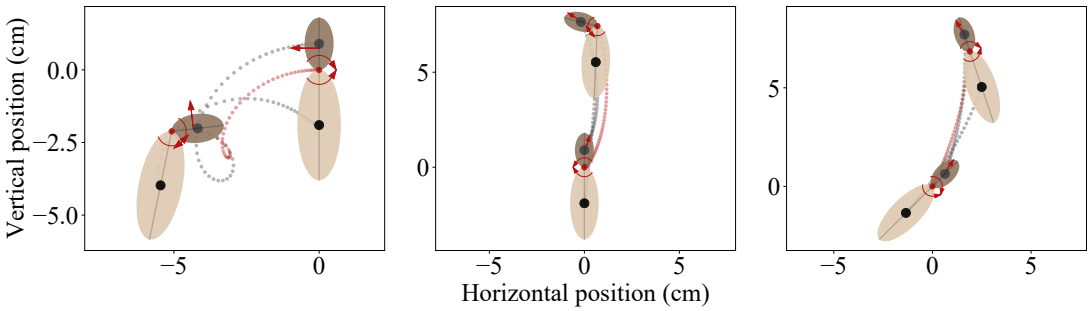


Figure 4.6: **Example trajectories of the simulated insects.** Each trajectory is 20 ms, and each starts at (x,y) = (0,0). Force ($F$) is indicated with the straight red arrow, and torque ($\tau$) is shown with the curved arrows at the thorax-abdomen joint (red dot). The center of mass of each body segment is shown with black dots.

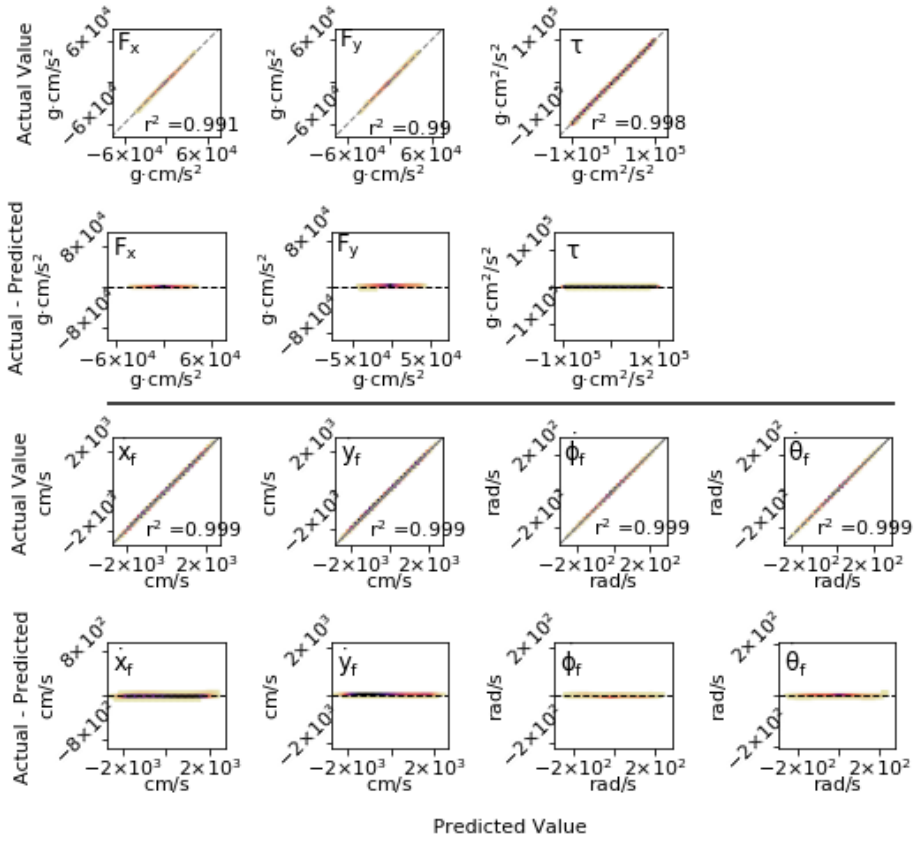


Figure 4.7: Error evaluation of a fully-connected network before any pruning. The seven parameters shown are the outputs of the network, the three control variables and the final derivatives of the state space. The residual plots are also shown (denoted by Actual - Prediction).

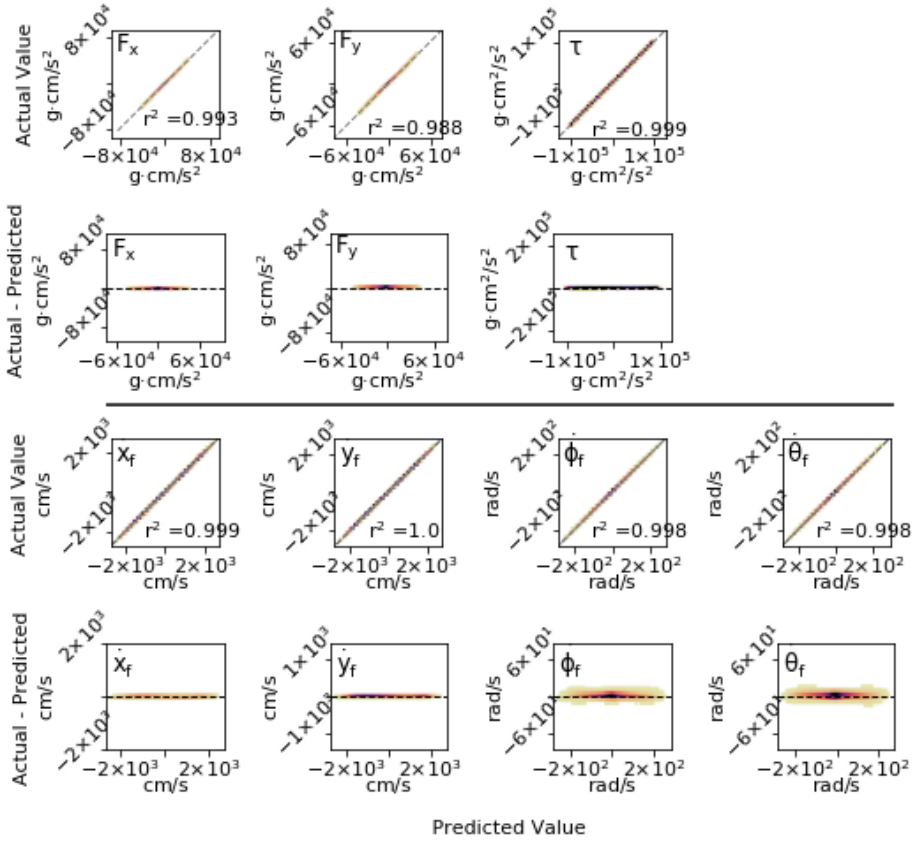


Figure 4.8: **Error evaluation (with pruning)** Note that axes for residual plots are scaled to include the max outliers

### *4.2 Table for Chapter 4*

| **Layer** $i$ | Average number remaining | Variance | Percentage remaining |
|---|---|---|---|
| 1 | 280 | 23 | 0.07 |
| 2 | 11199 | 0 | 0.07 |
| 3 | 11199 | 0 | 0.07 |
| 4 | 447 | 0.04 | 0.07 |
| 5 | 8 | 6 | 0.07 |

Table 4.1: **Number of remaining parameters in networks pruned to 93% sparsity** This table gives the average number of remaining weights in each layer of the networks pruned to 93% sparsity. The variance on the number of connections, as well as the fraction of remaining connections are also given.

***Acknowledgments for Chapter 4***

We gratefully acknowledge the support of NVIDIA Corporation with the donation of the Titan Xp GPU used for this research. This work was supported by AFOSR Grant (Nature-Inspired Flight Technology and Ideas, FA9550-14-1-0398) to TLD and the Komen Endowed Chair to TLD. CMS was supported in part by the University of Washington Data Science Grant from the Moore Foundation, Sloan Foundation, and the Washington Research Foundation. JB was supported in part by the National Science Foundation Graduate Research Fellowship Program. JNK acknowledges support from the Air Force Office of Scientific Research FA9550-19-1-0386.

# BIBLIOGRAPHY

[1] Metamorphosis of the insect nervous system: Changes in morphology and synaptic interactions of identified neurones. *Nature*, 299:250–252, 1982.

[2] Martín Abadi, Ashish Agarwal, Paul Barham, Eugene Brevdo, Zhifeng Chen, Craig Citro, Greg S. Corrado, Andy Davis, Jeffrey Dean, Matthieu Devin, Sanjay Ghemawat, Ian Goodfellow, Andrew Harp, Geoffrey Irving, Michael Isard, Yangqing Jia, Rafal Jozefowicz, Lukasz Kaiser, Manjunath Kudlur, Josh Levenberg, Dandelion Mané, Rajat Monga, Sherry Moore, Derek Murray, Chris Olah, Mike Schuster, Jonathon Shlens, Benoit Steiner, Ilya Sutskever, Kunal Talwar, Paul Tucker, Vincent Vanhoucke, Vijay Vasudevan, Fernanda Viégas, Oriol Vinyals, Pete Warden, Martin Wattenberg, Martin Wicke, Yuan Yu, and Xiaoqiang Zheng. TensorFlow: Large-scale machine learning on heterogeneous systems, 2015. Software available from tensorflow.org.

[3] Pablo A. E. Alarcón, Juan M. Morales, José A. Donázar, José A. Sánchez-Zapata, Fernando Hiraldo, and Sergio A. Lambertucci. Sexual-size dimorphism modulates the trade-off between exploiting food and wind resources in a large avian scavenger. *Scientific Reports*, 7(11461):1–9, 2017.

[4] Robert McNeill Alexander. The lift produced by the heterocercal tails of selachii. *Journal of Experimental Biology*, 43(1):131–138, 1965.

[5] Robert McNiell Alexander. Models and scaling of energy costs for locomotion. *Journal of Experimental Biology*, 208(9):1645–1652, 2005.

[6] B. R. Anholt, J. H. Marden, and D. M. Jenkins. Patterns of mass gain and sexual dimorphism in adult dragonflies (insecta: Odonata). *Canadian Journal of Zoology*, 69:1156–1163, 1991.

[7] Tsevi Beatus and Itai Cohen. Wing-pitch modulation in maneuvering fruit flies is explained by an interplay between aerodynamics and a torsional spring. *Physical Review E*, 92(022712):1–13, 2015.

[8] John Bender and Michael Dickinson. A comparison of visual and haltere-mediated feedback in the control of body saccades in *Drosophila melanogaster*. *Journal of Experimental Biology*, 2006.

[9] Simon Benhamou. How to reliably estimate the tortuosity of an animal's path:: straightness, sinuosity, or fractal dimension? *Journal of Theoretical Biology*, 229(2):209–220, 2004.

[10] Leon Bennett. Insect flight: Lift and rate of change of incidence. *Science*, 167(3519):177–179, 1970.

[11] Leon Bennett. Clap and fling aerodynamics - an experimental evaluation. *Journal of Experimental Biology*, 69(1):261–272, 1977.

[12] Gordon Berman and Jane Z. Wang. Energy-minimizing kinematics in hovering insect flight. *The Journal of Fluid Mechanics*, 582:153–168, 2007.

[13] D. Berrigan. Lift production in the flesh fly, *Neobellieria* (= sarcophaga) *bullata* parker. *British Ecological Society*, 5(3):448–456, 1991.

[14] Ruben Berthé and Fritz-Olaf Lehmann. Body appendages fine-tune posture and moments in freely manoeuvring fruit flies. *Journal of Experimental Biology*, 2015.

[15] Katharina Bieker, Sebastian Peitz, Steven L. Brunton, J. Nathan Kutz, and Michael Dellnitz. Deep model predictive flow control with limited sensor data and online learning. *Theoretical and Computational Fluid Dynamics*, 34(4):577–591, Mar 2020.

[16] Richard J. Bomphrey, Toshiyuki Nakata, Nathan Phillips, and Simon M. Walker. Smart wing rotation and trailing-edge vortices enable high frequency mosquito flight. *Nature*, 544:92–95, 2017.

[17] Patrick Bouffard, Anil Aswani, and Claire Tomlin. Learning-based model predictive control on a quadrotor: Onboard implementation and experimental results. In *2012 IEEE International Conference on Robotics and Automation*, pages 279–284, 2012.

[18] James Bradbury, Roy Frostig, Peter Hawkins, Matthew James Johnson, Chris Leary, Dougal Maclaurin, George Necula, Adam Paszke, Jake VanderPlas, Skye Wanderman-Milne, and Qiao Zhang. JAX: composable transformations of Python+NumPy programs. 2018.

[19] Tom B. Brown, Benjamin Mann, Nick Ryder, Melanie Subbiah, Jared Kaplan, Prafulla Dhariwal, Arvind Neelakantan, Pranav Shyam, Girish Sastry, Amanda Askell, Sandhini Agarwal, Ariel Herbert-Voss, Gretchen Krueger, Tom Henighan, Rewon Child, Aditya Ramesh, Daniel M. Ziegler, Jeffrey Wu, Clemens Winter, Christopher Hesse, Mark Chen, Eric Sigler, Mateusz Litwin, Scott Gray, Benjamin Chess, Jack Clark, Christopher Berner, Sam McCandlish, Alec Radford, Ilya Sutskever, and Dario Amodei. Language models are few-shot learners, 2020.

[20] Malcolm Burrows, Darron A. Cullen, Marina Dorosenko, and Gregory P. Sutton. Mantises exchange angular momentum between three rotating body parts to jump precisely to targets. *Current Biology*, 25(6):786–789, 2015.

[21] Jorge Bustamante, Jr., Mahad Ahmed, Tanvi Deora, Brian Fabien, and Thomas L. Daniel. Abdominal movements in insect flight reshape the role of non-aerodynamic structures for flight maneuverability i: Model predictive control for flower tracking. *Integrative Organismal Biology*, tbd(tbd):tbd, In review, 2021.

[22] Jorge Bustamante, Jr., Tanvi Deora, and Thomas L. Daniel. Abdominal movements in insect flight reshape the role of non-aerodynamic structures for flight maneuverability ii: performance trade-offs of inertial, elastic, and morphological determinants of flight. *Integrative Organismal Biology*, tbd(tbd):tbd, In prep, 2021.

[23] Jeffrey M. Camhi. Sensory control of abdomen posture in flying locusts. *The Journal of Experimental Biology*, 52:533–537, 1970.

[24] Eric O. Campos, Harvey D. Bradshaw Jr, and Thomas L. Daniel. Shape matters: corolla curvature improves nectar discovery in the hawkmoth *Manduca sexta*. *Functional Ecology*, 29:462–468, 2015.

[25] Reginald Frederick Chapman. *The Insects: Structure and Function*. Cambridge University Press, 2013.

[26] Gal Chechik, Isaac Meilijson, and Eytan Ruppin. Synaptic Pruning in Development: A Computational Account. *Neural Computation*, 10(7):1759–1777, 10 1998.

[27] François Chollet et al. Keras. https://keras.io, 2015.

[28] A. N. Clements. *The Physiology of Mosquitoes*. Permagon, 1963.

[29] S. A. Combes, D. E. Rundle, J. M. Iwasaki, and J. D. Crall. Linking biomechanics and ecology through predator–prey interactions: flight performance of dragonflies and their prey. *Journal of Experimental Biology*, 215:903–913, 2012.

[30] S. A. Combes, M. K. Salcedo, M. M. Pandit, and J. M. Iwasaki. Capture success and efficiency of dragonflies pursuing different types of prey. *Integrative and Comparative Biology*, 53(5):787–798, 2013.

[31] Stacey A. Combes and Robert Dudley. Turbulence-driven instabilities limit insect flight performance. *Proceedings of the National Academy of Sciences*, 106(22):9105–9108, 2009.

[32] Noah J. Cowan, Mert M. Ankarali, Jonathan P. Dyhr, Manu S. Madhav, Eatai Roth, Shahin Sefati, Simon Sponberg, Sarah A. Stamper, Eric S. Fortune, and Thomas L. Daniel. Feedback control as a framework for understanding tradeoffs in biology. *Integrative and Comparative Biology*, 2014.

[33] Fergus I.M. Craik and Ellen Bialystok. Cognition through the lifespan: mechanisms of change. *Trends in Cognitive Sciences*, 10(3):131–138, 2006.

[34] A. Demir, M. Mert Ankarali, J. P. Dyhr, K. A. Morgansen, T. L. Daniel, and N. J. Cowan. Inertial stabilization of thrust forces for flight stabilization. *Adaptive Mobile Robotics*, 2012.

[35] Tanvi Deora, Mahad A. Ahmed, Thomas L. Daniel, and Bingni W. Brunton. Tactile active sensing in insect-plant pollination. *The Journal of Experimental Biology*, 224:4, 2021.

[36] Tanvi Deora, Namrata Gundiah, and Sanjay P. Sane. Mechanics of the thorax in flies. *Journal of Experimental Biology*, 220(8):1382–1395, 2017.

[37] M. H. Dickinson and K. G. Gotz. Unsteady aerodynamic performance of model wings at low reynolds numbers. *Journal of Experimental Biology*, 174(1):45–64, 1993.

[38] Michael Dickinson. Insect flight. *Current Biology*, 2006.

[39] Michael H. Dickinson. The effects of wing rotation on unsteady aerodynamic performance at low reynolds numbers. *Journal of Experimental Biology*, 192(1):179–206, 1994.

[40] Michael H. Dickinson. Unsteady mechanisms of force generation in aquatic and aerial locomotion. *American Zoologist*, 36(6):537–554, 1996.

[41] Michael H. Dickinson, Fritz-Olaf Lehmann, and Sanjay P. Sane. Wing rotation and the aerodynamic basis of insect flight. *Science*, 284(5422):1954–1960, 1999.

[42] William Dickson, Andrew Straw, Christian Poelma, and Michael Dickinson. An integrative model of insect flight control. *AIAA Aerospace Meetings*, 2012.

[43] Elizabeth M. Dlugosz, Mark A. Chappell, David G. McGillivray, Douglas A. Syme, and Jr Theodore Garland. Locomotor trade-offs in mice selectively bred for high voluntary wheel running. *Journal of Experimental Biology*, 212(16):2612–2618, 2009.

[44] E. G. Drucker and George V. Lauder. Locomotor forces on a swimming fish: three-dimensional vortex wake dynamics quantified using digital particle image velocimetry. *Journal of Experimental Biology*, 202(18):2393–2412, 1999.

[45] Jonathan P. Dyhr, Kristi A. Morgansen, Thomas L. Daniel, and Noah J. Cowan. Flexible strategies for flight control: an active role for the abdomen. *The Journal of Experimental Biology*, 216:1523–1536, 2013.

[46] J. D. Edman and William L. Bidlingmayer. Flight capacity of blood-engorged mosquitoes. *Mosquito News*, 29(3):386–392, 1969.

[47] C. P. Ellington. The aerodynamics of hovering insect flight. iii. kinematics. *Philosophical Transactions of the Royal Society B*, 305(1122):41–78, 1973.

[48] C. P. Ellington. Limitations on animal flight performance. *Journal of Experimental Biology*, 160(1):71–91, 1991.

[49] L. Ferry and George V. Lauder. Heterocercal tail function in leopard sharks: a three-dimensional kinematic analysis of two models. *Journal of Experimental Biology*, 199(10):2253–2268, 1996.

[50] David W. Franklin and Daniel M. Wolpert. Computational mechanisms of sensorimotor control. *Neuron*, 72(3):425–442, 2011.

[51] Robert J. Full. Mechanics and energetics of terrestrial locomotion: Bipeds to polypeds. *Energy Transformations in Cells and Animals*, pages 175–182, 1989.

[52] Robert J. Full, D. A. Zuccarello, and A. Tullis. Effect of variation in form on the cost of terrestrial locomotion. *Journal of Experimental Biology*, 150(1):233–246, 1990.

[53] James D Gardiner, Grigorios Dimitriadis, Jonathan R Codd, and Robert L Nuddes. A potential role for bat tail membranes in flight control. *PLOS One*, 2011.

[54] Crawford H. Greenewalt. The flight of birds: The significant dimensions, their departure from the requirements for dimensional similarity, and the effect on flight aerodynamics of that departure. *Transactions of the American Philosophical Society*, 65(4):1–67, 1975.

[55] Robert W. Gwadz. Regulation of blood meal size in the mosquito. *Journal of Insect Physiology*, 15(11):2039–2042, 1969.

[56] Charles R. Harris, K. Jarrod Millman, Stéfan J. van der Walt, Ralf Gommers, Pauli Virtanen, David Cournapeau, Eric Wieser, Julian Taylor, Sebastian Berg, Nathaniel J. Smith, Robert Kern, Matti Picus, Stephan Hoyer, Marten H. van Kerkwijk, Matthew Brett, Allan Haldane, Jaime Fernández del Río, Mark Wiebe, Pearu Peterson, Pierre Gérard-Marchant, Kevin Sheppard, Tyler Reddy, Warren Weckesser, Hameer Abbasi, Christoph Gohlke, and Travis E. Oliphant. Array programming with NumPy. *Nature*, 585(7825):357–362, September 2020.

[57] J.E. Harris. The role of the fins in the equilibrium of the swimming fish : Ii. the role of the pelvic fins. *Journal of Experimental Biology*, 15(1):32–47, 1938.

[58] Babak Hassibi, David G Stork, and Gregory J Wolff. Optimal brain surgeon and general network pruning. In *IEEE international conference on neural networks*, pages 293–299. IEEE, 1993.

[59] Tyson L. Hedrick and Thomas Lewis Daniel. Flight control in the hawkmoth *Manduca sexta*: the inverse problem of hovering. *The Journal of Experimental Biology*, 209:3114–3130, 2006.

[60] B. T. Hinson, E. Rombokas, J. P. Dyhr, T. L. Daniel, and K. A. Morgansen. Sensing from control: Airframe deformation for simultaneous actuation and state estimation. pages 2683–2690, 2013.

[61] Armin J. Hinterwirth and Thomas L. Daniel. Antennae in the hawkmoth *Manduca sexta* (lepidoptera, sphingidae) mediate abdominal flexion in response to mechanical stimuli. *Journal of Comparative Physiology A*, 196:947–956, 2010.

[62] Geoffrey Hinton, Nitish Srivastava, and Kevin Swersky. Neural networks for machine learning lecture 6a overview of mini-batch gradient descent, 2012.

[63] Yu Hu, Steven L. Brunton, Nicholas Cain, Stefan Mihalas, J. Nathan Kutz, and Eric Shea-Brown. Feedback through graph motifs relates structure and function in complex networks. *Physical Review E*, 98(6), Dec 2018.

[64] John T. Huber and John S. Noyes. A new genus and species of fairyfly, *Tinkerbella nana* (hymenoptera, mymaridae), with comments on its sister genus *Kikiki*, and discussion on small size limits in arthropods. *Journal of Hymenoptera Research*, 32:17–44, 2013.

[65] Mark Jankauski, Tom Lewis Daniel, and I Y Shen. Asymmetries in wing inertial and aerodynamic torques contribute to steering in flying insects. *Bioinspiration and Biomimetics*, 12(4), 2017.

[66] Jeeva Jayakumar, Kei Senda, and Naoto Yokoyama. Control of pitch attitude by abdomen during forward flight of two-dimensional butterfly. *Journal of Aircraft*, 55(6):1–11, 2018.

[67] Bruce C. Jayne, Adrian F. Lozada, and George V. Lauder. Function of the dorsal fin in bluegill sunfish: Motor patterns during four distinct locomotor behaviors. *Journal of Morphology*, 228(3):307–326, 1996.

[68] Geoffrey M. Jeffery. Blood meal volume in *Anopheles quadrimaculatus*, *A. albimanus* and *Aedes aegypti*. *Experimental Parasitology*, 5(4):371–375, 1956.

[69] Roxana B. Josens and Walter M. Farina. Nectar feeding by the hovering hawk moth *Macroglossum stellatarum*: intake rate as a function of viscosity and concentration of sucrose solutions. *Journal of Comparative Physiology A*, 187:661–665, 2001.

[70] Paul S Katz. Evolution and development of neural circuits in invertebrates. *Current Opinion in Neurobiology*, 17(1):59–64, 2007. Development.

[71] Mahdi Khoramshahi, Hamed Jalaly Bidgoly, Soroosh Shafiee, Ali Asaei, Auke Jan Ijspeertb, and Majid Nili Ahmadabadia. Piecewise linear spine for speed–energy efficiency trade-off in quadruped robots. *Robotics and Autonomous Systems*, 61(12):1350–1359, 2013.

[72] Dong-Wook Kim, Jin dong Yeo, and Jeong-Kyu Kim. Revision of the family sphecidae (hymenoptera: Apoidea) in south korea. *Annual Review of Ecology and Systematics*, 44(6):271–292, 2014.

[73] Diederik P. Kingma and Jimmy Ba. Adam: A method for stochastic optimization, 2017.

[74] Jamie M. Kneitel and Jonathan M. Chase. Trade-offs in community ecology: linking spatial scales and species coexistence. *Ecology Letters*, 7:69–80, 2004.

[75] Andrey Kuzmin, Markus Nagel, Saurabh Pitre, Sandeep Pendyam, Tijmen Blankevoort, and Max Welling. Taxonomy and evaluation of structured compression of convolutional neural networks, 2019.

[76] George V. Lauder. Caudal fin locomotion in ray-finned fishes: Historical and functional analyses. *American Zoologist*, 29(1):85–102, 1989.

[77] George V. Lauder. Function of the caudal fin during locomotion in fishes: Kinematics, flow visualization, and evolutionary patterns. *American Zoologist*, 40(1):101–122, 2000.

[78] Yann LeCun, Yoshua Bengio, and Geoffrey Hinton. Deep learning. *Nature*, 521(7553):436–444, 2015.

[79] Yann LeCun, John Denker, and Sara Solla. Optimal brain damage. In D. Touretzky, editor, *Advances in Neural Information Processing Systems*, volume 2. Morgan-Kaufmann, 1990.

[80] Thomas Libby, Talia Y. Moore, Evan Chang-Siu, Deborah Li, Daniel J. Cohen, Ardian Jusufi, and Robert J. Full. Tail-assisted pitch control in lizards, robots and dinosaurs. *Nature*, 481:181–184, 2012.

[81] M. J. Lighthill. On the weis-fogh mechanism of lift generation. *Journal of Fluid Mechanics*, 60(1):1–17, 1973.

[82] Christos Louizos, Karen Ullrich, and Max Welling. Bayesian compression for deep learning, 2017.

[83] Christos Louizos, Max Welling, and Diederik P. Kingma. Learning sparse neural networks through $l_0$ regularization, 2018.

[84] Bethany Lusch, J. Nathan Kutz, and Steven L. Brunton. Deep learning for universal linear embeddings of nonlinear dynamics. *Nature Communications*, 9(1), Nov 2018.

[85] Alexander Mathis, Pranav Mamidanna, Kevin M. Cury, Taiga Abe, Venkatesh N. Murthy, Mackenzie Weygandt Mathis, and Matthias Bethge. Deeplabcut: markerless pose estimation of user-defined body parts with deep learning. *Nature Neuroscience*, 21:1281–1289, 2018.

[86] A. A. Mian and W. Daobo. Nonlinear flight control strategy for an underactuated quadrotor aerial robot. pages 938–942, 2008.

[87] Matteo Mischiati, Huai-Ti Lin, Paul Herold, Elliot Imler, Robert Olberg, and Anthony Leonardo. Internal models direct dragonfly interception steering. *Nature*, 517:333–338, 2015.

[88] Decebal Constantin Mocanu, Elena Mocanu, Peter Stone, Phuong H. Nguyen, Madeleine Gibescu, and Antonio Liotta. Scalable training of artificial neural networks with adaptive sparse connectivity inspired by network science. *Nature Communications*, 9(1), Jun 2018.

[89] K.A. Morgansen, V. Duidam, R.J. Mason, J.W. Burdick, and R.M. Murray. Nonlinear control methods for planar carangiform robot fish locomotion. *IEEE*, 1:427–434, 2001.

[90] Yash Mulgaonkar, Michael Whitzer, Brian Morgan, Christopher M. Kroninger, Aaron M. Harrington, and Vijay Kumar. Power and weight considerations in small, agile quadrotors. *Proceedings SPIE*, 9083:90831Q–1 – 90831Q–16, 2014.

[91] Yonatan Munk, Stephen P. Yanoviak, M. A. R. Koehl, and Robert Dudley. The descent of ant: field-measured performance of gliding ants. *The Journal of Experimental Biology*, 218(9):1393–1401, 2015.

[92] Ami Fadhillah Amir Abdul Nasir, Christofer J. Clemente, Melissa L. Wynn, and Robbie S. Wilson. Optimal running speeds when there is a trade-off between speed and the probability of mistakes. *Functional Ecology*, 31(10):1941–1949, 2017.

[93] NVIDIA, Péter Vingelmann, and Frank H.P. Fitzek. Cuda, release: 10.2.89, 2020.

[94] Titilayo Ogunwa, Blake McIvor, Nurkhairunisa Awang Jumat, Ermira Abdullah, and Javaan Chahl. Longitudinal actuated abdomen control for energy efficient flight of insects. *Energies*, 13(20):5480–5502, 2020.

[95] R. M. Olberg, R. C. Seaman, M. I. Coats, and A. F. Henry. Eye movements and target fixation during dragonfly prey-interception flights. *Journal of Comparative Physiology A*, 193:685–693, 2007.

[96] R. M. Olberg, A. H. Worthington, J. L. Fox, C. E. Bessette, and M. P. Loosemore. Prey size selection and distance estimation in foraging adult dragonflies. *Journal of Comparative Physiology A*, 191:791–797, 2005.

[97] R. M. Olberg, A. H. Worthington, and K. R. Venator. Prey pursuit and interception in dragonflies. *Journal of Comparative Physiology A*, 186:155–162, 2000.

[98] Edward C. Polhamus. Predictions of vortex-lift characteristics by a leading-edge suctionanalogy. *Journal of Aircraft*, 8(4):193–199, 1971.

[99] Robert A. Raguso, Cynthia Henzel, Stephen L. Buchmann, and Gary P. Nabhan. Trumpet flowers of the sonoran desert: Floral biology of *Peniocereus* cacti and sacred *Datura*. *International Journal of Plant Sciences*, 164(6):877–892, 2003.

[100] Robert A. Raguso and Mark A. Willis. Synergy between visual and olfactory cues in nectar feeding by naïve hawkmoths, *Manduca sexta*. *Animal Behaviour*, 64:685–695, 2002.

[101] Robert A. Raguso and Mark A. Willis. Synergy between visual and olfactory cues in nectar feeding by wild hawkmoths, *Manduca sexta*. *Animal Behaviour*, 69:407–418, 2005.

[102] David M. Raup. Geometric analysis of shell coiling: General problems. *Journal of Paleontology*, 40(5):1178–1190, 1966.

[103] David M. Raup and Arnold Michelson. Theoretical morphology of the coiled shell. *Science*, 147:1294–1295, 1965.

[104] Gal Ribak, Moshe Gish, Daniel Weihs, and Moshe Inbar. Adaptive aerial righting during the escape dropping of wingless pea aphids. *Current Biology*, 23(3):R102–R103, 2013.

[105] Jeffrey A. Riffell, Hong Lei, Leif Abrell, and John G. Hildebrand. Neural basis of a pollinator's buffet: Olfactory specialization and learning in *Manduca sexta*. *Science*, 339(6116):200–204, 2013.

[106] L. J. Rosenberger. Pectoral fin locomotion in batoid fishes: undulation versus oscillation. *Journal of Experimental Biology*, 204(2):379–394, 2001.

[107] Eatai Roth, Robert W. Hall, Thomas Lewis Daniel, and Simon Sponberg. Integration of parallel mechanosensory and visual pathways resolved through sensory conflict. *Proceedings of the National Academy of Sciences*, 113(45):12832–12837, 2016.

[108] Sanjay P. Sane. The aerodynamics of insect flight. *Journal of Experimental Biology*, 206(23):4191–4208, 2003.

[109] Sanjay P. Sane and Michael H. Dickinson. The control of flight force by a flapping wing: lift and drag production. *Journal of Experimental Biology*, 204(15):2607–2626, 2001.

[110] Sanjay P. Sane and Michael H. Dickinson. The aerodynamic effects of wing rotation and a revised quasi-steady model of flapping flight. *Journal of Experimental Biology*, 205(8):1087–1096, 2002.

[111] Simone Scardapane, Danilo Comminiello, Amir Hussain, and Aurelio Uncini. Group sparse regularization for deep neural networks. *Neurocomputing*, 241:81–89, Jun 2017.

[112] Knut Schmidt-Nielsen. Energy cost of swimming, flying, and running. *Science*, 177(4045):222–228, 1972.

[113] Knut Schmidt-Nielsen. Locomotion: energy cost of swimming, flying and running. *Science*, 177:222–228, 1972.

[114] F. Seow-Choen. The longest insect in the world. *The Malayan Naturalist*, 48:12, 1995.

[115] Saeed Shamaghdari, S.K.Y. Nikravesh, and Mohammad Haeri. Integrated guidance and control of elastic flight vehicle based on robust mpc. *International Journal of Robust and Nonlinear Control*, 25(15):2608–2630, 2015.

[116] A. Shkolnik and R. Tedrake. High-dimensional underactuated motion planning via task space control. pages 3762–3768, 2008.

[117] Simon Sponberg, Jonathan P. Dyhr, Robert W. Hall, and Thomas Lewis Daniel. Luminance-dependent visual processing enables moth flight in low light. *Science*, 348(6240):1245–1248, 2015.

[118] Jordanna D. H. Sprayberry and Thomas L. Daniel. Flower tracking in hawkmoths: behavior and energetics. *Journal of Experimental Biology*, 210(1):37–45, 2007.

[119] Nitish Srivastava, Geoffrey Hinton, Alex Krizhevsky, Ilya Sutskever, and Ruslan Salakhutdinov. Dropout: A simple way to prevent neural networks from overfitting. *Journal of Machine Learning Research*, 15(56):1929–1958, 2014.

[120] Thomas J. Stastny, Adyasha Dash, and Roland Siegwart. *Nonlinear MPC for Fixed-wing UAV Trajectory Tracking: Implementation and Flight Experiments*. 2017.

[121] Marc L. Steinberg and Anthony B. Page. Nonlinear adaptive flight control with genetic algorithm design optimization. 1999.

[122] Jian-Yuan Su, Shang-Chieh Tin, Yu-Hung Chang, and Jing-Tang Yang. A passerine spreads its tail to facilitate a rapid recovery of its body posture during hovering. *The Journal of the Royal Society Interface*, 9:3114–3130, 2012.

[123] Graham Taylor. Mechanics and aerodynamics of insect flight control. *Biological Reviews*, 2001.

[124] Graham Taylor and Holger Krapp. Sensory systems and flight stability: What do insects measure and why? *Advances in Insect Physiology*, 2007.

[125] K. C. Tejaswi, Madhu K. Sridhar, Chang-kwon Kang, and Taeyoung Lee. Effects of abdomen undulation in energy consumption and stability for monarch butterfly. *Bioinspiration & Biomimetics*, 16(4):1–20, 2021.

[126] Adrian Thomas. Why do birds have tails? the tail as a drag reducing flap, and trim control. *The Journal of Theoretical Biology*, 183:3114–3130, 1996.

[127] Pauli Virtanen, Ralf Gommers, Travis E. Oliphant, Matt Haberland, Tyler Reddy, David Cournapeau, Evgeni Burovski, Pearu Peterson, Warren Weckesser, Jonathan Bright, Stéfan J. van der Walt, Matthew Brett, Joshua Wilson, K. Jarrod Millman, Nikolay Mayorov, Andrew R. J. Nelson, Eric Jones, Robert Kern, Eric Larson, CJ Carey, İlhan Polat, Yu Feng, Eric W. Moore, Jake Vand erPlas, Denis Laxalde, Josef Perktold, Robert Cimrman, Ian Henriksen, E. A. Quintero, Charles R Harris, Anne M. Archibald, Antônio H. Ribeiro, Fabian Pedregosa, Paul van Mulbregt, and SciPy 1. 0 Contributors. SciPy 1.0–Fundamental Algorithms for Scientific Computing in Python. *arXiv e-prints*, page arXiv:1907.10121, Jul 2019.

[128] Steven Vogel. *Life in Moving Fluids*. Princeton University Press, 1994.

[129] Fernando Vonhoff and Haig Keshishian. Activity-dependent synaptic refinement: New insights from drosophila. *Frontiers in Systems Neuroscience*, 11:23, 2017.

[130] P. B. Walker. Experiments on the growth of circulation about a wing and an apparatus for measuring fluid motion. *Rep. Memo. Aeronaut. Res. (Great Britain)*, (1402), 1931.

[131] Trevor J. Wardill, Samuel T. Fabian, Ann C. Pettigrew, Doekele G. Stavenga, Karin Nordström, and Paloma T. Gonzalez-Bellido. A novel interception strategy in a miniature robber fly with extreme visual acuity. *Current Biology*, 27(6):854–859, 2017.

[132] Torkel Weis-Fogh. Quick estimates of flight fitness in hovering animals, including novel mechanisms for lift production. *Journal of Experimental Biology*, 59(1):169–230, 1973.

[133] Rebecca Wheatley, Michael J. Angilletta Jr, Amanda C. Niehaus, and Robbie S. Wilson. How fast should an animal run when escaping? an optimality model based on the trade-off between speed and accuracy. *Integrative and Comparative Biology*, 55(6):1166–1175, 2015.

[134] C. D. Wilga and George V. Lauder. Locomotion in sturgeon: function of the pectoral fins. *Journal of Experimental Biology*, 202(18):2413–2432, 1999.

[135] Alexander Willmott and Charles Ellington. The mechanics of flight in the hawkmoth manduca sexta. *Journal of Experimental Biology*, 200(21):2705–2722, 1997.

[136] Alexander P. Willmott and Charles P. Ellington. The mechanics of flight in the hawkmoth *Manduca sexta*. i. kinematics of hovering and forward flight. *Journal of Experimental Biology*, 200(21):2705–2722, 1997.

[137] Xinyan Deng, L. Schenato, and S. S. Sastry. Flapping flight for biomimetic robotic insects: part ii-flight control design. *IEEE Transactions on Robotics*, 22(4):789–803, 2006.

[138] Olivia Zahn, Jorge Bustamante, Jr., Callin Switzer, Thomas L. Daniel, and J. Nathan Kutz. Pruning deep neural networks generates a sparse, bio-inspired nonlinear controller for insect flight. *PLoS Computational Biology*, tbd(tbd):tbd, In prep, 2021.

[139] Johannes M. Zanker. How does lateral abdomen deflection contribute to flight control of *Drosophila melanogaster*? *Journal of Comparative Physiology A*, 162:581–588, 1988.

[140] Johannes M. Zanker. On the mechanism of speed and altitude control in drosophila melanogaster. *Physiological Entomology*, 13(3):351–361, 1988.

[141] Yu Zeng, Kenrick Lam, Yuexiang Chen, Mengsha Gong, Zheyuan Xu, and Robert Dudley. Biomechanics of aerial righting in wingless nymphal stick insects. *Royal Society Interface*, 7(1), 2016.

[142] Anthony J. Zera and Lawrence G. Harshman. The physiology of life history trade-offs in animals. *Annual Review of Ecology and Systematics*, 32:95–126, 2001.

[143] H Zhu, H Liu, A Ataei, Y Munk, T Daniel, and IC Paschalidis. Learning from animals: How to navigate complex terrains. *PLoS computational biology*, 16(1):e1007452, 2020.

[144] Michael Zhu and Suyog Gupta. To prune, or not to prune: exploring the efficacy of pruning for model compression, 2017.